ALMA MATER STUDIORUM · UNIVERSITÀ DI BOLOGNA

Scuola di Scienze
Corso di Laurea Magistrale in Fisica della Materia

Optical properties of transition metal oxide perovskites by the Bethe-Salpeter equation

Relatore:
Prof. Cesare Franchini

Presentata da:
Lorenzo Varrassi

Anno Accademico 2018/2019

Abstract

In questa tesi abbiamo eseguito uno studio sistematico, tramite un approccio computazionale *ab-initio*, delle proprietà ottiche di un insieme di quattordici diverse perovskiti. Questi quattordici materiali sono stati scelti in modo da formare un insieme rappresentativo delle perovskiti di metalli di transizione, ed includono differenti configurazioni elettroniche, ordinamenti magnetici e caratteristiche strutturali, con bandgap che variano da 0.1 eV a 6.1 eV.

Lo studio è stato compiuto utilizzando un approccio basato sulla risoluzione dell'equazione di Bethe-Salpeter, dove le energie di quasi-particella e l'interazione schermata sono state ricavate da una precedente simulazione basata sull'approssimazione GW.

Il lavoro svolto è finalizzato alla valutazione del ruolo e del contributo dell'interazione elettrone-lacuna sugli spettri ottici dei materiali considerati. Per ogni perovskite abbiamo inoltre confrontato i risultati ottenuti con le misure sperimentali, laddove presenti, e con precedenti risultati numerici ottenuti nell'ambito dell' Approssimazione di Particelle Indipendenti (ottenuti a partire da spettri GW). Infine abbiamo determinato l'origine delle strutture all'interno dello spettro, attribuendole a transizioni tra specifiche bande.

Contents

Introduction

Transition Metal Oxide (TMO) perovskites are an extensively studied class of materials, with widely interesting chemical and physical properties and promising technological applications. A series of recent works have investigated, through *ab-initio* simulations, their structural and electronic properties with grat precision. However *their optical properties* (excluding the Metal Halide perovskite and $SrTiO_3$) have been less explored from a computational point of view, and to our knowledge their calculations have almost always been performed using the Independent Particle Approximation (IPA). This approach, however, has often proved to be inadequate to reproduce accurately the experimental spectra. Moreover, the IPA approximation is not able to describe the excitonic properties (that is, the electron-hole interaction).

The aim of the present work is therefore to address these issues by analysing the contribution of the electron-hole interaction to the optical properties of the studied materials. We also argue that the inclusion of the this interaction, beyond the Independent Particle Approximation, is crucial to obtain a better agreement with the experimental data for many TMO perovskites, such as the cubic non-magnetic ones $SrTiO_3$, $KTaO_3$, $SrZrO_3$, $SrHfO_3$.
We examined a representative dataset of fourteen $3d$, $4d$, and $5d$ TMO perovskites with different crystal structures and magnetic orderings. Specifically, we considered (1) non-magnetic d_0 cubic perovskites $STMO_3$ ($TM = Ti, Hf, Zr$) and $KTaO_3$; (2) non-magnetic and structural distorted $3d_0$ $LaScO_3$; (3) magnetic and structural distorted $LaTMO_3$ ($TM = Ti, V, Cr, Fe, Mn$), $SrTMO_3$ ($TM = Mn, Tc$), $NaOsO_3$ and Ca_2RuO_4. Their structural and electronic properties are briefly described in chapter 4.

The investigation of the optical properties outlined above is performed through *ab-initio* calculations made with the *Vienna Ab initio Simulation Package* ($VASP$).
The first step needed to obtain a optical spectra which includes the excitonic effect is a preliminary DFT calculation of the ground state properties of the compound; chapter 1 is devoted to an overview of the Density Functional Theory and of the Hartree Fock Approximation. However, such mean field methods are inadequate to describe the excited states properties, as we discuss in chapter 1.3: therefore they are unfit to describe the optical properties.
The state-of-the-art method to estimate the bandgap and the excited states properties is the so-called GW approximation, introduced in chapter 2. The GW method uses the one-body Green's functions and the many-body Perturbation Theory to determine the single-particle excitation spectrum of the quasiparticles. The implementation of the GW approximation relies on a perturbative treatment starting from DFT wavefunction and energies.
Nonetheless, in this method the interactions between quasiparticles are neglected, and

the quasiparticles are considered independent; In fact the so-called *Independent Particle Approximation* employs directly the results of a GW calculation to determine the optical spectra.
To overcome the IPA and include the interaction between electron-hole quasiparticles, we need to solve the Bethe-Salpeter Equation (BSE) for the two-particle Green's function (presented in chapter 3) starting from the wavefunction and the screened interaction calculated at the previous GW step. In chapter 5 we describe instead the parameters employed in the DFT and $G0W0$ runs.

The main disadvantages of the approach based on the Bethe-Salpeter equation are the large computational cost and memory requirements. The reason behind these disadvantages and the procedures chosen to cope with them are discussed in chapters 6.1, 7.1 and 6.3. Finally, in chapters 6.4, 7.2 and 7.3 the results are presented and commented.

Part I

Theoretical Background

As we briefly described in the introduction, three different steps are needed to obtain a single optical spectra which includes the excitonic effect: a preparatory *Density Functional Theory* calculation; a following GW calculation which improves the bandstructure obtained by the DFT method (the GW approximation in fact represents the current state of the art to simulate the bandstructure of a given compounds); a final step which the Bethe-Salpeter equation is solved to determine the dielectric function with the inclusion of the electron-hole interaction.
The first three chapter in this section are dedicated to these three methods: in each chapter we briefly summarize the theoretical background of the method itself (with a particular attention to the description of the excited states) and its implementation inside the software $VASP$.
In the fourth chapter an introduction to the transition metal oxide perovskites and their electronic and structural properties is given instead.

Chapter 1

Mean field methods

The fundamental idea behind the mean-field methods presented in this chapter is to replace an interacting many-body problem, notoriously hard to treat, with an *independent-particle* problem associated with an *effective* potential. This potential, which is the key of these methods, can be chosen as an approximation for the interaction effects in an average sense (as in the *Hartree-Fock* approximation) or defined in such a way to reproduce selected properties of the interacting system.
This chapter will provide a short summary of the Density Functional Theory, which will be applied in Part II, and of the Hartree Fock method, which will be not employed directly but will be used to understand the *GW* method.

1.1 Hartree-Fock Approximation

The Hartree-Fock approximation was developed by D.R. Hartree and W. Hartree[1], who combined their previous work[2] (the so called *Hartree* method) with the ideas on the antisymmetric wavefunction due to Fock[3].
The equations in the Hartree method neglect any non-classical interactions in the no-homogenneous electron gas, and can be obtained starting from a *single-particle wavefunction product antsaz* for the many-body wavefunction. We can refine the result by including the fermion nature of the electrons (that is the obedience of the Pauli exclusion principle) and still remain inside an independent particle approximation, and thus keeping the electrons uncorrelated. To do this we take as antsaz a *single* Slater determinant:

$$\Psi_{HF} = \frac{1}{\sqrt{N!}} \begin{vmatrix} \psi_{1,\sigma_1}(\vec{r}_1) & \psi_{1,\sigma_2}(\vec{r}_2) & \psi_{1,\sigma_3}(\vec{r}_3) & .. \\ \psi_{2,\sigma_1}(\vec{r}_1) & \psi_{2,\sigma_2}(\vec{r}_2) & \psi_{2,\sigma_3}(\vec{r}_3) & .. \\ \psi_{3,\sigma_1}(\vec{r}_1) & \psi_{3,\sigma_2}(\vec{r}_2) & \psi_{3,\sigma_3}(\vec{r}_3) & .. \\ .. & .. & .. & .. \end{vmatrix} \tag{1.1}$$

whew ψ are the single-particle orbitals, $\vec{r}_i$ and σ_i the position and spin of the *i-th* particle.
The total energy of a system of electrons in an external potential v_{ext} is

$$E = \langle \Psi_{HF} | \hat{H} | \Psi_{HF} \rangle = -\int d\vec{r} \sum_{i,\sigma_i} \psi^*_{i,\sigma_i}(\vec{r}) \frac{\nabla^2}{2} \psi_{i,\sigma_i}(\vec{r}) + \int d\vec{r}\, v_{ext}(\vec{r}) n(\vec{r}) + E_H + E_x \tag{1.2}$$

where

$$E_H = \frac{1}{2}\int d\vec{r}d\vec{r'}\frac{n(\vec{r})n(\vec{r'})}{|\vec{r}-\vec{r'}|} \tag{1.3}$$

is the Hartree contribution to the total energy and

$$E_x = -\frac{1}{2}\sum_{\sigma}\sum_{i,j}^{occ}\int d\vec{r}d\vec{r'}\ \psi^*_{j,\sigma}(\vec{r'})\psi_{i,\sigma}(\vec{r'})\frac{1}{|\vec{r}-\vec{r'}|}\psi_{j,\sigma}(\vec{r})\psi^*_{i,\sigma}(\vec{r}) \tag{1.4}$$

is the corresponding Fock (exchange) term (n is the density). This term is negative, reducing the total energy with respect to the Hartree approximation, and therefore stabilizing the electronic system.

To obtain the Hartree-Fock equations we perform a variational minimization of the total energy while requiring the orthonormality of the single-body orbital $\psi_{i,\sigma}$, i.e.:

$$\frac{\delta E}{\delta\psi^*_{i,\sigma}} = 0 \qquad \int d\vec{r}\ \psi^*_{i,\sigma}(\vec{r})\psi_{j,\sigma}(\vec{r}) = \delta_{i,j}$$

The Hartree-Fock equations are:

$$\left[-\frac{\nabla^2}{2} + v_{ext}(\vec{r}) + \sum_{j,\sigma_j}\int d\vec{r'}\psi^*_{j,\sigma_j}(\vec{r'})\psi_{j,\sigma_j}(\vec{r'})\frac{1}{|\vec{r}-\vec{r'}|}\right]\psi_{i,\sigma}(\vec{r}) \tag{1.5}$$

$$-\sum_{j}^{occ}\int d\vec{r'}\psi^*_{j,\sigma}(\vec{r'})\psi_{i,\sigma}(\vec{r'})\frac{1}{|\vec{r}-\vec{r'}|}\psi_{j,\sigma}(\vec{r}) = \epsilon_{i,\sigma}\psi_{i,\sigma}(\vec{r}) \tag{1.6}$$

Equation 1.5 represents a coupled set of integro-differential equations, and can be solved exactly only in some special cases.

The potential on the first line, arising from the Hartree energy (equation 1.3),

$$v_H = \sum_{j,\sigma_j}\int d\vec{r'}\psi^*_{j,\sigma_j}(\vec{r'})\psi_{j,\sigma_j}(\vec{r'})\frac{1}{|\vec{r}-\vec{r'}|} = \int d\vec{r'}\frac{n(\vec{r'})}{|\vec{r}-\vec{r'}|} \tag{1.7}$$

is also called the Hartree potential and it's local in space and time. It's the electrostatic potential arising from the electron charge density and includes the self-interactions (i.e. each electron acting on itself), and does not depend on the spin.

The second term is the non-local[1] and integral Fock operator, which can be rewritten as the so-called *Fock Self-energy* $\Sigma_{x\sigma}(\vec{r},\vec{r'})$:

$$\Sigma_{x\sigma}(\vec{r},\vec{r'}) \overset{\text{def}}{=} -\sum_{j}^{occ}\psi^*_{j,\sigma}(\vec{r'})\psi_{i,\sigma}(\vec{r'})\frac{1}{|\vec{r}-\vec{r'}|} \rightarrow \tag{1.8}$$

$$-\sum_{j}^{occ}\int d\vec{r'}\psi^*_{j,\sigma}(\vec{r'})\psi_{i,\sigma}(\vec{r'})\frac{1}{|\vec{r}-\vec{r'}|}\psi_{j,\sigma}(\vec{r}) = -\int d\vec{r}\ \Sigma_{x\sigma}(\vec{r},\vec{r'})\psi_{i,\sigma}(\vec{r}) \tag{1.9}$$

which is non-zero only for like spins. It originates from the antisymmetry of the wavefunction, and thus is linked to the Pauli's exclusion principle (in fact this term is absent

---

[1] in the sense that its evaluation requires an additional integration over the variable $\vec{r'}$.

in the Hartree method). Note that the case $j = i$ cancels exactly the spurious self-interaction term inside the Hartree potential.

In second quantization the mean field character of the Hartree-Fock approximation becomes more clear. The Hartree and Fock terms have the form:

$$\hat{U} = \frac{1}{2} \sum_{mm'nn'} \sum_{\sigma\sigma'} U_{mm'nn'} \hat{c}^+_{m\sigma} \hat{c}^+_{m'\sigma'} \hat{c}_{n'\sigma'} \hat{c}_{n\sigma} \tag{1.10}$$

where $m, m', n, n' = 1, .., N_{states}$ refer to the set of independent-particle wavefunctions and $\hat{c}^+_{m'\sigma'}, \hat{c}_{n'\sigma'}$ are the creation or annihilation operators.
The Hartree Fock method corresponds to the approximation of the two-particle terms in equation 1.10 with single-particle ones:

$$\hat{c}^+_{m\sigma} \hat{c}^+_{m'\sigma'} \hat{c}_{n'\sigma'} \hat{c}_{n\sigma} \quad \rightarrow \quad \langle \hat{c}_{m'\sigma'} \hat{c}_{n'\sigma'} \rangle \hat{c}^+_{m'\sigma} \hat{c}_{n\sigma} - \delta_{\sigma,\sigma'} \left\langle \hat{c}^+_{m\sigma} \hat{c}_{n'\sigma'} \right\rangle \hat{c}^+_{m'\sigma'} \hat{c}_{n\sigma} \tag{1.11}$$

where the first term yields the Hartree potential and the second term yields the exchange term.

Exchange hole

In this section we will concisely sketch an intuitive picture of the effect of the exchange term. Let's define the pair correlation functions:

$$h_{\sigma,\sigma'}(\vec{r}, \vec{r'}) \overset{\text{def}}{=} \left\langle \hat{\psi}^+_\sigma(\vec{r}) \hat{\psi}^+_{\sigma'}(\vec{r'}) \hat{\psi}^+_{\sigma'}(\vec{r'}) \hat{\psi}^+_\sigma(\vec{r}) \right\rangle - \left\langle \hat{n}_\sigma(\vec{r}) \right\rangle \left\langle \hat{n}_\sigma(\vec{r'}) \right\rangle \tag{1.12}$$

$$g_{\sigma,\sigma'}(\vec{r}, \vec{r'}) \overset{\text{def}}{=} \frac{\left\langle \hat{\psi}^+_\sigma(\vec{r}) \hat{\psi}^+_{\sigma'}(\vec{r'}) \hat{\psi}^+_{\sigma'}(\vec{r'}) \hat{\psi}^+_\sigma(\vec{r}) \right\rangle}{\left\langle \hat{n}_\sigma(\vec{r}) \right\rangle \left\langle \hat{n}_\sigma(\vec{r'}) \right\rangle} \tag{1.13}$$

We can obtain one definition from the other with:

$$h_{\sigma,\sigma'}(\vec{r}, \vec{r'}) = \left\langle \hat{n}_\sigma(\vec{r}) \right\rangle \left\langle \hat{n}_\sigma(\vec{r'}) \right\rangle \left[g_{\sigma,\sigma'}(\vec{r}, \vec{r'}) - 1 \right] \tag{1.14}$$

where $\hat{\psi}^+_\sigma(\vec{r}), \hat{\psi}_\sigma(\vec{r})$ are the creation and annihilation operators and $\hat{n}_\sigma(\vec{r}) = \psi^+_\sigma(\vec{r})\psi_\sigma(\vec{r})$ is the particle density operator. $h_{\sigma,\sigma'}$ evaluates the correlation in the system: in fact, if the probability of finding an electron (with spin σ) at $\vec{r}$ and a second one (with spin σ') at $\vec{r'}$ are uncorrelated then $h_{\sigma,\sigma'}(\vec{r}, \vec{r'}) = 0$.

The Hartree-Fock equations don't contain any term which accounts for the electron-electron correlation stemming from the electron-electron interaction. We recall in fact that the Hartree-Fock wavefunction is a *single Slater determinant.*
However, the pair correlation function is different from zero for electron with like spin even when no electron-electron interaction is present, such as in the Hartree-Fock approximation. For example, in the three-dimensional homogeneous Fermi-gas ground state we can prove that[4, 5]:

$$h_{\sigma,\sigma}(\vec{r}, \vec{r'}) = - \left[\left(\frac{3n}{2} \right) \frac{\sin(x) - x\cos(x)}{x^3} \right]^2 \tag{1.15}$$

with $x = k_F|\vec{r} - \vec{r'}|$, and n is the density. The probability of finding an electron with σ spin in the vicinity of another σ electron on the scale of the reciprocal Fermi wave number $1/k_F$ si partially suppressed, due to the Pauli principle. This effect, called *exchange hole*, is totally independent of electron-electron interaction and descends only from the exchange effects. In fact, for electrons with different spins we instead find that electrons are totally uncorrelated:

$$h_{\sigma,-\sigma}(\vec{r},\vec{r'}) = 0 \tag{1.16}$$

Historically, the correlation energy has been defined as the Hartree-Fock energy defined in equation 1.2 (completely uncorrelated) minus the exact ground-state energy.

1.2 Density Functional Theory

1.2.1 Kohn-Hohenberg theorems

The Density Functional Theory (hereafter *DFT*) is a very popular and successful theory, frequently adopted to study the ground state electronic and structural properties of a vast class of materials. The foundation of this approach is given by the two *Kohn-Hohenberg* theorems[6]. Their statement will be presented and commented without giving a proof, which can be found in many books[4, 7, 8, 9, 10]. The original formalism is derived assuming a non degenerate ground state, however later works by Kohn[11], as well as the alternative formulation provided by Levy[9], overcome this limitation.

Theorem 1 *For any system of interacting particles in an given external potential* $v_{ext}(\vec{r})$*, the potential itself is determined uniquely (within an additive constant) by the ground state particle density* $n_0(\vec{r})$*.*

Mathematically, the first theorem proves that the map $v_{ext} \rightarrow n_0$ *is injective* [9, p. 10][10, p. 232][12, p. 435]. If we restrict to the n_0 determined by a given v_{ext} (we will elaborate on this later) this map can be inverted: the density therefore becomes the basic variable in this approach and v_{ext} becomes an unique functional of the electron density n_0.

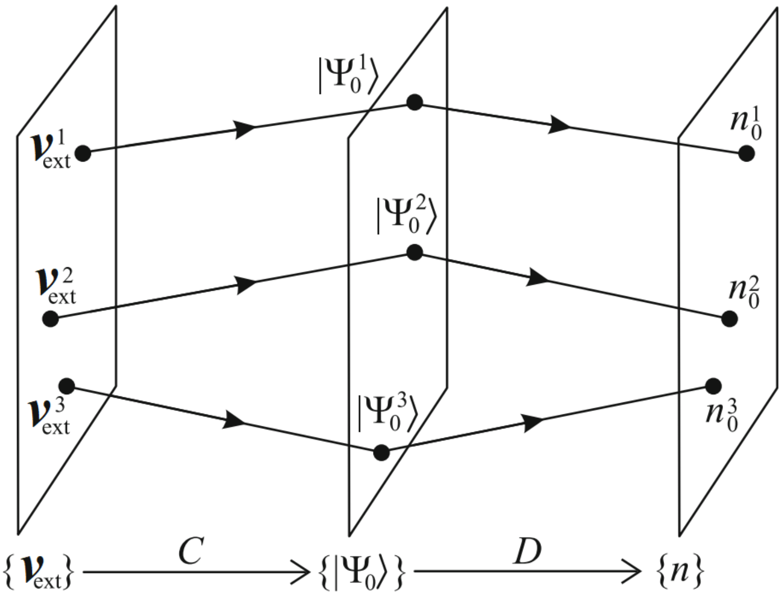

Figure 1.1: The First Kohn-Hohenberg theorem proves that the map $(C \circ D)$ is injective, and thus invertible (restricting n_0 to the *v-representable* ones). Taken from [13].

The immediate consequence of the first theorem is that the many-body hamiltonian is fully determined by the ground state density $n_0(\vec{r})$. This in turn implies that the many-body wavefunctions of *all* states (ground and excited)[4] are determined by the same ground state density $n_0(\vec{r})$, and *therefore all properties of the system are completely determined by it*:

$$\psi(\vec{r}_1, \vec{r}_2, .., \vec{r}_N) = \psi[n_0(\vec{r})] \quad \Longrightarrow \quad \left\langle \hat{O} \right\rangle = \langle \psi[n_0(\vec{r})] | \hat{O} | \psi[n_0(\vec{r})] \rangle$$

Because every expectation value is fully determined by the ground state density, the energy (which obviously is the expectation value of the hamiltonian) can be written as a functional of $n_0(\vec{r})$. Hence we can easily find that:

$$E[n_0(\vec{r})] = \left\langle \hat{T}[n_0(\vec{r})] \right\rangle + \left\langle \hat{V}_{ne}[n_0(\vec{r})] \right\rangle + \left\langle \hat{V}_{ee}[n_0(\vec{r})] \right\rangle \tag{1.17}$$

where $\hat{T}$ is the kinetic energy, $\hat{V}_{ne}$ the term arising from the nucleus-electron interaction and $\hat{V}_{ee}$ the term associated to the electron-electron interaction. We can reorganize this equation by defining the so called *Hohenberg-Kohn* functional F_{HK}:

$$F_{HK}[n_0(\vec{r})] \overset{\text{def}}{=} \left\langle \hat{T}[n_0(\vec{r})] \right\rangle + \left\langle \hat{V}_{ee}[n_0(\vec{r})] \right\rangle \rightarrow \quad E[n_0(\vec{r})] = F_{HK}[n_0(\vec{r})] + \int d\vec{r} v_{ext}(\vec{r}) n_0(\vec{r}) \tag{1.18}$$

This form has the merit to make the dependence on the external potential v_{ext} explicitly. In fact the functional F_{HK} is defined independently of the external potential v_{ext}; that is, the formal definition of this functional is the same for all electron systems.

The second theorem paves a way to calculate E, defining the variational behaviour of the energy functional:

Theorem 2 *Let $v_{ext}(\vec{r})$ be the external potential of a specific system with exact ground state density $n_0(\vec{r})$. The exact ground state energy of the system is the global minimum value of the functional $E[n(\vec{r})]$, and the density that minimizes the functional is $n_0(\vec{r})$.*

So it follows that, supposing that the expression for F_{HK} was known, we can find the exact ground state density and energy by minimizing the total energy of the system with respect to variation of the density $n(\vec{r})$. Note that the theorem determines only the ground state properties (density and energy), and it does not provide any hint regarding the excited states.

However, a technical but important problem arises: the framework requires that n_0 *is* the ground state density of an Hamiltonian with a suitably chosen $v_{ext}(\vec{r})$; such densities are called *v-representable.*

However we can't exclude *a priori* the existence of n_0 that *cannot* be derived from any Hamiltonians with some external potential. Moreover, different works have found specific examples of reasonably well-behaved function that cannot be determined from a specific hamiltonian[14, 15] (an overview can be found in [9]). This problem has still no solution in the case of continuous systems.

Another issue concerns the *N-representability*, corresponding to the question: *is it possible to derive a corresponding N-body antisymmetric wavefunction given an arbitrary $n(\vec{r})$?*

This problem was solved for by Gilbert[16], who found that the answer is positive under the conditions $n(\vec{r}) \geq 0$ and $\int d\vec{r} |n(\vec{r})^{1/2}|^2$ finite.

1.2.2 Kohn-Sham equations

While it's possible, in principle, to implement a direct minimization of an explicit energy functional of the density, this is not the most efficient approach. *DFT*'s popularity is due to the reformulation by Kohn and Sham: they introduced an *auxiliary independent-particle theory*, which is solvable and is specifically chosen to reproduce

exactly some properties of the full many-body system (the density n_0), but not all. In other words, the Kohn-Sham formulation of *DFT* maps an N interacting electrons system onto a system of N non-interacting *fictitious* particles - the Kohn-Sham particles - which move in an effective potential, while reproducing only certain properties (such as the density) of the original system.
Formally, the Kohn-Sham approach relies on two assumptions[4]:

1. The exact many body ground state density can be represented by the ground state density of an *auxiliary* system of non-interacting particles: $n(\vec{r}) = \sum_\sigma \sum_{i=1}^N |\psi_{i,\sigma}^{KS}(\vec{r})|^2$ where $\psi_i^{KS}(\vec{r})$ are the single particle wavefunctions and are called *Kohn-Sham* orbitals.
   This is referred as *non-interacting V-representability*, and we will assume its validity.
2. The auxiliary hamiltonian is defined with the usual kinetic operator and an *effective* potential V_{eff}. We assume, for simplicity, that V_{eff} is spin independent, although it's not strictly necessary.

The Kohn-Sham approach now proceeds to rewrite the ground state energy functional 1.17 through $\psi_{i\sigma}^{KS}$:

$$\begin{aligned} E[n] =& T_{ip}[n] + \int d\vec{r} v_{ext}(\vec{r})n(\vec{r}) + E_H[n] + E_{xc}[n] \\ T_{ip}[n] =& -\frac{1}{2}\sum_\sigma \sum_{i=1}^N \langle \psi_{i,\sigma}^{KS}|\nabla^2|\psi_{i,\sigma}^{KS}\rangle = \frac{1}{2}\sum_\sigma \sum_{i=1}^N |\nabla \psi_{i,\sigma}^{KS}|^2 \\ E_H[n] =& \frac{1}{2}\int d\vec{r} d\vec{r'} \frac{n(\vec{r})n(\vec{r'})}{|\vec{r}-\vec{r'}|} \end{aligned} \tag{1.19}$$

T_{ip} is the independent-particle kinetic energy and E_H is the Hartree Energy defined in equation 1.3. *But what is E_{xc}?*
The exchange-correlation functional contains the difference between the exact kinetic energy $\left\langle \hat{T} \right\rangle$ and T_{ip}, plus the difference between the exact interaction energy $\left\langle \hat{V}_{ee} \right\rangle$ and the Hartree Energy. In other words, E_{xc} contains all many-body effects of exchange and correlation:

$$E_{xc}[n] \stackrel{\text{def}}{=} F_{HK}[n] - (T_{ip}[n] + E_H[n]) = \left\langle \hat{T} \right\rangle - T_{ip}[n] + \left\langle \hat{V}_{ee} \right\rangle - E_H[n] \tag{1.20}$$

E_{xc} is a functional of the density since all the variables on the right-hand side are functional of it; moreover, it's a universal functional in the same sense of F_{HK}.
Finally, we can write the auxiliary hamiltonian:

$$\left[-\frac{1}{2}\nabla^2 + v_{eff}(\vec{r}) \right] \psi_i^{KS}(\vec{r}) = \epsilon_i^{KS} \psi_i^{KS}(\vec{r}) \tag{1.21}$$

The condition of minimum energy for fixed particle number defines v_{eff}:

$$v_{eff}(\vec{r}) \stackrel{\text{def}}{=} v_{ext}(\vec{r}) + \frac{\delta E_H[n]}{\delta n(\vec{r})} + \frac{\delta E_{xc}[n]}{\delta n(\vec{r})} = v_{ext}(\vec{r}) + v_H(\vec{r}) + v_{xc}(\vec{r}) \tag{1.22}$$

These equations are called the *Kohn-Sham* equations and must be solved self-consistently, since the potential is a functional of the density.

The potential v_{xc} has a critical role in this formulation, however an explicit and exact form for it is not known: we have to resort to approximations. To quote Kohn's Nobel Prize Lecture (Kohn, 1999):

> *"The Kohn–Sham theory may be regarded as the formal exactification of Hartree theory. With the exact E_{xc} and V_{xc} all many-body effects are in principle included. Clearly this directs attention to the functional $E_{xc}[n]$. The practical usefulness of ground-state DFT depends entirely on whether approximations for the functional $E_{xc}[n]$ could be found, which are at the same time sufficiently simple and sufficiently accurate."*

1.2.3 Exchange and Correlation functionals

One of the reason of the success of the DFT approach is that even comparatively simple functionals can often reach overall good results for many properties.
The simplest approximation is the **Local Density Approximation (LDA)**, where E_{xc} is assumed only *locally* dependent on the charge density. It's defined from the homogeneous electron gas exchange-correlation energy density ϵ_{xc}^{HEG}:

$$E_{xc}^{LDA}[n] \stackrel{\text{def}}{=} \int d\vec{r} n(\vec{r}) \epsilon_{xc}^{HEG}(n) \tag{1.23}$$

Where $\epsilon_{xc}^{HEG}(n)$ is equal to the sum of the exchange and correlation contributions $\epsilon_{xc}^{HEG}(n) = \epsilon_{c}^{HEG}(n) + \epsilon_{c}^{HEG}(n)$. $\epsilon_{x}^{HEG}(n)$ is known analytically:

$$\epsilon_{x}^{HEG}(n) = -\frac{3}{4}\left(\frac{3}{\pi}\right)^{1/3} n^{4/3} \tag{1.24}$$

The determination of $\epsilon_{c}^{HEG}(n)$ is more complicated. Early expressions were based on perturbation theory[17] (specifically the Random Phase Approximation), but modern implementations rely on parameterizations of Quantum Monte Carlo calculations[18].

A refinement of the *LDA* is the **Generalized Gradient Approximation (GGA)**, where E_{xc} is not only function of $n(\vec{r})$ but also of $\nabla n(\vec{r})$ (functionals of this kind are called *semilocal*):

$$E_{xc}^{GGA}[n] \stackrel{\text{def}}{=} \int d\vec{r} f\left(n(\vec{r}), \nabla n(\vec{r})\right)) \tag{1.25}$$

The most popular *GGA*s are *PBE* (proposed in 1996 by *Perdew. Burke and Ernzenhof*[19]) and *BLYP* (the combination of Becke's 1988 exchange functional[20] with the 1988 correlation functional by *Lee, Yang and Parr*[21]).

There have been efforts in the past to move beyond the *GGA*. One class of very successful functionals are the **hybrids** ones, which mix a fraction of the (non local) Hartree-Fock exchange into the DFT exchange-correlation functional, but also other mixtures are possible. The original definition of a hybrid functional involves a certain empiricism in the choice of the component functionals and of the weights to assign to each one[2]. In this work we will briefly employ the *HSE06*[24] hybrid functional.

---

[2] although several self-consistent and parameter free hybrid functionals have been defined in the recent years [22, 23].

Exact constraint and the exchange-correlation hole
While the construction of the *LDA* scheme calls for application only to systems with a slowly varying density, many somewhat satisfying results have been reported for inhomogeneous systems quite different from homogeneous electron gas. This success calls for an explanation.

This can be related to the fact that *LDA* satisfies several constraints and reproduce various properties of the exact exchange-correlation functional. The first one is linked to the exchange-correlation hole, already introduced in section 1.1. We start by defining a variant of the correlation function (equation 1.13), the *average pair correlation function*:

$$\bar{g}(\vec{r},\vec{r'}) \overset{\text{def}}{=} \int_0^1 d\lambda g_\lambda(\vec{r},\vec{r'}) \tag{1.26}$$

where $g_\lambda(\vec{r},\vec{r'})$ is defined within a system with a rescaled electron interaction $\frac{\lambda}{|\vec{r}-\vec{r'}|}$; $\lambda = 0$ is associated with a system with no interaction, where $\lambda = 1$ describes the usual Coulomb interaction.
Gunnarsson *et.al.*[25] define the *exchange-correlation hole density*, representing the charge density *depletion* around the electron due to exchange and correlation as:

$$n_{xc}(\vec{r},\vec{r'}) \overset{\text{def}}{=} n(\vec{r})\bar{g}(\vec{r},\vec{r'}) \tag{1.27}$$

This hole density satisfies the sum rule:

$$\int \vec{r} d\vec{r'} n_{xc}(\vec{r},\vec{r'}) = -1 \tag{1.28}$$

which means the charge depletion sums up to exactly one electron charge.
We can restate the exact exchange-correlation energy through n_{xc}:

$$E_{xc} = \frac{e^2}{2} \int d\vec{r} n(\vec{r}) \int d\vec{r'} n_{xc}(\vec{r},\vec{r'}) \frac{1}{|\vec{r}-\vec{r'}|} \tag{1.29}$$

Interestingly, E_{xc} depends *only* on the monopole part of the multipole expansion of n_{xc}(for a given $\vec{r}$), that is only on the spherical average of n_{xc}:

$$n_{xc}(\vec{r},\vec{r'}) = \sum_{l,m} n_{xc}^{lm}(\vec{r},\vec{r'}) Y_{lm}(\Omega) \implies \quad E_{xc} = \frac{1}{2} \int d\vec{r} n(\vec{r}) \int dR \frac{1}{R} n_{xc}^{00}(\vec{r},R) \tag{1.30}$$

where $R = |\vec{r} - \vec{r'}|$.

Does the LDA approximation describe correctly the exchange-correlation hole density and its properties? An important success of the *LDA* approximation is the correct reproduction of the sum rule defined in equation 1.28[9, p. 186]. Moreover it replicates rather well the hole spherical average, even if the exact curve is poorly approximated. For example, we show the results for the *Ne* atom by Gunnarsson *et.al.*[25].
Lastly, it's important to note that also the *GGA* approximation developed by Perdew *et.al* fulfills the sum rule for the exchange-correlation hole.

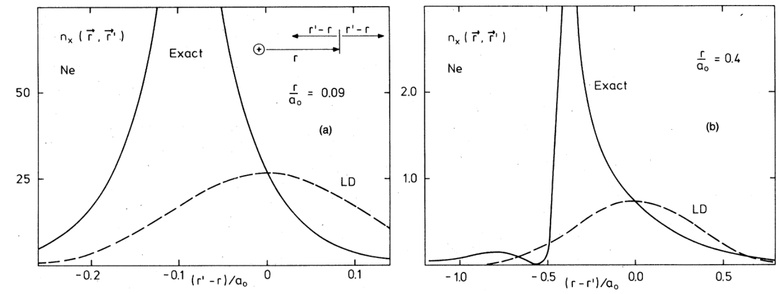

Figure 1.2: Exchange hole n_{xc} of Ne atom for *(a)*$r = 0.09a_0$ and *(b)*$r = 0.4a_0$. The full curves are the exact results while the dashed curves are obtained with *LDA*. From [25].

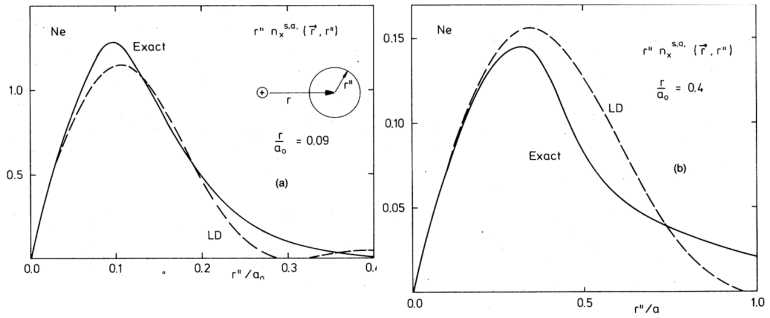

Figure 1.3: Spherically average exchange hole n_{xc} of Ne atom $(r'n_{xc}(r,r')/sqrt4\pi)$for *(a)*$r = 0.09a_0$ and *(b)*$r = 0.4a_0$. The full curves are the exact results while the dashed curves are obtained with *LDA*. From [25].

1.3 Excited states

The correct estimation of the excited states and in particular of the bandgaps is critical for the study of the optical properties. Therefore, in this chapter we briefly summarize how the two methods discussed in this chapter perform these tasks.

1.3.1 Excited states in Hartree Fock

In the Hartree Fock theory, the Koopmans' theorem gives a very clear physical meaning to the eigenvalues:

$$\epsilon_i^{HF} = E(f_1, .., f_i, .., f_n) - E(f_1, .., f_i - 1, .., f_n) \tag{1.31}$$

where ϵ_i^{HF} is the i-th Hartree Fock eigenvalue, f_i is the occupancy of the i-th level and $E(f_1, .., f_i, .., f_n)$ represents the total energy of a system of $f_1 + .. + f_i + .. + f_n$ electrons. Therefore the eigenvalues of the single electron equation have a unambiguous physical meaning: they represent the energy required to remove an electron from the i-th orbital, *i.e.* the *ionization energy.*
However, the Hartree Fock description usually offers a very poor comparison with the experimental data: for example, the method consistently overestimates the direct bandgap for different materials (see Table 1.1). This can be traced back to two main reasons:

- The glaring deficiency of Hartree Fock theory is the absence of any description of the correlation effects.

- Moreover, Koopmans' theorems describe the addition or removal of electrons to the system, but HF description neglects the relaxation effects: indeed the other *HF* eigenvalues ($\epsilon^{HF}_{j\neq i}$) remain unchanged and at the same value. In other words, the other orbitals are not relaxed to a new equilibrium configuration after the addition or removal, but are "*frozen*"[26, p. 330].

	DFT (eV)	***HF*** (eV)	**Experimental** (eV)
Ge	0.5[27]	4.3[28]	1.0[28]
C	5.6[29]	15.0[29]	7.3[29]
Si	2.6[29]	9.4[29]	3.4[29]
Ne	21.2[29]	25.1[29]	21.4[29]
Ar	8.3[29]	18.5[29]	14.3[29]
Kr	6.8[29]	16.4[29]	11.6[29]

Table 1.1: Comparison of minimum direct bandgap (in eV) calculated with the *HF* and *DFT* methods.

1.3.2 Excited states in DFT

We briefly hinted before that the second Kohn-Hohenberg theorem applies only to ground state. *It is possible to extend the Kohn-Hohenberg framework to the excited states and properties*?
First of all, the map $n_0 \to v_{ext}$ loses its bijectivity: Epstein and Rosenthal proved[30] (via finite dimension counterexample) that the external potential is in general not uniquely associated to a given excited state density. Another important work on the topic was written by Perdew and Levy[31], which proved various results:

- Every extremum density $n_i(\vec{r})$ of the *ground state* energy functional $E[n(\vec{r})]$ yields the energy E_i of an exact stationary state of the system. The absolute minimum corresponds to the ground state density and energy, while the other extrema correspond to excited state densities.

- the coverage is incomplete: not every excited state density $n_i(\vec{r})$ is an extrema of the ground state energy functional. In other words, the extrema of $E[n(\vec{r})]$ represent only a subset of all excited state density.

- If $n_i^{exact}(\vec{r})$ is an arbitrary exact excited state density with energy E_i^{exact} then the ground state energy functional provides a lower bound for the exact energy ($E[n_i^{exact}] \leq E_i^{exact}$) and this equality holds if and only if $n_i^{exact}(\vec{r})$ is an extremum of ground state energy functional $E[n(\vec{r})]$.

Janak's theorem
However the one-particle *KS* eigenvalues have been commonly used as excitation energies without, as we saw, formal justification. While in Hartree Fock theory the Koopmans' theorem gives a sound physical meaning to the eigenvalues of the single electron equation, this association between eigenvalues and ionization energies is not

longer in general valid in the *DFT* framework.
However a result involving eigenvalues exists, the so called Janak's theorem:

$$\frac{\partial E}{\partial f_i} = \epsilon_i^{KS} \tag{1.32}$$

where f_i represents a fractional particle number. From this result we can give a physical meaning *only* to the highest occupied eigenvalue ϵ_N^{KS}:

$$E(N) - E(N-1) = \int_0^1 df_N \frac{\partial E}{\partial f_N} = \int_{N-1}^{N} df_N \epsilon_N^{KS} \tag{1.33}$$

where E_N and E_{N-1} are the ground energies for a system with N and $N-1$ electrons and ϵ_N^{KS} is the highest occupied eigenvalue of a system of N electrons.
Because ϵ_N^{KS} does not depends[3] on f_N we find that $E_N - E_{N-1} = -\epsilon_N^{KS}$, which means that from this theorem we can easily find the *ionization energy.* We stress that this is true within an *exact* DFT, so without taking into consideration the various approximations used for E_{xc}.
Can we reproduce the same procedure for all eigenvalues of a given KS hamiltonian? For example, for E_N and E_{N+1} holds $E_{N+1} - E_N = -\epsilon_{N+1}^{KS}$: however this eigenvalue *does not belong* to the N-electron *KS* hamiltonian, but to the $N+1$ one: they are not eigenvalue of the same hamiltonian.

The bandgap problem

One of most important properties that involves excited states is the bandgap, which is unfortunately significantly underestimated by the *DFT*; In general the *LDA* predicts bandgaps at least $30\% - 50\%$ smaller than the experimental ones. This issue is called in literature the *bandgap problem.*
Following the reasoning presented previously, the DFT could in principle evaluate the exact value for the bandgap as a difference of total ground state energies:

$$E_{gap}^{exact} = (E_{N+1} - E_N) - (E_N - E_{N-1}) = \epsilon_{N+1}^{KS}(N+1) - \epsilon_N^{KS}(N) \tag{1.34}$$

where we have slightly changed the notation and $\epsilon_M^{KS}(N)$ means the *M-th KS* eigenvalue of a system with N electrons.

The Kohn-Sham gap is $\epsilon_{gap}^{KS} = \epsilon_{N+1}^{KS}(N) - \epsilon_N^{KS}(N+1)$, implying that:

$$E_{gap}^{exact} = \epsilon_{gap}^{KS} + \epsilon_{N+1}^{KS}(N+1) - \epsilon_{N+1}^{KS}(N) \tag{1.35}$$

Thus, even an *exact DFT* underestimates E_{gap}^{exact} by the correction $\Delta = \epsilon_{N+1}^{KS}(N+1) - \epsilon_{N+1}^{KS}(N)$. Works of the early 1980s[32, 33] gave an expression to Δ in term of the exact v_{xc} potential:

$$\Delta = \lim_{\Delta n \to 0} v_{xc}[n + \Delta n] - v_{xc}[n - \Delta n] \tag{1.36}$$

When an electron is added or removed from a solid, the density change is infinitesimal and periodic, thus $\Delta n \to 0$. We would therefore expect that also v_{xc} changes infinitesimally upon electron addition or removal, but this is not correct. In fact the exact v_{xc}

---

[3] this is true because the exact ground state energy functional is a series of straight lines with discontinuities at integer occupancies[32].

varies discontinuously, and $\Delta \neq 0$: it can reach values up to 1 eV [34]. This shows that even exact DFT calculations *cannot* yield the correct bandgap, because it doesn't account for Δ.
Furthermore, standards exchange-correlation functionals such as the *LDA* possess no derivate discontinuity, and in this sense fails to reproduce an important feature of the exact exchange-correlation functional. It has also been proved that an exact exchange-correlation functional, possessing the derivative discontinuity, cannot be an explicit and differentiable functional of the electron density[35].

Additional shortcoming of v_{xc}: local nature and self-interaction
Another important drawback that we only hint at is the *local* nature of the exchange correlation potential. We recall that the v_{xc} potential, at least in the *LDA* approximation, is static and a local functional of the density. Many authors[36, 37, 38] have pointed out that the exact exchange correlation functional, however, is an highly non local functional of the density: a change in the density at a given point $\vec{r}$ may induce strong variation at a distant point $\vec{r'}$.
In fact, as discussed previously, many modern approach such as the hybrid one or the *meta-GGA* try to implement a functional which have a non local dependence on the density, either by including a fraction of Hartree Fock exchange or a dependence on the non-interacting kinetic energy.

Finally, other important properties of the exact functional are two conditions which embody the absence of artificial self-interaction[39]: in the one-electron limit the correlation and exchange energy must satisfy $E_c[n^{(1)}] = 0 \quad E_x[n^{(1)}] = -E_H[n^{(1)}]$.
These conditions are satisfied by the Hartree Fock approximation, but not by *LDA* and *GGA*.
The self-interaction error is particularly critical for localized states, such as the d states in transition-metal oxides: *DFT* often leads to an artificial stabilization of delocalized states[40].

1.4 DFT implementation in VASP

One of the fundamental milestones in condensed matter physics is the Bloch theorem, which argues that the electronic wavefunction in a system exhibiting translational invariance can be written as

$$\psi_{n\vec{k}}(\vec{r}) = u_{n\vec{k}} e^{i\vec{k}\cdot\vec{r}} \tag{1.37}$$

where $u_{n\vec{k}}$ represents a periodic function with the same periodicity of the crystal (i.e. of the crystal potential), and can be expanded on a plane wave basis set associated with the reciprocal lattice vectors (Ω is the primitive cell volume):

$$u_{n\vec{k}} = \frac{1}{\sqrt{\Omega}} \sum_{\vec{G}} C_{\vec{G}n\vec{k}} e^{i\vec{G}\cdot\vec{r}} \quad \Longrightarrow \quad \psi_{n\vec{k}}(\vec{r}) = \frac{1}{\sqrt{\Omega}} \sum_{\vec{G}} C_{\vec{G}n\vec{k}} e^{i(\vec{G}+\vec{k})\cdot\vec{r}} \tag{1.38}$$

why a plane wave basis set? There are different reasons, that can be traced back to *historical, practical* and *computational* ones. The historical one is that the pseudopotential theory, which was a precursor of the method implemented in *VASP* (The Projected Augmented Wave, or *PAW*), was originally developed to cope with elements that can

be easily interpreted in a free electron picture, like metallic s and p compounds.
The practical reason argues that the total energy expressions (briefly discussed in chapter 1.2.2) and the hamiltonian $\hat{H}$ have an easy implementation within this basis set. Finally, $\hat{H}\left|\psi\right\rangle$ can be evaluated in a efficient manner using the Fast Fourier Transform.

While the exact basis set contains an infinite number of plane waves, for implementation reason their number of the plane waves must be finite. The cutoff (defined by the parameter $ENCUT$) is imposed on the energy, i.e:

$$\psi_{n\vec{k}}(\vec{r}) = \frac{1}{\sqrt{\Omega}} \sum_{\vec{G}}^{\frac{\hbar^2}{2m}|\vec{k}^2+\vec{G}^2|<ENCUT} C_{\vec{G}n\vec{k}}\, e^{i(\vec{G}+\vec{k})\cdot\vec{r}} \tag{1.39}$$

Note that this implies that the number of plane waves can differ for each kpoints.

Ideally, the computation of quantities like energies and densities would require integrations over the entire *Brillouin Zone* (BZ) (defined as the Wigner–Seitz cell in reciprocal space). From a numerical standpoint, an integral evaluation can be carried out only in an approximate way through a weighed sum on a finite set of point (called *kpoint grid* or *kpoint mesh*), carefully chosen:

$$\frac{1}{\Omega_{BZ}} \int_{\Omega_{BZ}} d\vec{k} f(\vec{k}) \simeq \sum_{\vec{k}} \omega_{\vec{k}} f(\vec{k}) \tag{1.40}$$

For the *DFT* calculations *VASP* takes advantage of the crystal points symmetries of the system to run the calculation only to the kpoints belonging to the *Irreducible Brillouin Zone* (which is defined as the smallest fraction of the BZ that reproduce the complete BZ through the symmetries).

1.4.1 The Projector Augmented-Wave method (PAW)

Within the *DFT* approach, several methods have been developed to solve the Kohn-Sham equations. The one implemented in *VASP*, the *Projector Augmented Wave Method* (*PAW*)[41], was first introduced as a combination of the augmented wave methods[42] and the pseudopotential methods[43], and then improved by Kresse[44, 45]. The electrons are divided in two sets: the core electrons, which are close to the nucleus, and the valence electrons, which are further away from the nucleus itself. The valence electrons play a major role in processes such as bonding or electron transfer, and because of this their wavefunctions can significantly change; the core wavefunctions play instead a minor role in such processes, and so their wavefunctions undergo only minor changes.

The first idea is, therefore, to define a core region (called *Augmentation Region* with radius r_c) and substitute the *all-electron Kohn-Sham* wavefunction $\left|\psi^e\right\rangle$ with a *"pseudized"* one $\left|\tilde{\psi}^p\right\rangle$: this wavefunction reproduces the behaviour of the all-electron one outside the core region but is smoothly simplified within this region.
The method starts with a partial wave expansion for the pseudized wavefunction and

the full one-electron Kohn-Sham wavefunction $|\psi^e\rangle$ *within the augmentation region*:

$$|\psi^e\rangle = \begin{cases} \sum_i c_i \, |\phi_i^e\rangle & r < r_c \\ |\psi^e\rangle & r \geq r_c \end{cases} \qquad \left|\tilde{\psi}^p\right\rangle = \begin{cases} \sum_i c_i \left|\tilde{\phi}_i^p\right\rangle & r < r_c \\ |\psi^e\rangle & r \geq r_c \end{cases} \tag{1.41}$$

the partial waves $|\phi^e\rangle$ are the solutions of the radial Schröedinger equation:

$$\left[-\frac{\hbar^2}{2m}\nabla^2 + v_{eff}\right] |\phi_i^e\rangle = \epsilon_i \, |\phi_i^e\rangle \tag{1.42}$$

and the special projector functions c_i are defined through the relation:

$$c_i = \left\langle \tilde{p}_i \middle| \tilde{\psi}^p \right\rangle \tag{1.43}$$

which must fulfill the condition $\left\langle \tilde{p}_i \middle| \tilde{\phi}_j \right\rangle = \delta_{ij}$. The connection between the pseudized wavefunction and the full Kohn-Sham wavefunction is given by the identity:

$$|\psi^e\rangle = \left|\tilde{\psi}^p\right\rangle + \left(|\psi^e\rangle - \left|\tilde{\psi}^p\right\rangle\right) = \left|\tilde{\psi}^p\right\rangle + \sum_i c_i \, |\phi_i^e\rangle - \sum_i c_i \left|\tilde{\phi}_i^p\right\rangle \tag{1.44}$$

The idea behind this equation is to reconstruct $|\psi^e\rangle$ by starting from $\left|\tilde{\psi}^p\right\rangle$, subtracting $\sum_i c_i \left|\tilde{\phi}_i^p\right\rangle$ and finally replacing it with $\sum_i c_i \, |\phi_i^e\rangle$.
The pseudo partial waves are determined by:

$$\left[-\frac{\hbar^2}{2m}\nabla^2 + \tilde{v}_{eff} + \sum_{i,j} \left|\tilde{\phi}_i^p\right\rangle D_{ij} \left\langle \tilde{\phi}_i^p\right|\right] \left|\tilde{\phi}_i^p\right\rangle = \epsilon_i \left[1 + \sum_{i,j} \left|\tilde{\phi}_i^p\right\rangle D_{ij} \left\langle \tilde{\phi}_i^p\right|\right] \left|\tilde{\phi}_i^p\right\rangle \tag{1.45}$$

with $Q_{ij} = \langle \phi_i^e | \phi_j^e \rangle - \left\langle \tilde{\phi}_i^p \middle| \tilde{\phi}_j^p \right\rangle$, $D_{ij} = \langle \phi_j^e | \frac{\hbar^2}{2m}\nabla^2 + v_{eff} | \phi_j^e \rangle - \left\langle \tilde{\phi}_j^p \middle| \frac{\hbar^2}{2m}\nabla^2 + \tilde{v}_{eff} \middle| \tilde{\phi}_j^p \right\rangle$.
The *PAW* method implemented in *VASP* exploits also the *Frozen Core* approximation.
This method employs a smaller core radius r_c than the one used by a simple pseudopotential one: this makes it more computationally expensive, but in turn it offers higher quality results and a better reproduction of the nodes inside the core region.

1.4.2 The Self-Consistent cycle

The Hartree potential, being a functional of the density, requires the density itself to be evaluated. Thus the KS equations, which can be employed to determine $n(\vec{r})$, require too the density itself. Thus, to solve these equations we need a self-consistent loop:

1. Start from an initial guess for the density $n(\vec{r})$.
2. Calculate the KS effective potential $v_{eff}(\vec{r})$ defined in equation 1.22.
3. Solve the KS equations 1.21, obtaining $\psi^K S(\vec{r})$.
4. Evaluate the electronic density $n(\vec{r}) = 2\sum_i |\psi_i^{KS}(\vec{r})|^2$ and the total energy 1.19.
5. Check if it satisfies the convergence condition; otherwise repeat the loop. The convergence criterion can be either imposed on the density (if the input and output densities of a given cycle are equal within a certain accuracy), on the total energy or on different physical quantities.

Chapter 2

The GW Approximation

2.1 Theory: the Green function approach

Let's consider a non relativistic system of N electrons with exact ground state $\left|\psi_0^N\right\rangle$. The one particle Green function in coordinate space is defined as:

$$G(\vec{r},t,\vec{r'},t') \overset{\text{def}}{=} -i\left\langle\psi_0^N\right|\hat{T}\left[\hat{\psi}(\vec{r},t)\hat{\psi}^\dagger(\vec{r'},t')\right]\left|\psi_0^N\right\rangle \tag{2.1}$$

$$= \begin{cases} -i\left\langle\psi_0^N\middle|\hat{\psi}(\vec{r},t)\hat{\psi}^\dagger(\vec{r'},t')\middle|\psi_0^N\right\rangle\theta(t-t') \\ +i\left\langle\psi_0^N\middle|\hat{\psi}^\dagger(\vec{r'},t')\hat{\psi}(\vec{r},t)\middle|\psi_0^N\right\rangle\theta(t'-t) \end{cases} \tag{2.2}$$

$\hat{\psi}(\vec{r},t)$ and $\hat{\psi}^\dagger(\vec{r'},t')$ are the annihilation and creation field operators in the Heisenberg representation (i.e. $\hat{\psi}(\vec{r},t) = e^{i\hat{H}t}\hat{\psi}(\vec{r})e^{-i\hat{H}t}$, assuming $\hat{H}$ is time-independent), $\hat{T}$ is the time-ordering operator ($\hat{T}\left[\hat{\psi}(\vec{r},t)\hat{\psi}^\dagger(\vec{r'},t')\right] \overset{\text{def}}{=} \hat{\psi}(\vec{r},t)\hat{\psi}^\dagger(\vec{r'},t')\theta(t-t')-\hat{\psi}^\dagger(\vec{r'},t')\hat{\psi}(\vec{r},t)\theta(t'-t)$) and $\theta(t-t')$ the step function. The ground state wavefunction is assumed normalized, i.e. $\left\langle\psi_0^N\middle|\psi_0^N\right\rangle = 1$.
This definition is either valid for the interacting and non-interacting cases: the only difference is the ground state $\left|\psi_0^N\right\rangle$ used for the calculation of the expectation value.

Equation 2.1 has an immediate qualitative interpretation: for $t' > t$ we add a particle at time t' at position $\vec{r'}$ to the ground state $\left|\psi_0^N\right\rangle$ through the action of $\hat{\psi}^\dagger(\vec{r'},t')\left|\psi_0^N\right\rangle$; the (N+1) particle state just created propagates from t' to time t under the action of the time-independent hamiltonian $\hat{H}$. Lastly, we evaluate the overlap between the propagated state and the (N+1) particle state $\left\langle\psi_0^N\right|\hat{\psi}(\vec{r},t)$, which represents the *transition amplitude for the propagation of a test particle* added to the N particle ground state from $\vec{r'} \to \vec{r}$ during the interval $t'-t$.
On the other side, for $t > t'$ we *"add a test hole"*: that is, we study the transition amplitude for the propagation of a (N-1) particle state.
It's moreover possible to establish a relation between the single particle Green function and the density matrix. We recall the definition for the density matrix in second quantization:

$$\hat{n}(\vec{r},\vec{r'}) = \hat{\psi}^\dagger(\vec{r'})\hat{\psi}(\vec{r}) \tag{2.3}$$

The density matrix is then:

$$n(\vec{r},\vec{r'}) = \left\langle\psi_N^0\middle|\hat{n}(\vec{r},\vec{r'})\middle|\psi_N^0\right\rangle = iG(\vec{r},t,\vec{r'},t^+) \tag{2.4}$$

where t^+ denotes t plus an infinitesimal shift, i.e. $lim_{\eta\to 0}\ t+\eta$, with the purpose of select the right expression of the time ordering operator. Therefore the Green function can be considered a time-dependent generalization of the density matrix.

Fourier transforms of the Green function

We can quickly derive an expression for the Green function in other single particle basis. Let's consider the definitions of the field operators:

$$\hat{\psi}(\vec{r},t) \overset{\text{def}}{=} \frac{1}{\sqrt{\Omega}}\sum_{\alpha}\phi_\alpha(\vec{r})\hat{c}_\alpha(t) \qquad \hat{\psi}^\dagger(\vec{r'},t') \overset{\text{def}}{=} \frac{1}{\sqrt{\Omega}}\sum_{\alpha}\phi_\alpha(\vec{r})\hat{c}^\dagger_\alpha(t') \tag{2.5}$$

The expression for the Green function in term of the creation and annihilation operators associated to the basis $\{\phi_\alpha\}$ is therefore:

$$G(\vec{r},t,\vec{r'},t') = -i\sum_{\alpha,\alpha'}\phi_\alpha(\vec{r})\phi_{\alpha'}(\vec{r})\left\langle\psi_0^N\right|\hat{T}\left[\hat{c}_\alpha(t)\hat{c}^\dagger_{\alpha'}(t')\right]\left|\psi_0^N\right\rangle \tag{2.6}$$

We can also define the Fourier Transform with respect to the space variable $\vec{r}$ and $\vec{r'}$ [46, p. 62]:

$$G(\vec{r},t,\vec{r'},t') = \frac{1}{\Omega}\sum_{\vec{k}}\sum_{\vec{k'}}G(\vec{k},t,\vec{k'},t')e^{i(\vec{k}\vec{r}-\vec{k'}\vec{r'})} \tag{2.7}$$

A correspondence can be found between this formulation and the Green function as written in equation 2.6 on a plane wave basis $\phi_{\vec{k}} = \frac{1}{\sqrt{\Omega}}e^{i\vec{k}\cdot\vec{r}}$:

$$G(\vec{k},t,\vec{k'},t') = -i\left\langle\psi_0^N\right|\hat{T}\left[\hat{c}_{\vec{k}}(t)\hat{c}^\dagger_{\vec{k'}}(t')\right]\left|\psi_0^N\right\rangle \tag{2.8}$$

Let's now focus on the Fourier transform with respect to the time variables:

$$G(\vec{k},t,\vec{k'},t') = \frac{1}{2\pi}\iint d\omega d\omega' G(\vec{k},\omega,\vec{k'},\omega')e^{-i(\omega t-\omega' t')} \tag{2.9}$$

In a system with a translationally invariant hamiltonian, $G(\vec{r},t,\vec{r'},t')$ does not depend on $\vec{r}$ and $\vec{r'}$ separately but only on their difference $\vec{r}-\vec{r'}$ (that is $G(\vec{r},t,\vec{r'},t') = G(\vec{r}-\vec{r'},t,t')$). This implies that the Green Function becomes diagonal in $\vec{k},\vec{k'}$, i.e. $G(\vec{k},t,\vec{k'},t') = \delta_{\vec{k},\vec{k'}}G(\vec{k},t,t')$ [47, p. 124] and that:

$$G(\vec{r}-\vec{r'},t,t') = \frac{1}{\Omega}\sum_{\vec{k}}G(\vec{k},t,t')e^{i\vec{k}(\vec{r}-\vec{r'})} \tag{2.10}$$

Similarly, if the hamiltonian is translationally invariant in time, the Green function depends only on the difference $t-t'$ and non separately on t and t', and therefore becomes diagonal in ω and ω':

$$G(\vec{k},t-t') = \frac{1}{2\pi}\int d\omega G(\vec{k},\omega)e^{-i\omega(t-t')} \tag{2.11}$$

The Lehmann representation

It's possible to write the Green function of the interacting N particle system as a function of the excitation energies. For simplicity, let's consider a time independent and translationally invariant system (allowing us to use the diagonal Green function in reciprocal space $G(\vec{k}, t-t')$) and insert the completeness relation in *Fock space*:

$$\hat{1} = |vac\rangle \langle vac| + \sum_{m\geq 0} |\psi^1_m\rangle \langle \psi^1_m| + .. + \sum_{m\geq 0} |\psi^N_m\rangle \langle \psi^N_m| + .. \tag{2.12}$$

where $|\psi^N_m\rangle$ denotes the the *m-th* eigenstate of a system with N particles.
Thus:

$$G(\vec{k}, t-t') = \begin{cases} -i\theta(t-t') \sum_{m\geq 0} | \langle \psi^{N+1}_m | \hat{c}^\dagger_{\vec{k}'} | \psi^N_0 \rangle |^2 e^{-\frac{i}{\hbar}\left(E^{(N+1)}_m - E^{(N)}_0\right)(t-t')} \\ +i\theta(t'-t) \sum_{m\geq 0} | \langle \psi^{N-1}_m | \hat{c}^\dagger_{\vec{k}'} | \psi^N_0 \rangle |^2 e^{+\frac{i}{\hbar}\left(E^{(N-1)}_m - E^{(N)}_0\right)(t-t')} \end{cases} \tag{2.13}$$

This result can be obtained by remembering that the scalar products between wavefunctions with different particle number are equal to zero, and hence the only non-zero contributions come from states with $N+1$ and $N-1$ particles.
Now we employ the integral representation equation of the (Heaviside) step function:

$$\theta(\tau) = \lim_{\eta\to 0^+} -\frac{1}{2\pi i} \int_{-\infty}^{+\infty} d\omega \frac{e^{-i\omega\tau}}{\omega + i\tau} \tag{2.14}$$

obtaining:

$$G(\vec{k}, t-t') = \lim_{\eta\to 0^+} \frac{1}{2\pi} \int_{-\infty}^{+\infty} d\omega e^{-i\omega(t-t')} \left[\sum_{m\geq 0} \frac{| \langle \psi^{N+1}_m | \hat{c}^\dagger_{\vec{k}'} | \psi^N_0 \rangle |^2}{\omega - \frac{1}{\hbar}\left(E^{(N+1)}_m - E^(_0N)\right) + i\eta} \right.$$
$$\left. + \sum_{m\geq 0} \frac{| \langle \psi^{N-1}_m | \hat{c}_{\vec{k}'} | \psi^N_0 \rangle |^2}{\omega + \frac{1}{\hbar}\left(E^{(N-1)}_m - E^(_0N)\right) - i\eta} \right]$$

Recalling equation 2.11 we find the *Lehmann representation*:

$$G(\vec{k}, \omega) = \lim_{\eta\to 0^+} \sum_{m\geq 0} \frac{| \langle \psi^{N+1}_m | \hat{c}^\dagger_{\vec{k}'} | \psi^N_0 \rangle |^2}{\omega - \frac{1}{\hbar}\left(E^{(N+1)}_m - E^{(N)}_0\right) + i\eta} + \sum_{m\geq 0} \frac{| \langle \psi^{N-1}_m | \hat{c}_{\vec{k}'} | \psi^N_0 \rangle |^2}{\omega + \frac{1}{\hbar}\left(E^{(N-1)}_m - E^{(N)}_0\right) - i\eta} \tag{2.15}$$

We define the two *spectral functions* and reformulate $G(\vec{k}, \omega)$ through these functions:

$$A_+(\vec{k}, \omega) \overset{\text{def}}{=} \sum_{m\geq 0} | \langle \psi^{N+1}_m | \hat{c}^\dagger_{\vec{k}'} | \psi^N_0 \rangle |^2 \delta \left[\omega - \frac{1}{\hbar}\left(E^{(N+1)}_m - E^{(N)}_0\right) \right] \tag{2.16}$$

$$A_-(\vec{k}, \omega) \overset{\text{def}}{=} \sum_{m\geq 0} | \langle \psi^{N-1}_m | \hat{c}_{\vec{k}'} | \psi^N_0 \rangle |^2 \delta \left[\omega + \frac{1}{\hbar}\left(E^{(N-1)}_m - E^{(N)}_0\right) \right] \tag{2.17}$$

$$G(\vec{k}, \omega) = \lim_{\eta\to 0^+} \int_{-\infty}^{+\infty} d\omega' \left[\frac{A_+(\vec{k}, \omega)}{\omega - \omega' + i\eta} + \frac{A_-(\vec{k}, \omega)}{\omega + \omega' - i\eta} \right] \tag{2.18}$$

$A(\vec{k},\omega) \overset{\text{def}}{=} A_+(\vec{k},\omega) + A_-(\vec{k},\omega)$ is called *spectral function.* A_- and A_+ are real, positive and and equal to zero for $\omega < 0$:

$$A_+(\vec{k},\omega) = A_+^*(\vec{k},\omega) \geq 0 \qquad A_-(\vec{k},\omega) = A_-^*(\vec{k},\omega) \geq 0 \tag{2.19}$$

$$A_+(\vec{k},\omega) = 0 = A_-(\vec{k},\omega) \;\text{ for } \omega < 0 \tag{2.20}$$

and their sum satisfies the *sum rule*:

$$\int_0^\infty d\omega A(\vec{k},\omega) = 1 \tag{2.21}$$

Due to the two properties above, $A(\vec{k},\omega)$ can be formally interpreted *as a probability density.* We will give a physical intuition to it in the next paragraph.
The interacting Green function has poles at the exact excitation energies, defined as the addition or removal energies and involving the *exact* eigenvalues of the N and $N+1$ system. These energies comprehend the correlation effects and the orbital relaxations (following the electrons addition or removal) which were neglected in the Hartree Fock theory (chapter 1.3.1). This is an important and nice result.

We state also another expression for G that will be useful later:

$$G(\vec{r},\vec{r'},\omega) = \lim_{\eta\to 0^+} \sum_{m\geq 0} \frac{\Psi_m^{N+1}(\vec{r})\Psi_m^{N+1*}(\vec{r})}{\omega - \frac{1}{\hbar}\left(E_m^{(N+1)} - E_0^{(N)}\right) + i\eta} + \sum_{m\geq 0} \frac{\Psi_m^{N-1}(\vec{r})\Psi_m^{N-1*}(\vec{r})}{\omega + \frac{1}{\hbar}\left(E_m^{(N-1)} - E_0^{(N)}\right) - i\eta} \tag{2.22}$$

where $\Psi_m^M(\vec{r}) = \langle \psi_m^M | \hat{\psi}^\dagger(\vec{r}) | \psi_0^N \rangle$ ($\hat{\psi}^\dagger(\vec{r})$ is the field operator, defined in equation 2.5). To obtain this expression we start from the Lehmann representation (equation 2.15)[1], insert it inside the Fourier transform formula (equation 2.1) and apply the definition of the field operator (equation 2.5) implemented on a plane wave basis $(1/\sqrt{\Omega})e^{i\vec{k}\cdot\vec{r}}$.

2.1.1 The interpretation of $A(\vec{k},\omega)d\omega$: excited states and quasiparticles

It's possible to give a very clear interpretation to the spectral function $A(\vec{k},\omega) = A_+(\vec{k},\omega) + A_-(\vec{k},\omega)$ in the Lehmann representation.
First of all we point out that, while $\left|\psi_m^{(N+1)}\right\rangle$ and $\left|\psi_m^{(N)}\right\rangle$ are eigenstates respectively of the N and $N+1$ interacting particle systems, $\hat{c}_{\vec{k}'}^\dagger \left|\psi_0^N\right\rangle$ *is not* an eigenstate of the interacting system. Therefore it has finite lifetime[2] and propagates as a superposition of N+1 particle eigenstates $\left|\psi_m^{(N+1)}\right\rangle$.
The modulus $|\langle \psi_m^{N+1} | \hat{c}_{\vec{k}'}^\dagger | \psi_0^N \rangle|^2$ represents the component of the state $\hat{c}_{\vec{k}'}^\dagger \left|\psi_0^N\right\rangle$ over the excited eigenstates. Therefore $A(\vec{k},\omega)$ represents the normalized density of states with

---

[1] The Lehmann expression given in equation 2.15 is diagonal in the momentum; to obtain equation 2.22 however we employ a slightly different version of it, i.e. the non diagonal one $G(\vec{k},\vec{k'},\omega)$.

[2] the only case where $\hat{c}_{\vec{k}'}^\dagger \left|\psi_0^N\right\rangle$ is a eigenstate is when the system is not interacting.

energy in the interval $[\omega, \omega + d\omega]$ which are involved in the propagation of an added particle with momentum $\vec{k}$ [48, p. 35]. Other authors[49, p. 280] describe qualitatively $A(\vec{k}, \omega)d\omega$ as the probability of being able to create an excitation with wavevector $\vec{k}$ and energy in the interval $[\hbar\omega, \hbar\omega + \hbar d\omega]$.

We explore now the quasiparticle concept and answer the question *Under which circumstances is it possible to consider the additional state (created by $\hat{c}^\dagger_{\vec{k}}$) as a separate particle that propagates in the system?* This is the exactly idea behind the *quasiparticle picture*; that is, to *approximate* the description of a strongly interacting system with a description in term of a new type of particles, which reproduces (approximately) the same physics. These particles are weakly interacting, have different properties and are called *quasiparticles*.

We start from the Green function of a non interacting electron system (that we can obtain directly from the definition 2.1 by replacing $\left|\psi_0^N\right\rangle$ with the non interacting ground state):

$$G_0(\vec{k}, t - t') = -ie^{-iE_{\vec{k}}(t-t')/\hbar}\left[\theta(t - t')\theta(k - k_F) - \theta(t' - t)\theta(k_F - k)\right] \tag{2.23}$$

$$\Downarrow$$

$$G_0(\vec{k}, \omega) = \lim_{\eta \to 0^+} \frac{\theta(k - k_F)}{\omega - \frac{1}{\hbar}E_{\vec{k}} + i\eta} + \frac{\theta(k_F - k)}{\omega - \frac{1}{\hbar}E_{\vec{k}} - i\eta} \tag{2.24}$$

and this is the *Lehmann representation* for the non interacting Green function (k is used for $k = |\vec{k}|$). The spectral functions are therefore:

$$A_+(\vec{k}, \omega) = \theta(k - k_F)\delta(\omega - \frac{1}{\hbar}E_{\vec{k}}) \tag{2.25}$$

$$A_-(\vec{k}, \omega) = \theta(k_F - k)\delta(\omega - \frac{1}{\hbar}E_{\vec{k}}) \tag{2.26}$$

We can now restate the question: to behave in an *approximate free particle way*, the interacting Green function must be similar to the non interacting one during the quasiparticle lifetime:

$$G(\vec{k}, t) \approx -iZ_{\vec{k}}e^{-i\tilde{E}(\vec{k})t/\hbar}e^{-\Gamma_{\vec{k}}t} + G_{incoherent}(\vec{k}, t) \tag{2.27}$$

The term $e^{-\Gamma_k t}$ represents the fact that this approximation holds only during a finite time interval ($\hat{c}^\dagger_{\vec{k}'}\psi_0^N$ is not an eigenstate of the interacting system): we define the quasiparticle lifetime as $1/\Gamma_{\vec{k}}$.

In summary, we have seen that for a non interacting system the spectral functions are represented by Dirac deltas. The interaction however is going to broaden the peaks; nonetheless, to preserve the form 2.27, $A(\vec{k}, \omega)$ must be similar to equations 2.25 and 2.26 and hence *must* still exhibit a peaked structure over a continuous incoherent background.

A typical lineshape of a quasiparticle peak, characteristic of a *Fermi liquid*, is the Lorentzian one:

$$A(\vec{k}, \omega) \approx Z_{\vec{k}} \frac{\Gamma_{\vec{k}}}{\omega - \frac{1}{\hbar}\left(E_{\vec{k}} - \Delta E_{\vec{k}}\right)^2 + \Gamma^2_{\vec{k}}} + A_{incoherent}(\vec{k}, \omega) \tag{2.28}$$

The area under the peak is equal to $Z_{\vec{k}}$ and the (complex) energies $E^{QP}_{\vec{k}} \stackrel{\text{def}}{=} E_{\vec{k}} - \Delta E_{\vec{k}}$ are renormalized with respect to the non interacting ones $E_{\vec{k}}$; The width of the peak

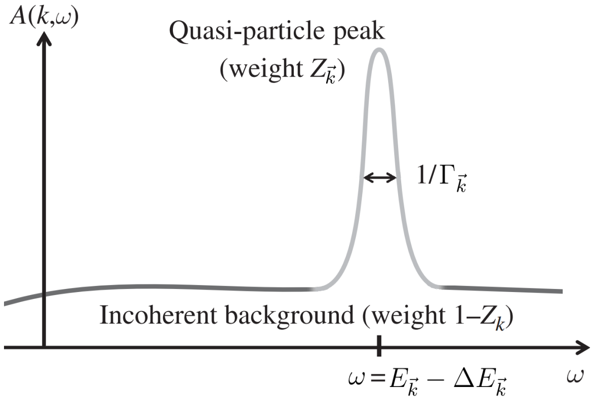

Figure 2.1: Qualitative picture of the spectral function: we can recognize the peak over an incoherent background.

Γ_k is equal to the inverse lifetime of the quasiparticle. A schematic representation of the spectral function in this approximation can be seen in figure 2.1.
We have therefore characterized the expression of $A(\vec{k},\omega)$ by the initial requirement on $G(\vec{k},t)$: *if* $A(\vec{k},\omega)$ *satisfies this constraint the quasiparticle approximation holds.*

We can think about these quasiparticles as bare particles carrying along a cloud of neighbouring particles that changes their properties. It's important to note that, while G in principle contains all information necessary to fully characterize the properties of a quasiparticle, it carries *no* information concerning the interaction between quasiparticles.

2.1.2 The Dyson equation and the quasiparticle equation

In the previous paragraph we have studied the formal properties of the Green function, but we haven't so far found a way to calculate G, because the definition involves the unknown interacting ground state $\left|\psi_0^N\right\rangle$.
Moreover, we are also interested in the excited quasiparticle energies: we can in principle determine them as poles of the Lehmann representation of the Green function itself. However, it would be more convenient to obtain them as a solution of an equation in a similar way to the ones defined for the *DFT* (equation 1.21) and Hartree Fock (equation 1.5).

The first step to derive an equation of this kind is the *Dyson equation*, which connects the Green function of the interacting system with the one belonging to the non interacting system:

$$G(\vec{r},\vec{r'},\omega) = G_0(\vec{r},\vec{r'},\omega) + \iint d\vec{r_1} d\vec{r_2} G_0(\vec{r},\vec{r_1},\omega)\Sigma(\vec{r_1},\vec{r_2},\omega)G_0(\vec{r},\vec{r_2},\omega) \tag{2.29}$$

Although the expression in momentum and frequency space is more common:

$$G(\vec{k},\omega) = G_0(\vec{k},\omega) + G_0(\vec{k},\omega)\Sigma(\vec{k},\omega)G(\vec{k},\omega) \tag{2.30}$$

The newly defined $\Sigma(\vec{r},\vec{r'},\omega)$ is the so-called *self-energy*, a non local, non hermitian and frequency dependent operator which contains all many body exchange and correlation

contributions. We will devote an entire section to analyze and understand it.
By iterating the Dyson equation we define the Dyson series:

$$G = G_0 + G_0 \Sigma G_0 + G_0 \Sigma G_0 \Sigma G_0 + .. \tag{2.31}$$

We can solve it with respect to the interacting G[3]:

$$G(\vec{k},\omega) = \frac{G_0(\vec{k},\omega)}{G_0(\vec{k},\omega) - \Sigma(\vec{k},\omega)} \tag{2.32}$$

and, finally, by substituting the explicit expression of G_0:

$$G(\vec{k},\omega) = \frac{1}{\omega - \frac{1}{\hbar}E_{\vec{k}} + i\eta - \Sigma(\vec{k},\omega)} \tag{2.33}$$

we have hence expressed G through G_0 (which is known) and through Σ (which on the contrary is *unknown*). Because we have not yet presented a way to calculate Σ, the question *"how we can calculate G?"* is not yet solved: in the next sections we will introduce different methods.
For one thing, equation 2.33 allows us to give a precise meaning to the quantities $\Delta E_{\vec{k}}$ and $\Gamma_{\vec{k}}$ which characterize a quasiparticle peak (equations 2.27 and 2.28). The Green function described has a pole at $\omega \approx \frac{1}{\hbar}E_{\vec{k}} - i\eta + \Sigma(\vec{k}, E_{\vec{k}}/\hbar)$, which implies $\Delta E_{\vec{k}} = \hbar\,\mathrm{Re}\left[\Sigma(\vec{k}, E_{\vec{k}}/\hbar)\right]$, $\Gamma_{\vec{k}} = \hbar/\,\mathrm{Im}\left[\Sigma(\vec{k}, E_{\vec{k}}/\hbar)\right]$.

Let's now focus on the quasiparticle equation anticipated at the beginning of the paragraph. Starting form the Lehmann representation (equation 2.22) and the Dyson equation we find[50, Appendix B]:

$$\sum_{m\geq 0} \frac{\Psi^*_m(\vec{r'})}{\hbar\omega - \epsilon_m - +i\eta} \left[\left[\hbar\omega - \hat{h}_0(\vec{r})\right] \Psi_m(\vec{r}) - \int d\vec{r_1} \Sigma(\vec{r},\vec{r_1},\omega)\Psi_m(\vec{r_1}) \right] = \delta(\vec{r} - \vec{r'}) \tag{2.34}$$

where $\epsilon_m = E^{(N+1)}_m - E^{(N)}_0$ and $\hat{h}_0$ is the hamiltonian associated with the non interacting Green function (which takes into account only the Hartree contribution). From this we finally find the *quasiparticle equation*, which is the purpose of this paragraph:

$$\left[-\frac{\hbar^2}{2m}\nabla^2 + v_{ext}(\vec{r}) + \frac{1}{2}\int d\vec{r} \frac{n(\vec{r'})}{|\vec{r} - \vec{r'}|} \right] \Psi_m(\vec{r}) + \int d\vec{r'} \Sigma\left(\vec{r},\vec{r'},\frac{\epsilon_m}{\hbar}\right) \Psi_m(\vec{r}) = \epsilon_m \Psi_m(\vec{r}) \tag{2.35}$$

the amplitude $\Psi_m(\vec{r})$ and the quasiparticle energies were defined in equation 2.22. The real parts of the QP-energies ϵ_m describe the positions of the quasiparticle peaks, while the imaginary parts $\mathrm{Im}(\epsilon_i)$ describe their lifetimes.
The equation is nonlinear in ϵ_i (because ϵ_i appears ar argument of Σ) and is the analogue of the equation 1.21 and 1.5 for DFT and Hartree-Fock. However this equation does *not* constitute a mean-field approach, and can reproduce the exact excitation energies. Lastly, Σ has an analogous role of the exchange-correlation potential v_{xc} in the *DFT* formalism.

---

[3] this is formally equivalent to sum the infinitely many terms in the Dyson series.

2.2 The Self energy Σ: diagrammatic approach

The perturbation expansion, briefly discussed in this section, gives a first interpretation of the self energy.
The procedure to obtain the result presented in this section is quite cumbersome and will therefore be omitted. We split the many body hamiltonian in the non interacting part $\hat{H}_0$ plus the interaction part $\hat{H}_I$, which is considered as a perturbation and is described in the Dirac picture. The main result is:

$$
\begin{aligned}
G(\vec{k}, t-t') = & \frac{-i}{\left\langle \psi_0^{(N)} \middle| \hat{U}(-\infty, +\infty) \middle| \psi_0^{(N)} \right\rangle} \sum_{n=0}^{\infty} \frac{1}{n!} \frac{1}{(i\hbar)^n} \int_{-\infty}^{\infty} dt_1 \int_{-\infty}^{\infty} dt_2 .. \int_{-\infty}^{\infty} dt_n \\
& \times \left\langle \psi_0^{(N)} \middle| \hat{T} \left[\hat{c}_{\vec{k}}(t) \, \hat{H}_I(t_1) \hat{H}_I(t_2) .. \hat{H}_I(t_n) \, \hat{c}^{\dagger}_{\vec{k}}(t') \right] \middle| \psi_0^{(N)} \right\rangle \qquad (2.36)
\end{aligned}
$$

where $\hat{T}$ is the time ordering operator and $\hat{U}$ is the time evolution operator (in the Dirac picture). The integrand is evaluated through *Wick's theorem*, and reduces to a product of non interacting Green function.

It's possible to associate to every term in the sum a pictorial representation, known as *Feynman diagrams*. Remember that $G_0(\vec{k}, t-t')$ describes the propagation of an electron created at time t' with wavevector $\vec{k}$ and destroyed or measured at time t; this is associated to a straight line:

Figure 2.2: Association between a straight line and a non interacting Green function G_0 in a Feynman diagram.

The interaction potential is instead usually denoted by a wavy line (〰), and the double line (═►═) represents the interacting Green function. A set of rules exists to recover the integral formulation from the pictorial one and vice-versa. We can reformulate the Dyson equation through Feynman diagrams:

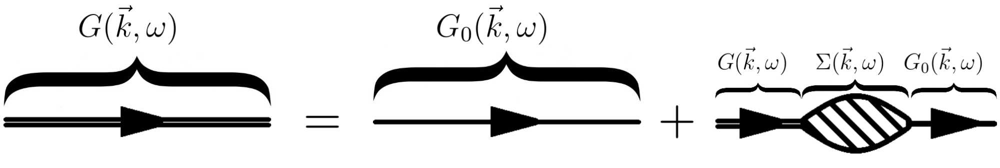

Figure 2.3: Dyson equation in Feynman representation.

The perturbation expansion provides also an explicit definition for the self energy, that is as *the sum of all diagrams that cannot be split in two by breaking a single fermion line*, as showed in figure 2.4:

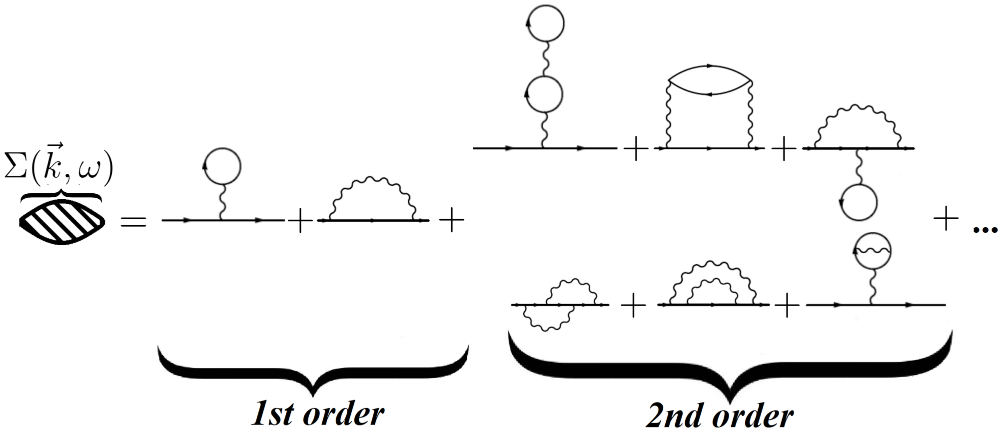

Figure 2.4: The first two order of diagrams contributing to the self energy term. The order of a given diagram is defined by the number of wavy lines (〰〰).

2.3 The GW Approximation

A systematic procedure to determine the self energy and the interacting Green function was developed by Hedin in his seminal paper[51]. This scheme, derived through Schwinger's functional derivative technique, is composed of five coupled integral equations, usually called *Hedin equations*:

$$\Sigma(1,2) = i\int d(3,4)G(1,3)\Gamma(3,2,4)W(4,1^+) \tag{2.37}$$

$$G(1,2) = G_0(1,2) + \int d(3,4)G_0(1,3)\Sigma(3,4)G(4,2) \tag{2.38}$$

$$W(1,2) = v(1,2) + \int d(3,4)v(1,3)P(3,4)W(4,2) \tag{2.39}$$

$$P(1,2) = -i\int d(3,4)G(1,3)G(4,1^+)\Gamma(3,4,2) \tag{2.40}$$

$$\Gamma(1,2,3) = \delta(1,2)\delta(1,3) + \int d(4,5,6,7)\frac{\delta\Sigma(1,2)}{\delta G(4,5)}G(4,6)G(7,5)\Gamma(6,7,3) \tag{2.41}$$

where we used the notation $1 = (\vec{r}_1, \sigma_1, t_1), 1^+ = (\vec{r}_1, \sigma_1, t_1+\delta)$ with δ positive infinitesimal. The physical quantities involved in Hedin equation are:

1. The self energy Σ (equation 2.37) and the interacting Green function G (Dyson equation 2.38 in position and time space); G_0 is non interacting (and known) Green function.

2. The *irreducible polarizability* P (equation 2.40).

3. The *screened interaction* W (equation 2.39).

4. The *vertex function* Γ.

These equation *are exact* and must be solved self-consistently. A straight numerical implementation is computationally too cumbersome and expensive, and some approximations are required. The most used, the *GW approximation*, assumes the vertex function Γ to be diagonal in space and time coordinates:

$$\Gamma(1,2,3) = \delta(1,2)\delta(1,3) \tag{2.42}$$

Hedin equation became in this approximation:

$$\Sigma(1,2) = iG(1,2)W(1^+,2) \tag{2.43}$$

$$G(1,2) = G_0(1,2) + \int d(3,4)G_0(1,3)\Sigma(3,4)G(4,2) \tag{2.44}$$

$$W(1,2) = v(1,2) + \int d(3,4)v(1,3)P(3,4)W(4,2) \tag{2.45}$$

$$P(1,2) = -iG(1,2)G(2,1^+) \tag{2.46}$$

$$\Gamma(1,2,3) = \delta(1,2)\delta(1,3) \tag{2.47}$$

We now discuss the physical meaning of the various quantities and the effect of the approximation itself.

The Screened Interaction W

The *effective classical electrostatic interaction* in an polarizable system is not the bare interaction $v(1,2)$ but the screened one $W(1,2)$, which represents the classical screened potential at 2 generated by a charge in 1. We remark again that it contains only the classical (Hartree) potential: the exchange-correlation correction to the screening potential is described by Γ[52, p. 250]: its introduction changes the effective (screened) interaction from W to $W\Gamma$.

The Irreducible Polarizability P and the Vertex Correction Γ

P describes the change of the density δn in 1 upon a small perturbation of the total classical potential δv_{tot} evaluated in 2 [52, p. 247] (δv_{tot} is given by the sum of an external potential δv_{ext} plus the variation of the Hartree potential δv_H: $\delta v_{tot} = \delta v_{ext} + \delta v_H$) :

$$P(1,2) \overset{\text{def}}{=} -i\frac{\delta G(1,1^+)}{\delta v_{tot}(2)} = \frac{\delta n(1)}{\delta v_{tot}} \tag{2.48}$$

where we used equation 2.4. By employing the definition of the functional derivative ($\delta F \overset{\text{def}}{=} \int dx\, [\delta F/\delta f(x)]\, \delta f(x)$), it can be proved that this is equivalent to $\delta n(1) = \int d(2)P(1,2)v_{tot}(2)$.

The connection between δv_{tot} and δv_{ext} is given by the *inverse dielectric function*:

$$\epsilon^{-1}(1,2) = \frac{\delta v_{tot}(1)}{\delta v_{ext}(2)} \tag{2.49}$$

The polarization of the medium, as described by the Hedin equation 2.40 for P, results from the creation of pairs of particles at time 1 described by the two Green function. The idea is that the electron addition / removal excites the system through the formation of electron-hole pairs (*neutral* excitations). In particular, if $t_3 = t_4$ the couple is formed by an electron and a hole[4]. For simplicity, in the following discussion we restrict to this electron-hole pair case.

All contributions to the polarization come therefore from these particle pairs (following the perturbation) and *give rise to the screening of the perturbation.*

In section 2.1.1 we have briefly described a quasiparticle as a bare particle plus a polarization cloud; equation 2.40 tells us that this polarization cloud *is formed by* these

---

[4] otherwise t_3 and t_4 could lie on different sides of t_1 which implies the same time ordering for the two Green function

electron hole pairs (at least in the description given by this approach).

A first role of the vertex function Γ *is to describe how (and if) the particles inside a given pair interact.* In fact the vertex function Γ couples the two particles in a given pair and describe how they interact, including exchange-correlation effects[52, p. 250][53, p. 250] and excitonic effects[54, p. 619] (if the couple is formed by an electron and a hole).
The GW approximation decouples the two Green functions and imposes $t_3 = t_4 = t_2$: thus P becomes *constituted by two Green functions describing a cloud of non interacting electron-hole pair.*

There is an important result concerning P in the GW approximation. We start by Fourier transforming it to the coordinate and frequency space:

$$P^{GW}(\vec{r}, \vec{r'}, \omega) = -\frac{i\hbar}{2\pi} \int d\omega' G(\vec{r}, \vec{r'}, \omega - \omega') G(\vec{r}, \vec{r'}, \omega') \tag{2.50}$$

From this we can determine an explicit expression[54, p. 618][55, p. 41] :

$$P_0^{GW}(\vec{r}, \vec{r'}, \omega) = P^{RPA}(\vec{r}, \vec{r'}, \omega) \overset{\text{def}}{=} \sum_{ij} (f_i - f_j) \frac{\psi_i(\vec{r})\psi_j^*(\vec{r})\psi_j(\vec{r'})\psi_i^*(\vec{r'})}{\omega - \frac{1}{\hbar}(\epsilon_i - \epsilon_j) + i\eta} \tag{2.51}$$

This expression is formally equal to the RPA polarization; this is in fact the same result originally developed by Bohm and Pines[56] to study the density oscillations in the homogeneous electron gas. Hubbard[57] showed that the Bohm–Pines approach provides similar results as the perturbative expansion in bubble diagrams for the dielectric function. Ehrenreich and Cohen[58] employed a linearised time dependent Hartree approach, which was proved equivalent to the *RPA*, to calculate the frequency dependent dielectric function and other quantities. Andler and Wiser[59, 60] expanded this approach some years later.
This expression can be usually interpreted as a *sum over independent transitions* (each one identified by the couple of quantum number i, j).
Moreover, the *RPA* polarization (being equivalent to the *GW* approximation) contains the electron-electron interaction only through the classical Coulomb interaction with the polarization charges and neglects the short-range effects due to exchange and correlation[61, p. 13,19].

The Self Energy Σ

We have already introduced the self energy Σ in section 2.1.2, where we noted its role as "generalized" exchange-correlation potential in the quasiparticle equation. In this paragraph we'll analyze the self energy in the *GW* approximation through successive approximations and comparisons with the Hartree Fock approach. Before discussing the various approximation, we recall the Fourier transform of Σ to frequency variables:

$$\Sigma^{GW}(\vec{r}, \vec{r'}, \omega) = \frac{i}{2\pi} \int d\omega' W(\vec{r}, \vec{r'}, \omega) G(\vec{r}, \vec{r'}, \omega + \omega') \tag{2.52}$$

To understand what are the consequences of screened interaction presence in Σ^{GW}

we briefly examine the first approximation, the *Screened Exchange Approximation* (*SEX*). This approximation neglects the frequency (or energy) dependence of W, i.e. $W(\vec{r}, \vec{r'}, \omega) \approx W(\vec{r}, \vec{r'}, \omega = 0)$ (therefore, being constant with respect to ω, only the poles in G provide contributions to the integral in equation 2.52). The approximation is equivalent to neglect the non-locality in time of W and replace it with an instantaneous interaction:

$$\Sigma^{SEX}(\vec{r}, t, \vec{r'}, t') = G(\vec{r}, t, \vec{r'}, t')W(\vec{r}, \vec{r'}, \omega = 0)\delta(t' - t^+) \tag{2.53}$$

It can be proved[52, p. 229][55, p. 36] that the Hartree Fock self energy is $\Sigma^{HF}(1, 2) = G(1, 2)v(1^+, 2)$ where v is the classical Coulomb interaction. Thus the *Screened Exchange Approximations* replaces the bare (and static) Coulomb potential in Σ^{HF} with a (static) screened potential, and hence can be understood as as *statically screened Hartree Fock* operator. Static screening contains the information about the relaxation after an electron addition/removal [52, p. 254], and is *one of the fundamental aspects of the GW method that are absent in the Hartree Fock Approach.* We have discussed in section 1.3.1 that Hartree Fock approach doesn't describe the relaxation effects upon electron addition; the polarization (and thus the screening) in the Green function approach represents these effects.

However, a proper integration in equation 2.52 would of course receives contributions also from the W poles. Therefore in the static limit Σ can be written as a sum of two contribution[52, p. 254][55] $\Sigma^{SEX}(\vec{r}, \vec{r'}) + \Sigma^{COH}(\vec{r}, \vec{r'})$, where Σ^{SEX} is given by equation 2.53 and Σ^{COH} is:

$$\Sigma^{COH}(\vec{r}, \vec{r'}, \omega) = \frac{1}{2}\delta(\vec{r} - \vec{r'})W^p(\vec{r}, \vec{r'}, \omega = 0) \tag{2.54}$$

where $W^p \overset{\text{def}}{=} W - v_c$ is called the polarization contribution. This second term, *local and static in space*, is called *COulomb Hole* contribution, and the approximation $\Sigma^{COHSEX} = \Sigma^{SEX} + \Sigma^{COH}$ is called *COulomb Hole plus Screened Exchange* (*COHSEX*). Σ^{COH} is the effect of the polarization of the system due a static Coulomb potential hole which is induced by a single hole or electron; the charge is represented classically as a point charge.

The *COHSEX* approximation, while being quite crude, captures some fundamental contributions to the self energy, that is the exchange one and the static screening of a point charge.
However, the dynamical properties of W (i.e. the *frequency dependence of the self-energy*) are not described by this approximation. This is *another important aspect that distinguish the GW approximation from Hartree Fock and any other static mean-field theory.* It can be proved[52, p. 255] that, taking into account these properties, the Coulomb hole (described by Σ^{COH}) became non-local and non-static (depending hence on ω).

2.4 GW implementation

The numerical implementation of the *GW* method relies on the quasiparticle equation 2.35 and make use of different approximations:

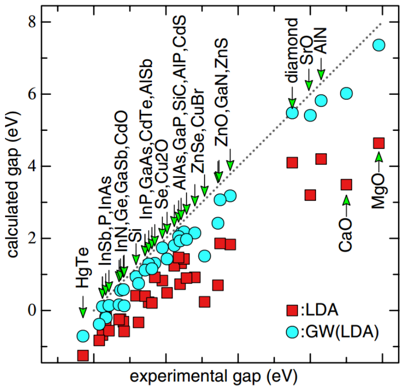

Figure 2.5: band gap comparison between *DFT@LDA* and *G0W0* starting from *LDA*. From [62].

1. We employ the first order perturbation to approximate the quasiparticle energies:

$$\epsilon_i \approx \epsilon_i^{KS} + \langle \psi_i^{KS} | \Sigma(\epsilon_i/\hbar) - v_{xc} | \psi_i^{KS} \rangle \tag{2.55}$$

This approximation is justified by the similarity between the quasiparticle and the Kohn-Sham wavefunction[5].

2. The self energy depends on ϵ_i too; to avoid this dependence (which would make the equation self consistent) and to simplify the equation we adopt the Taylor expansion:

$$\Sigma(\vec{r}, \vec{r'}, \epsilon_i/\hbar) = \Sigma(\vec{r}, \vec{r'}, \epsilon_i^{KS}/\hbar) + \frac{\epsilon_i - \epsilon_i^{KS}}{\hbar} \frac{\partial \Sigma(\vec{r}, \vec{r'}, \omega)}{\partial \omega}\Big|_{\hbar\omega = \epsilon_i^{KS}} + O\left(\left(\epsilon_i - \epsilon_i^{KS}\right)^2 \right) \tag{2.56}$$

which implies that

$$\epsilon_i \approx \epsilon_i^{KS} + Z_i \langle \psi_i^{KS} | \Sigma(\epsilon_i^{KS}/\hbar) - v_{xc} | \psi_i^{KS} \rangle \tag{2.57}$$

where the quasiparticle renormalization factor Z_i is given by:

$$Z_i = \left[1 - \langle \psi_i^{KS} | \frac{\partial \Sigma(\vec{r}, \vec{r'}, \omega)}{\partial \omega}\Big|_{\omega = \epsilon_i^{KS}} | \psi_i^{KS} \rangle \right]^{-1} \tag{2.58}$$

To determine $\Sigma(1,2)$ we employ the Hedin equation in the *GW* approximation, with a series of further approximations:

1. as a starting point for $G(1,2)$ we use the non interacting Green function build from the Kohn-Sham energies and wavefunctions.
2. Moreover P is evaluated from the *RPA* form (expression 2.51) starting from the Kohn-Sham energies and wavefunctions. From P^{RPA} we evaluate the frequency dependent dielectric function and the screened interaction W.

Moreover, *GW* implementations differentiate themselves by the level of self-consistency secured:

1. update G self-consistently while keeping W at the *RPA* expression: the *GW0* approach.
2. update both G and W self-consistently through Hedin equation (or some derived set of equation): the full *GW* approach.

---

[5] For discussion on this approximations' validity, see [63, 64].

3. do not iterate self-consistently at all, keeping both G and W fixed at the starting entries: the $G0W0$ approach. Despite the numerous approximations, the $G0W0$ method succeeds in correcting the bandgap problem of DFT, as we can see from figure 2.5, taken from [62].

An in detail explanation of the different GW implementations in $VASP$ can be found in [65, 66, 67].

Chapter 3

The Bethe-Salpeter equation

It's known that the correlated electron-hole excitations have a important role in the optical properties of many materials, especially semiconductors and insulators. One way to incorporate them is to go beyond the RPA in the GW approximations by including the vertex correction[68]. Another approach (which is equivalent to partially include the vertex corrections, as we will briefly mention later) starts from the two-particle Green function:

$$G(1,2,1',2') \overset{\text{def}}{=} (-i)^2 \left\langle \psi_0^N \middle| \hat{T} \left[\psi(1)\psi(1')\psi^\dagger(2')\psi^\dagger(2) \right] \middle| \psi_0^N \right\rangle \tag{3.1}$$

which describes the propagation of two particles, which can be either two electrons, two holes or an electron-hole pair. From this equation we define the 4-particle *reducible* polarizability L:

$$L(1,2,1',2') \overset{\text{def}}{=} L^0(1,2,1',2') - G(1,2,1',2') \tag{3.2}$$

where L^0 is the independent-electron polarizability $L_0(1,2,1',2') \overset{\text{def}}{=} iG(1,1')G(2',2)$ which, in a similar way to $P^{RPA}(1,2) = -iG(1,2)G(2,1)$, describes the polarization due to the independent propagation of two particles (electrons or holes).
This function satisfies a *Dyson-like* equation, the *Bethe-Salpeter equation*:

$$L(1,2,1',2') = L^0(1,2,1',2') + \int d(3,4,3',4')L^0(1,2,3',4')K(3,4,3',4')L(3',4',1',2') \tag{3.3}$$

where the kernel K is

$$K(3,4,3',4') = \delta(3,4)\delta(3',4')v_c(3,3') + i\frac{\delta\Sigma(3,3')}{\delta G(4,4')} \tag{3.4}$$

The Bethe-Salpeter equation thus describes the propagation of two interacting and coupled particles, and the kernel K defines the effective interaction between the two. Note that[52, p. 349] in equation 2.40 $P = -iGG\Gamma$ the electron-hole coupling is introduced by the vertex function; here, the variation of the exchange-correlation self energy introduces this coupling through K.

To solve equation 3.4, however, we need to specify the term $\delta\Sigma(3,3')/\delta G(4,4')$ inside the kernel. From this point different approximations depart: if we substitute $\Sigma(3,3')$ with a local and instantaneous potential such as the Kohn-Sham exchange-correlation

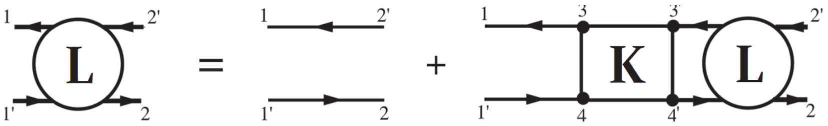

Figure 3.1: Diagrammatic expression for the Bethe-Salpeter equation 3.4, describing the coupled motion of an electron hole pair.

one, $\Sigma(3,3') \approx \delta(3,3')v_{xc}(3)$, and utilize the Kohn-Sham Green function we find the linear response screening equation of *TDDFT* (*Time-Dependent DFT*), the so-called *Casida equation*[69]. This approach is less demanding from a computational point of view, because it reduces the four-arguments equation to two-arguments (single-particle) one.
Another approach based on a mean-field theory employs the non local (but instantaneous in time) Fock exchange together with the Hartree-Fock Green function: this leads to the *linear response time-dependent Hartree Fock*[70].

A better approximation would be to start from the GW self energy $\Sigma(1,2) = iG(1,2)W(1,2)$. Carrying out the derivative we find:

$$\frac{\delta\Sigma^{GW}(3,3')}{\delta G(4,4')} = i\delta(3,4')\delta(3',4)W(3,3') + iG(3,4)\frac{\delta W(3,4)}{\delta G(4',3')} \tag{3.5}$$

The second term, which represents the variation of the screening due to the excitation, is supposed to be small and can be neglected[71, 72]; intuitively, the first term is first order in W, while it can be proved that the second term contains only higher orders of W[68]. Thus the kernel becomes:

$$K(3,4,3',4') = \delta(3,4)\delta(3',4')v_c(3,3') - \delta(3,3')\delta(4,4')W(3,4) \tag{3.6}$$

Contrary to the mean field method cited before, here the interaction between particles is frequency dependent: this is introduced by the frequency dependence of the screening. However, in many others *ab-initio* implementations, W is replaced by its static approximation. An in-depth discussion of the impact of neglecting the dynamical effects can be found in [73][52, Chapter. 4.10].
Note that we cannot write K as single-particle function, because the presence of $\delta\Sigma(3,3')/\delta G(4,4')$ prevents any contraction of indices - in other words, we cannot reduce this expression to a single-particle one.

Bethe-Salpeter from an iterated Hedin equation
It's possible to arrive to (a slightly different) Bethe-Salpeter equation by starting from a different point and going beyond the GW approximation for Γ, approximating it at the first order in W.
Let's rewrite the Hedin equation for Γ (equation 2.41) in an iterative form[68], where the *n-th* order expression is denoted by superscript n:

$$\Gamma^{(n+1)}(1,2,3) = \delta(1,2)\delta(1,3) + \int d(4,5,6,7)\frac{\delta\Sigma^{(n)}(1,2)}{\delta G^{(n)}(4,5)}G^{(n+1)}(4,6)G^{(n+1)}(7,5)\Gamma^{(n+1)}(6,7,3) \tag{3.7}$$

If we now substitute the GW expressions for Σ (equation 3.5) in the right side of the equation and neglect the term $\delta W/\delta G$ coming from $\delta\Sigma^{GW}/\delta G$, we find[54]:

$$\Gamma^{(2)}(1,2,3) = \delta(1,2)\delta(1,3) + \int d(4,5,6,7) W^{(1)}(1,2) G^{(1)}(4,6) G^{(1)}(7,5) \Gamma^{(2)}(6,7,3) \tag{3.8}$$

If we multiply both sides of this equation by $-iGG$ and integrate we can write[1] a Bethe-Salpeter equation for the two-particle irreducible[2] polarizability ${}^4P$: ${}^4P = {}^4P_0 + \int {}^4P_0 W^{(1)}\, {}^4P$.

3.1 Effective two particle Hamiltonian

Different ways to solve the Bethe-Salpeter exist; in this section we sketch one of the most common approach, which is based on mapping the problem onto an effective two-particle hamiltonian.

The procedure is composed of two main step: first, we recast the Bethe-Salpeter equation as a matrix inversion problem (equation 3.13); then, we use the spectral representation of a non-hermitian matrix to map this problem onto a diagonalization problem. We start by defining the matrix element for the two-particle (four point) function:

$$L_{n_1 n_2}^{n_{1'} n_{2'}} \overset{\text{def}}{=} \int d\vec{r}_1 d\vec{r}_2 d\vec{r}_{1'} d\vec{r}_{2'} L(1,2,1',2') \psi_{n_1}(\vec{r}_1) \psi^*_{n_2}(\vec{r}_2) \psi^*_{n_{1'}}(\vec{r}_{1'}) \psi_{n_{2'}}(\vec{r}_{2'}) \tag{3.9}$$

where the n index contains the band and wavevector index. The Bethe-Salpeter equation 3.4 can be reinstated for the matrix elements:

$$L_{n_1 n_2}^{n_{1'} n_{2'}} = L^{0}{}_{n_1 n_2}^{n_{1'} n_{2'}} + L^{0}{}_{n_1 n_2}^{n_3 n_4}\, K_{n_3 n_4}^{n_5 n_6}\, L_{n_5 n_6}^{n_{1'} n_{2'}} \tag{3.10}$$

If we choose the single-particle basis that diagonalize G_0 also L_0 becomes diagonal:

$$L^{0}{}_{n_1 n_2}^{n_{1'} n_{2'}} = (f_{n_2} - f_{n_1}) \frac{\delta_{n_1, n_{1'}} \delta_{n_2, n_{2'}}}{E_{n_2} - E_{n_1} - \omega - i\eta} \tag{3.11}$$

Equation 3.10 can be formally solved in a similar way to the Dyson equation 2.32:

$$L_{n_1 n_2}^{n_{1'} n_{2'}} = \left[\frac{1}{1 - L^0 K} \right] L^0 \tag{3.12}$$

This equation can be rewritten[75] by defining the *two-particle excitonic Hamiltonian*:

$$L_{n_1 n_2}^{n_{1'} n_{2'}} = \left[H^{2p} - I\omega \right]^{-1}{}_{n_1 n_2}^{n_{1'} n_{2'}} \left(f_{n_{1'}} - f_{n_{2'}} \right) \tag{3.13}$$

$$H^{2p}{}_{n_1 n_2}^{n_{1'} n_{2'}} \overset{\text{def}}{=} (E_{n_2} - E_{n_1})\, \delta_{n_1, n_{1'}} \delta_{n_2, n_{2'}} + (f_{n_1} - f_{n_2})\, K_{n_1 n_2}^{n_{1'} n_{2'}} \tag{3.14}$$

$$v_{n_1 n_2}^{n_{1'} n_{2'}} = \int d\vec{r}_1 d\vec{r}_2 \psi^*_{n_1}(\vec{r}_1) \psi^*_{n_{2'}}(\vec{r}_1) v(\vec{r}_1, \vec{r}_2) \psi^*_{n_{1'}}(\vec{r}_2) \psi^*_{n_2}(\vec{r}_2) \tag{3.15}$$

$$W_{n_1 n_2}^{n_{1'} n_{2'}} = \int d\vec{r}_1 d\vec{r}_2 \psi^*_{n_1}(\vec{r}_1) \psi^*_{n_{2'}}(\vec{r}_1) W(\vec{r}_1, \vec{r}_2) \psi^*_{n_{1'}}(\vec{r}_2) \psi^*_{n_2}(\vec{r}_2) \tag{3.16}$$

---

[1] we omitted the details of the derivation, which can be find in *Onida et.al*(2002)[54], Section *IV.B*.

[2] The relation between the two-particle irreducible polarizability ${}^4P$ and the reducible one L, which we have defined at the beginning of the chapter, is[74] ${}^4P = L + \int L v^4\ P$.

Equation 3.13 can be solved by direct matrix inversion or with a different approach based on the spectral representation of the inverse matrix. If we define $A_\lambda^{n_1 n_2}$ and E_λ as the eigenvectors and eigenvalues of the excitonic hamiltonian H^{2p} (A is also called *excitonic wavefunction*):

$$H^{2p}{}^{n_{1'} n_{2'}}_{n_1 n_2} A_\lambda^{n_{1'} n_{2'}} = E_\lambda A_\lambda^{n_1 n_2} \tag{3.17}$$

then the spectral representation of H^{2p} is:

$$\left[H^{2p} - I\omega\right]^{-1}{}^{n_{1'} n_{2'}}_{n_1 n_2} = \sum_{\lambda,\lambda'} \frac{A_\lambda^{n_1 n_2} S^{-1}_{\lambda\lambda'} A_{\lambda'}^{n_{1'} n_{2'}}}{\omega - E_\lambda + i\eta} \tag{3.18}$$

where $S_{\lambda\lambda'}$ is the overlap matrix, defined as $S_{\lambda\lambda'} \overset{\text{def}}{=} \sum_{n_1 n_2} A_\lambda^{n_{1'} n_{2'}} A_{\lambda'}^{n_{1'} n_{2'}}$.
H^{2p} is non-hermitian, but the spectral representation is also valid for a generic non-Hermitian matrix. However this in turn implies that its eigenvectors are not orthogonal and $S_{\lambda\lambda'}$ differs from the identity.
We have therefore recast the Bethe-Salpeter equation 3.4 in a eigenvalue problem related to the effective excitonic hamiltonian. It's also convenient to derive an expression for the dielectric function:

$$\epsilon^{BSE}(\omega) = 1 - \lim_{\vec{q}\to 0} v(\vec{q}) \sum_\lambda \frac{\left| \sum_{v,c} \sum_{\vec{k}} \left\langle \psi_{v,\vec{k}} \middle| e^{-i\vec{q}\cdot\vec{r}} \middle| \psi_{c,\vec{k}+\vec{q}} \right\rangle A_\lambda^{(v\vec{k})(c\vec{k}+\vec{q})} \right|^2}{\omega - E_\lambda + i\eta} \tag{3.19}$$

where v and c are the band index of the valence bands (v) and conduction bands(c), $v(\vec{q}) = 4\pi e^2/q^2$ [3]. Let's compare this expression to the one in the *Independent Particle picture*, derived from the *RPA* (using the non interacting Green function G_0 [77, equation 2.33 and 2.72]):

$$\epsilon^{IPA}(\omega) = 1 - \lim_{\vec{q}\to 0} v(\vec{q}) \sum_{v,c} \sum_{\vec{k}} \frac{\left| \left\langle \psi_{v,\vec{k}} \middle| e^{-i\vec{q}\cdot\vec{r}} \middle| \psi_{c,\vec{k}+\vec{q}} \right\rangle \right|^2}{\omega - \left(E_{c\vec{k}} - E_{v\vec{k}+\vec{q}}\right) + i\eta} \tag{3.20}$$

The two equations reduce to:

$$\epsilon^{IPA}(\omega) = 1 - C \sum_{v,c} \sum_{\vec{k}} \frac{\left| \left\langle \psi_{v,\vec{k}} \middle| \hat{p} \middle| \psi_{c,\vec{k}} \right\rangle \right|^2}{\omega - \left(E_{c\vec{k}} - E_{v\vec{k}}\right) + i\eta} \tag{3.21}$$

$$\epsilon^{BSE}(\omega) = 1 - C \sum_\lambda \frac{\left| \sum_{v,c} \sum_{\vec{k}} \left\langle \psi_{v,\vec{k}} \middle| \hat{p} \middle| \psi_{c,\vec{k}} \right\rangle A_\lambda^{(v\vec{k})(c\vec{k})} \right|^2}{\omega - \left(E_{c\vec{k}} - E_{v\vec{k}}\right) + i\eta} \tag{3.22}$$

Where C is a constant and $\hat{p}$ is the usual momentum operator. We observe that the expression ($|\sum_{vc\vec{k}} \langle \psi_{v\vec{k}} | \hat{p} | \psi_{c\vec{k}} \rangle A_\lambda^{(v\vec{k})(c\vec{k})}|^2$) has the same role of the usual transition dipole moment squared inside ϵ^{IPA}, and thus represents a transition probability. It's usually called in literature as *BSE oscillator strength.* Finally we note that inside its

---

[3] A discussion about the $\vec{q} = 0$ component of $v(\vec{q})$ is found in *Sander et.al* [76, p. 7] and references therein.

expression A mix the (formerly) independent transitions.
Let's now discuss the structure of H^{2p} in the optical limit $\vec{q} \rightarrow 0$. The conservation of momentum implies that each independent transition must conserve the wavevector $\vec{k}$. H^{2p} can be written explicitly as:

$$H^{2p} = \begin{pmatrix} H^{resonant} & H^{coupling} \\ -\left[H^{coupling}\right]^* & -\left[H^{resonant}\right]^* \end{pmatrix} \tag{3.23}$$

The matrix $H^{resonant}$ is hermitian, involves only positive frequency transitions (hence its eigenvalues are real, which in turn implies that all excitons have infinite lifetimes), and has expression:

$$H^{resonant} = H^{2p}{}_{vc}^{v'c'} = (E_v - E_c)\,\delta_{vv'}\delta_{cc'} - \left[2v_{vv'}^{cc'} - W_{vc}^{v'c'}\right] \tag{3.24}$$

It has three different contributions:

1. The first term is the difference between the valence and conduction band energies involved in the independent particle transition.
2. The second term ($v_{vv'}^{cc'}$) includes the unscreened interaction and is called *electron-hole exchange*. It's positive and leads to an increase of the transition energy.
3. The third term ($W_{vc}^{v'c'}$) includes the screened interaction and is called *direct electron-hole interaction* (even if it stems from the variation fo the exchange-correlation potential). It's negative (attractive interaction) and thus reduces the transition energy.

The other element has expression:

$$H^{coupling} = H^{2p}{}_{vc}^{c'v'} = 2v_{vc'}^{cv'} - W_{vc}^{c'v'} \tag{3.25}$$

It's symmetric and mixes transitions of positive and negative energy. The neglect of this term constitutes the *Tamm-Dancoff* approximation, and makes H^{2p} hermitian and of half size.

From a qualitative point of view, the effect is twofold:

1. excitonic peak may appear within the fundamental bandgap.
2. The oscillator strength of the BSE spectrum appears redshifted (due to the term $W_{vc}^{v'c'}$ that usually overcomes $v_{vv'}^{cc'}$) with respect to the $GW - RPA$ one.

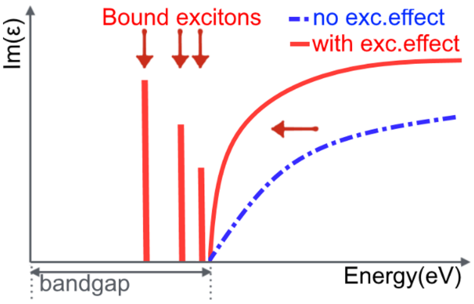

Figure 3.2: Qualitative representation of the excitonic effects on the $\mathrm{Im}(\epsilon)$.

Chapter 4

Transition Metals Perovskites

All perovskite-type materials owe their name to the very first perovskite, $CaTiO_3$. These materials share the same chemical formula ABX_3, where A and B are positively charged ions and X is a negatively charged ion.
In this work we study a representative set of a particular class of perovskites, the so-called *Transition Metals Oxide (TMO) perovskites*, which are characterized by having transition metals as cations and Oxygen as X. The properties of the metals' partially filled d orbitals give rise to a rich landscape of interesting physical properties, such as metal-insulator transitions[78], superconductivity[79], two-dimensional electron gas[80] and many others.
The different transition metals covered in the set distinguish themselves for the various ionic radii, which are linked to different lattice types and structural distortions, and for different types of d orbitals, which modulate the degree of electronic correlation and electron and spin itineracy.
In the first part of this chapter we will enumerate the different unit cells and lattice types, while in the second part we will discuss the electronic structures.

4.1 Structural properties

The first discovered perovskite, $CaTiO_3$, has a cubic unit cell, with the Ca atom at cube corner positions, Ti at body center positions and lastly the O atoms at face centered positions.
The Ti cation is in 6-fold coordination (surrounded by an *octahedron* of oxygens), while the larger Ca cation is in 12-fold cuboctahderal coordination, as shows in figure 4.1. The relative size requirements on the ions for the stability of the cubic structure are quite strict; distortions, needed to stabilize the cell, result in lower symmetry, such as orthorhombic, tetragonal or trigonal.
An empirical guess of the perovskite's structure (and its distortion) can be attained from the Goldschmidt tolerance factor t, which is based on the size mismatch between the cations radius and tries to determine the structure stability:

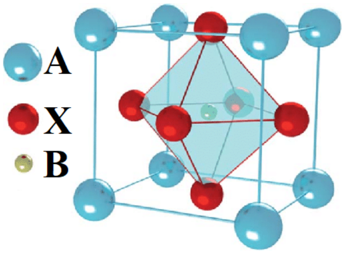

Figure 4.1: Example of cubic perovskite structure.

$$t = \frac{R_A + R_O}{\sqrt{2}(R_B + R_O)} \tag{4.1}$$

where t is the tolerance factor and R_A, R_B, R_O the ionic radii of the elements in ABO_3. If $0.9 < t \leq 1$ the perovskite has the ideal cubic structure, while $t > 1$ refers to an hexagonal or tetragonal structure and $0.7 < t \leq 0.9$ to an orthogonal or rhombohedral ones. Finally, if $t < 0.7$ then it might have a ferroelectric or a different structure.

However the Goldschmidt rule is not always effective for the TMO perovskites, since not all transition metals were investigated by Goldschmidt and some of the stoichiometries studied[81] were not matching with the previously found ones.

In addition to this, other sources of structural distortions exist. For example, $LaMnO_3$ exhibits a $GdFeO_3$-like distortion[82, 83], which leads to a decrease in the *d*-*d* hopping and bandwidth and gives the compound its orthorhombic structure. Moreover $LaMnO_3$ displays another type of distortion[84, 85], the so called *Jahn-Teller* effect (which removes the degeneracy of the $3d$ e_g orbitals).

The set of compounds considered in the present thesis and their fundamental characteristics are summarized in table 4.1.

Compound	**Crystal Structure**	***a***	***b***	***c***
$SrTiO_3$[86]	$C - P_{m3m}$	3.905	3.905	3.905
$SrZrO_3$[87]	$C - P_{m3m}$	4.109	4.109	4.109
$SrHfO_3$[88]	$C - P_{m3m}$	4.114	4.114	4.114
$KTaO_3$[89]	$C - P_{m3m}$	3.988	3.988	3.988
$LaScO_3$[90]	$O - P_{nma}$	5.680	5.680	5.680
$LaCrO_3$[91]	$O - P_{nma}$	5.480	7.759	5.517
$LaTiO_3$[92]	$O - P_{nma}$	5.589	7.901	5.643
$LaVO_3$[93]	$M - P_{21/b}$	5.592	7.752	5.562
$LaMnO_3$[82]	$O - P_{nma}$	5.742	7.668	5.532
$LaFeO_3$[94]	$O - P_{nma}$	5.568	7.850	5.557
$SrMnO_3$[95]	$C - P_{m\bar{3}m}$	5.374	5.374	7.600
$SrTcO_3$[96]	$O - P_{nma}$	5.535	7.845	5.588
$NaOsO_3$[97]	$O - P_{bca}$	5.384	7.580	0.703
Ca_2RuO_4[98]	$O - P_{bca}$	5.388	5.632	11.75

Table 4.1: The crystal structure (*C=cubic, T=tetragonal, O=orthorhombic, M=monoclinic*) and experimentally found lattice parameters (in $\dot{A}$) of the compounds. All values are taken from the cited papers.

4.2 Electronic properties

In this section we will recall some models aimed to describe the electronic structure of the coordination complexes, and then we will discuss the compounds' bandstructures.

Crystal fields and Molecular Orbitals

We start from *crystal field theory* (CFT), which describes the degeneracy breaking of d orbitals due to a static electric field produced by the surrounding ligands.

The d levels of an isolated transition metal are degenerate. However, in a perovskite

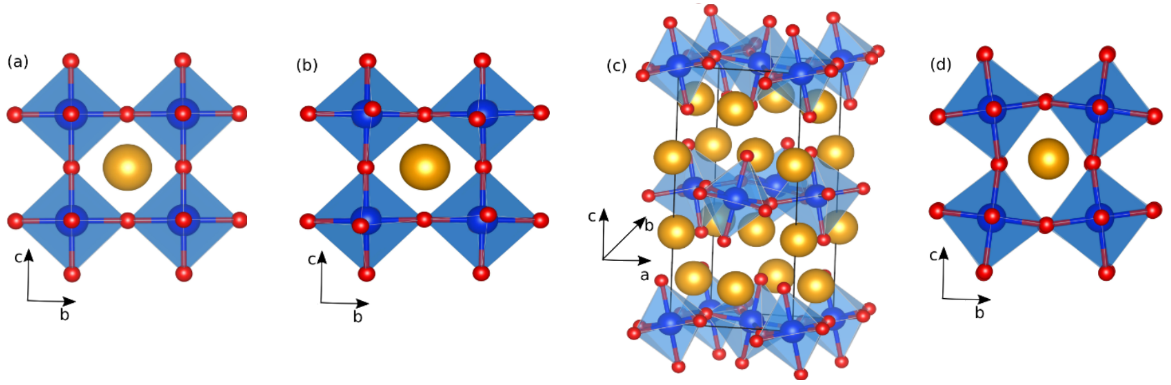

Figure 4.2: Different types of lattice distortions in the compounds studied in this thesis: (a)$P_{m\bar{3}m}$; (b)P_{nma} ; (c) P_{217b} ; (d) P_{cba}. Taken from [99].

structure (see figure 4.1) the positively charged metal ions are surrounded by six negatively charged ligands organized in an octahedral symmetry: this will cause a rearrangement of the d orbitals, where d_{x^2}, $d_{x^2-y^2}$ (together called e_g orbitals) will move at higher energies and d_{xy}, d_{xz}, d_{yz} will be shifted at lower energies and called t_{2g} orbitals, as shown in figure 4.3. The energy splitting between the two group is called *crystal field splitting*.

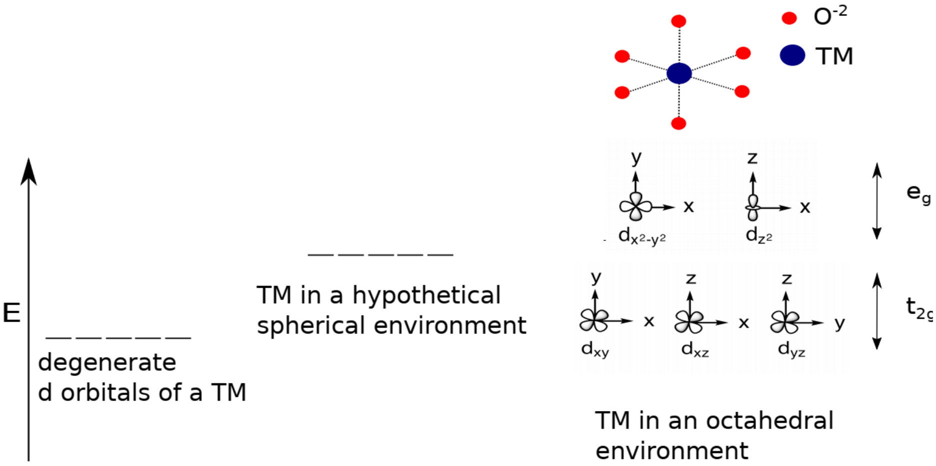

Figure 4.3: The crystal field splitting of a transition metal oxide surrounded by six negative oxygen ions in an octahedral arrangement. Taken from [100].

It's also important to consider another model, the *Molecular Orbital* (*MO*) theory, which considers the overlaps between orbitals. The $3d$ orbitals of the transition metals are more localized than $4p$ orbitals, and the $4p$ are more localized than $4s$; this means that the overlap with the ligands' orbitals is larger for $4s$ orbital than for $4p$, and so on. Consequently, the order of the energy splitting between the bonding and anti-bonding states is $4s > 4p > 3d$. Moreover, the σ^* bonds as well have larger overlaps than π^* bonds, which results in the e_g splitting being larger than the t_{2g} splitting.

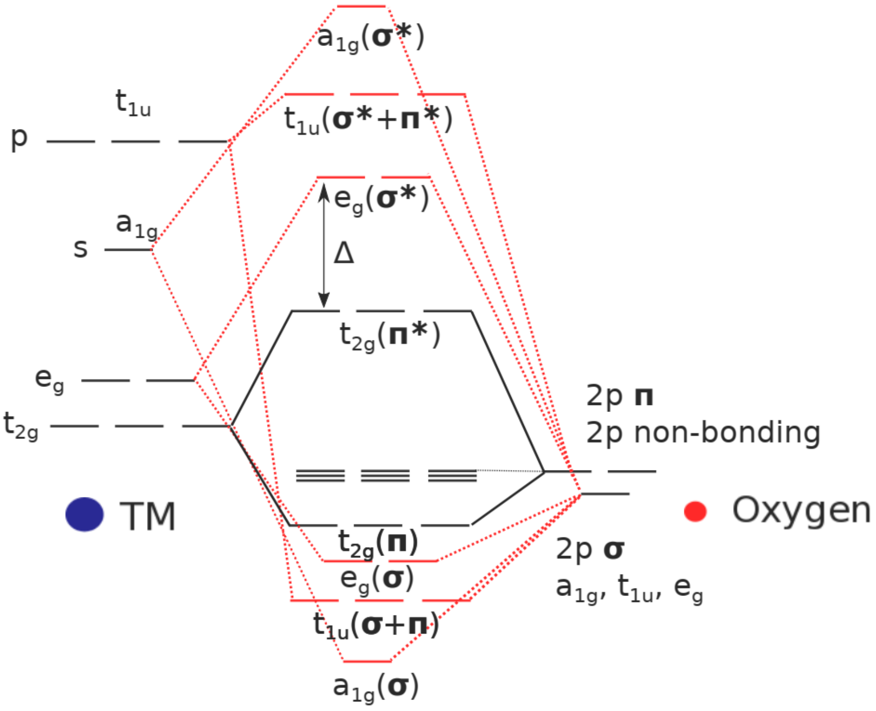

Figure 4.4: Molecular orbital diagram from a transition metal ion with its octahedral coordination complex. Taken from [100].

Bandstructures: Band, Mott and Charge-transfer insulators

While the *CFT* and *MO* theories can account for the electronic structure of coordination complexes, to understand the optical properties of the compounds it's necessary to describe accurately the perovskites' bandstructures.

However, the band theory based on the independent electron approximation cannot always correctly predict the materials' behavior, and this is especially true when transition metals are involved. Where unpaired *d* electrons are present, the system is in this approximation is often predicted to have a metallic behaviour, but many perovskites studied in this thesis (for example $LaTiO_3$) have unpaired electrons and are known to be insulators.

The insulating behaviour in those perovskites can only be explained by including the correlation effects neglected in band theory. The simplest model which can explain this behaviour is the *Hubbard* model.

Within this model, the electronic structure is governed by the competition between the local Coulomb interaction (U) and the bandwidth (W) of the d shell of the transition metals. Through this model Mott[101] studied the *metal-insulator transition* and observed how a strong short-range Coulomb interaction between electrons U can open a gap inside the d band, splitting it in two so-called *Hubbard subbands*.

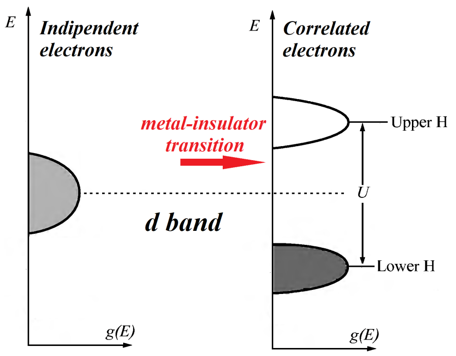

Figure 4.5: Schematic Example of metal-insulator transition.

The strength of U depends primarily on the spatial extent of the d orbitals and on the orbital filling. It reaches it largest values for $3d$ TMs[102, 103, 104], while $5d$ and $4d$ (which have less localized states) give rise to weaker electron-electron interaction and larger hopping. At the same time, localization of d orbital should increase with the atomic number along the same TM row of the periodic table.

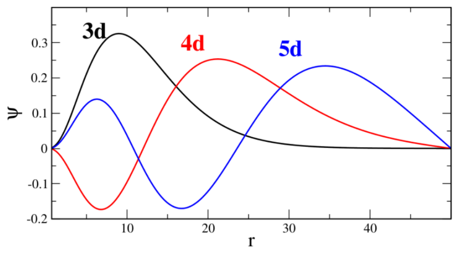

Figure 4.6: Example of TM d orbitals extensions. Taken from [99].

According to the classification scheme by *Zaanen, Sawatzky and Allen*[105], Mott insulators are classified into two types: the criterion is based on the relative values of the Hubbard gap U (equal to the energy splitting between the two Hubbard subbands) and the charge transfer energy Δ. If $\Delta > U$, the insulator is called *Mott-Hubbard (MH)*; if $U > \Delta$, it's called *Charge Transfer (CT)* type, as shown in figure 4.7.

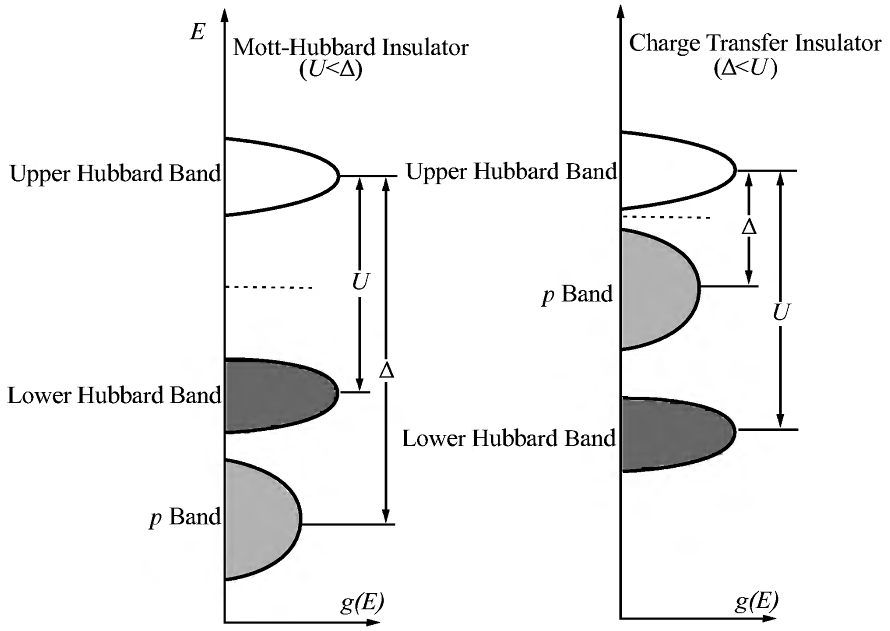

Figure 4.7: Classification of Mott insulators and relative position between the Hubbard subbands and the Oxygen $2p$ band. Taken from [106].

The perovskites studied in this thesis are all insulators, and some of them are magnetic insulators. The most favourable magnetic ordering among the studied compounds is the antiferromagnetic one, where two sublattices of transition metals ions with opposite spins occurs.

We now list in table 5.1 the different electronic characteristics of the various material and briefly discuss the compositions of the valence and conduction bands (following [99]):

Compound	**Electronic Configuration**	**Band Gap (eV)**		**Behaviour**	**Magnetic Ordering**
		Exp.	$G0W0$		
$SrTiO_3$	$3t_{2g}^0$	3.3	3.55	*band insulator*	*NM*
$SrZrO_3$	$4t_{2g}^0$	5.6	5.29	*band insulator*	*NM*
$SrHfO_3$	$5t_{2g}^0$	6.1	5.69	*band insulator*	*NM*
$KTaO_3$	$5t_{2g}^0$	3.6	3.56	*band insulator*	*NM*
$LaScO_3$	$3t_{2g}^0$	6.0	4.56	*band insulator*	*NM*
$LaTiO_3$	$3t_{2g}^1$	0.1	0.49	*Mott insulator*	*G-AFM*
$LaVO_3$	$3t_{2g}^2$	1.1	1.14	*Mott insulator*	*G-AFM*
$LaCrO_3$	$3t_{2g}^3$	3.3	2.95	*Mott insulator*	*G-AFM*
$LaMnO_3$	$3t_{2g}^3e_g^1$	1.1	0.97	*Mott insulator*	*A-AFM*
$LaFeO_3$	$3t_{2g}^3e_g^2$	2.1	1.91	*charge-transfer insulator*	*G-AFM*
$SrMnO_3$	$3t_{2g}^3$		1.75	*charge-transfer insulator*	*G-AFM*
$SrTcO_3$	$4t_{2g}^3$		1.14	*Magnetic insulator **	*G-AFM*
$NaOsO_3$	$5t_{2g}^3$	0.1	0.27	*Magnetic insulator **	*G-AFM*
Ca_2RuO_4	$4t_{2g}^3e_g^1$	0.3-0.5	0.50	*charge-transfer insulator*	*AFM*

Table 4.2: Electronic configuration, magnetic ordering, Experimental *vs* $G0W0@PBE$ bandgaps and behaviours for the studied set. The $G0W0$ calculations employed the parameters listed in table 5.1 and were taken from [99]. The asterisk on $SrTcO_3$ and $NaOsO_3$ symbolizes that, while having an insulator-like bandstructure, the two compounds are close to the metal-insulator transition[107, 108, 109].

The cubic non magnetic perovskites ($SrTiO_3$, $SrZrO_3$, $SrHfO_3$ and $KTaO_3$) and $LaScO_3$ display a band insulator behavior where the valence bands are dominated by $O-p$ states and the conduction bands by $TM-d$.

Mott insulators can be observed when the $3d$ band starts to be filled, exhibiting a predominant $d-d$ gap character with only minor $O-p$ states in the uppermost valence orbital (The $O-p$ percentages in the highest valence band are 10% for $LaTiO_3$, 26%

for $LaVO_3$, 22% for $LaCrO_3$ and 28% for $LaMnO_3$[1]) and lowest conduction ones (7% for $LaTiO_3$, 19% for $LaVO_3$ 18% for $LaCrO_3$ and 15% for $LaMnO_3$). The Jahn-Teller distortion plays also an important role in $LaMnO_3$[84, 85] (as already cited), lifting the orbital degeneracy in the e_g states.
The charge-transfer insulators have a very pronounced intermix of $O-p$ and $TM-d$ states for the highest valence band (the $O-p$ percentage are 40% for $LaFeO_3$, 40% for $SrMnO_3$ 16% for Ca_2RuO_4 and 42% for $NaOsO_3$), while the lowest conduction band is generally dominated by the $Tm-d$ states ($O-p$ percentage are 12% for $LaFeO_3$, 8% for $SrMnO_3$ 26% for Ca_2RuO_4 and 22% for $NaOsO_3$).
$NaOsO_3$ shows a peculiar nature[110, 111, 109]: with its $5d$ orbitals and their less localized nature (which results in weaker electron-electron interaction U and larger hopping W) $NaOsO_3$ behaves like an insulator on the verge of a Lifshitz insulator-to-metal transition and exhibits a spin orbit coupling (~ 0.3 eV).
Lastly, we focus on $SrTcO_3$: while some authors[112] have identified it as a Slater insulator (Slater's view on the metal-insulator transition are essentially based on the *exchange* interaction and deeply linked with the antiferromagnetic ordering[113]), it has been described with characteristics at the border between the itinerant-metallic and localized-insulating regimes [107, 108, 114].
The bandstructures and densities of states of all materials, calculated at $G0W0$ level (with a PBE starting point), are showed in the next page in figure 4.8.

---

[1] the percentages of all perovskites are taken from [99].

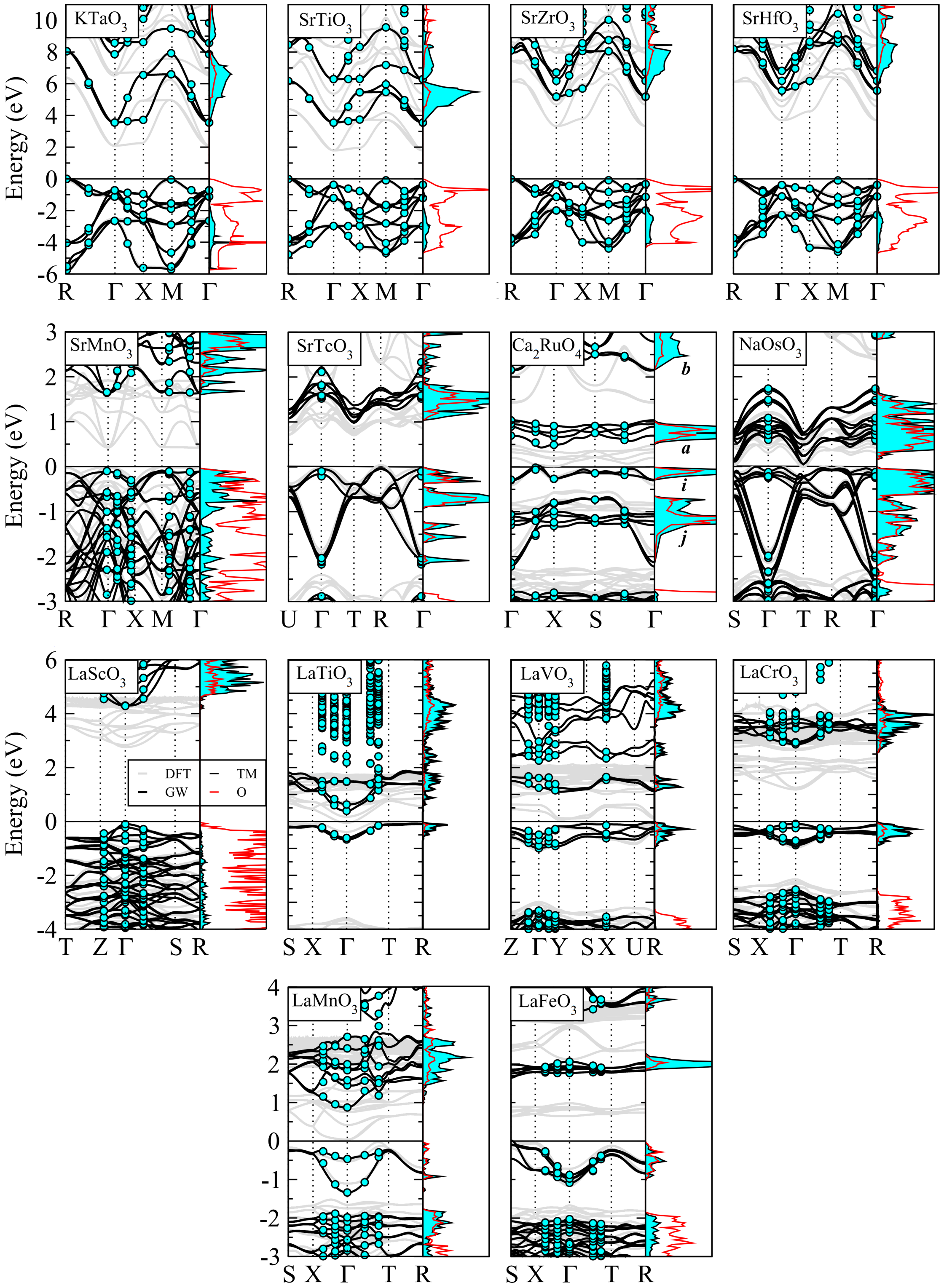

Figure 4.8: Calculated band structures from DFT (grey lines) and $G0W0$ (black) calculations together with $TM - d$(shadow, cyan line) and $O - p$(full line, red) the $G0W0$ density of states. The filled circles indicate the calculated $G0W0$ QP-energies (used for the Wannier interpolation). Taken from [99].

Part II

Methods and Results

In this section the optical properties of the perovskites set (computed using the methods described in the previous chapters) will be presented. The compounds set is divided in two classes, which are discussed separately: In chapter 6 we will discuss the results concerning the four cubic non magnetic (NM) perovskites $SrTMO_3$ *(*$TM = Sr, Hf, Zr$*) and* $KTaO_3$*, while in Chapter 7 we will address the remaining ten materials, which exhibit different types of structural distortions and magnetic orderings: The Lanthanide series* $LaTMO_3$ *(*$TM = Sc, Ti, Cr, Mn, Fe, V$*),* $SrTMO_3$ ($TM = Mn, Tc$)*,* $NaOsO_3$ *and* Ca_2RuO_4*.*

Initially, in chapter 5, we will outline step by step the general procedure employed for the optical spectra calculations.

The analysis of the optical properties of each material starts from the study of the convergence of the spectra with respect to the number of kpoints and to the numbers of valence and conduction bands employed in the BSE calculations. These two steps, short of being routine procedures, are computationally very expensive and became almost exceedingly so for the non cubic materials (due to the large size of the unit cells, which contain 20 atoms for $LaTMO_3$*,* $SrTMO_3$*,* $NaOsO_3$ *and 28 for* Ca_2RuO_4*), as we will discuss in chapters 6.1 and 7.1. We will therefore introduce in chapter 6.3 the techniques used to address these issues and their trade-offs.*

Then, in the chapters 6.4, 7.2 and 7.3, we will compare the results obtained through the $G0W0@PBE$ *and* BSE *methods, discussing the contribution of the electron-hole correlation for each perovskite and investigating the origin of the structures inside the various spectra. The remaining discrepancies with the experimental data will be finally examined.*

Chapter 5

Computational details

The calculations presented in this paper were conducted using the *Vienna Ab Initio Simulation Package* (*VASP*), Version 5.4.4[115].
The GW approximation was used in the $G0W0$ flavour[66], where the screening W_0 was fixed at the $DFT-RPA$ level. As a starting point for the $G0W0$ calculation we exploited a full DFT calculations using the generalized gradient approximation (GGA) parametrization introduced by Perdew, Burke, and Ernzerhof (PBE)[19]. When the GGA was not able to open the gap, a small on-site Hubbard U was added following the scheme of Dudarev[116] (this strategy was employed only for $LaTiO_3$ and $LaVO_3$; the starting point for them was a $DFT+U$ calculation with $U-J=2$ eV).

The same perovskites set analysed in the present thesis was subject of a thorough study (at $G0W0$ level) by *Ergönenc.et.al*[99]. In this work the authors outlined a proper procedure to obtain well-converged[1] quasiparticle(QP) energies and accurate bandgaps within the $G0W0$ method:

1. While keeping the kpoint mesh fixed, the bandgap E_g is computed as a function of the number of bands (*NBANDS*) for different values of the cut-off energy($ENCUT$).
2. Then, by fixing *NBANDS* and $ENCUT$ to their optimum values, E_g is converged with respect to the number of k-points.

Unless otherwise noted, the $ENCUT$, *NBANDS* and kpoint densities used for the consecutive DFT and $G0W0$ calculations were taken from this paper and obtained through the procedure described; the actual parameters are listed in table 5.1. Conversely, the $ENCUTGW$[2] was kept at the standard value $= 2/3ENCUT$.
All calculation employed Ultrasoft *GW PAW*, except $SrTiO_3$ ones, which adopted Norm-Conserving ones: the reason behind this PAW choice for $SrTiO_3$ were discussed in [99]. A number of frequency points in the $G0W0$ calculation ($NOMEGA$ variable) of 64 was deemed sufficient for all materials (with the exception of $SrHfO_3$, which employed 96).
For the cubic non magnetic perovskites and $LaScO_3$ we performed non-spin polarized

---

[1] A band gap is said *converged* when differences between bandgap values obtained with different (consecutive) parameter values are lower than a given threshold. The parameters in Table 5.1 satisfy a threshold of 100 meV.

[2] *ENCUTGW* represents the cutoff energy for the response function P as described in `https://cms.mpi.univie.ac.at/wiki/index.php/ENCUTGW` (url checked on October 3, 2019).

Compound	***ENCUT***	***NBANDS***	***kpoints mesh***
$SrTiO_3$	600	512	$4 \times 4 \times 4$
$SrZrO_3$	650	1792	$4 \times 4 \times 4$
$SrHfO_3$	650	2304	$4 \times 4 \times 4$
$KTaO_3$	500	896	$4 \times 4 \times 4$
$LaScO_3$	500	1280	$5 \times 5 \times 3$
$LaTiO_3$	500	448	$5 \times 3 \times 5$
$LaVO_3$	500	448	$5 \times 3 \times 5$
$LaCrO_3$	500	448	$5 \times 3 \times 5$
$LaMnO_3$	500	448	$5 \times 3 \times 5$
$LaFeO_3$	500	448	$5 \times 3 \times 5$
$SrMnO_3$	500	448	$4 \times 4 \times 2$
$SrTcO_3$	500	512	$5 \times 3 \times 5$
$NaOsO_3$	500	448	$5 \times 3 \times 5$
Ca_2RuO_4	500	521	$4 \times 4 \times 2$

Table 5.1: Set of parameters, taken from [99]. This setup guarantees well-converged QP energies within a accuracy of around 100 meV.

calculations; all the others compounds required spin polarized ones. Finally, for for $NaOsO_3$ we took into account the spin-orbit coupling (and thus used non collinear calculations).

Finally, all BSE calculations were performed within the *Tamm-Dancoff* approximation[76]. The experimental data were taken from [117] ($SrHfO_3$), [118] ($SrTiO_3$), [119] ($SrZrO_3$ and $KTaO_3$), [120] (La series)(except $LaMnO_3$ from [121]),[109] ($NaOsO_3$), [122] (Ca_2RuO_4). For $SrMnO_3$ and $SrTcO_3$ no experimental reports in the literature have been found.

Chapter 6

Cubic non magnetic perovskites

6.1 Kpoints convergence

The BSE step, performed on top of the $G0W0$ calculation, requires two additional parameters: the number of conduction bands ($NBANDSO$) and of valence bands ($NBANDSV$) included in the excitonic hamiltonian and effective eigenvalue equation (see equation 3.17 and section 3.1). Therefore, to obtain meaningful results, we must study the spectra convergence with respect to these two parameters.
However, this is not the end of the story: often the kpoints meshes which provide well converged total energies or bandgaps are inadequate to attain converged exciton binding energies and fails to deliver converged spectra. For example, as can be seen from figure 6.1, for $SrZrO_3$ the $4 \times 4 \times 4$ mesh (which proves enough for the bandgap calculation[99]) provides a poor spectra, and even a $10 \times 10 \times 10$ mesh fails to reach convergence.

Thus a question arises: *how can we choose these parameters?* The general outline of the procedure employed recalls the one sketched in Section 5. To determine the convergence of the dielectric function with respect to the number of kpoints, we compare the dielectric function curves for different kpoint meshes: convergence is achieved when the curve itself does not exhibit significant changes with further increase of the mesh density. Therefore, such study requires to repeat the entire chain of calculation ($DFT \rightarrow G0W0 \rightarrow BSE$, see figure 6.2) for each mesh.
Once we have picked a mesh, we have to determine $NBANDSV$ and $NBANDSO$ in a similar way, while keeping the mesh and all the other parameters fixed (The convergence of the bands number will be discussed in the next section).

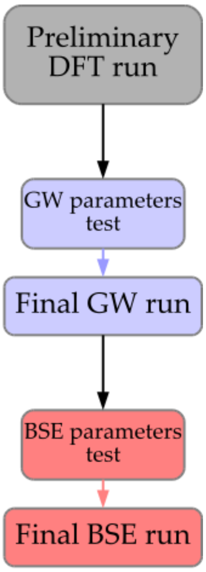

Figure 6.2: Workflow of each BSE calculation.

However the application of this procedure exhibits some complication: It's well known in literature[52, p. 370][123, 76, 124] that the optical spectra determination requires a much denser sampling of the Brillouin Zone than the corresponding ground-state properties calculation. The first reason behind the slow convergence of the dielectric function with respect to the kpoint mesh is that the BSE oscillator

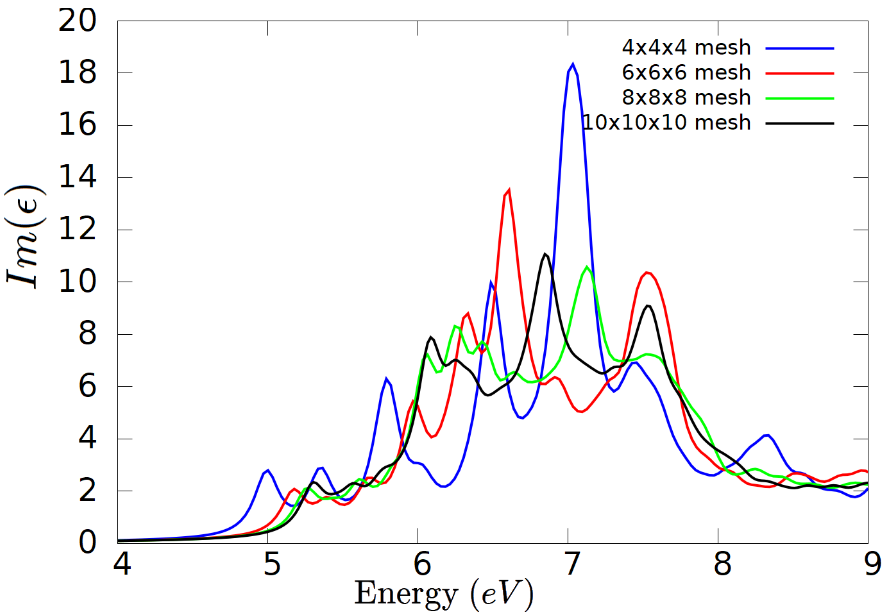

Figure 6.1: BSE calculation of the imaginary part of $SrZrO_3$ using different kpoints meshes. All calculations employed the cutoff energy and number of bands for the $DFT@PBE$ and $G0W0$ runs listed in table 5.1 and $NBANDSO = NBANDSV = 10$ for the BSE runs.
The $G0W0@PBE + BSE$ on $6 \times 6 \times 6$ run required $\sim$ 5 hours, the one on $8 \times 8 \times 8$ required $\sim$ 23 hour and the one on $10 \times 10 \times 10$ required $\sim$ 72 hours (all on 64 cores).

.

strengths (see the numerator in equation 3.19, i.e. $|\sum_{vc\vec{k}} \langle \psi_{v\vec{k}}|\hat{p}|\psi_{c\vec{k}}\rangle A_\lambda^{(v\vec{k})(c\vec{k})}|^2$) mix transitions at precise kpoints in space, and both $A_\lambda^{(v\vec{k})(c\vec{k})}$ and $\langle \psi_{v\vec{k}}|\hat{p}|\psi_{c\vec{k}}\rangle$ might depend in critical way on the $\vec{k}$ values inside the Brillouin Zone. Most ground state properties don't depends on values at individual kpoints (and thus on the details of the electronic structure), but only on integrals that span the entire Brillouin Zone[52, p. 370].
Another cause is associated to the localization of the exciton wavefunction $A_\lambda^{(v\vec{k})(c\vec{k})}$ inside the Brillouin Zone: while *Frenkel*-like excitons mix transitions from a rather large portion of the Brillouin Zone and, as such, allow a more coarse sampling[74], *Wannier-Mott*-like excitons are usually very localized in the Fourier space and require denser mesh to be described properly.

This in turn, make both the final calculation and the convergence study exceedingly time consuming and computationally expensive. The reason behind this is twofold:

1. The $G0W0$ step scales unfavorably with the kpoints number, roughly in a quadratic manner in the current $VASP$ implementation[123]. As introduced before, the optical properties simulation requires very dense kpoint meshes, and this is a mayor hindrance in this type of calculations. Luckily, $VASP$ handles efficiently the symmetry of the unit cell, restricting the calculation only to the kpoints inside the Irreducible Brillouin Zone: this somewhat helps speeding the calculations particularly for compounds with highly symmetric cells (such as the cubic perovskites of this section).

2. Also the last step, the BSE one, poses a difficulty: the memory requirement of

BSE implementation in $VASP$ scales quadratically with respect to the number of kpoints while the time requirement scales with the third power[1].

How we can proceed?
To mitigate these issues we slightly modify the approach summarized previously replacing the BSE step in the kpoint convergence study with the so-called *modelBSE*[125, 126]. Its purpose is to approximate a full BSE calculation by skipping the intermediate $G0W0$ run, simulating the $G0W0$ correction to the bandstructure and replacing the dielectric function $\epsilon^{-1}_{\vec{G},\vec{G}'}(\vec{k})$ (determined in the $G0W0$ step at a RPA level) with a local model function:

$$\epsilon^{-1}(\vec{k}+\vec{G}) = 1 - (1-\epsilon^{-1}_{-\infty})\exp\left[-\frac{|\vec{k}+\vec{G}|^2}{4\lambda^2}\right] \tag{6.1}$$

This allows to replace the RPA screening W (employed in the $G0W0$ run) with an analytical model:

$$W^{cv\vec{k}}_{c'v'\vec{k}} = \frac{4\pi e^2}{\Omega}\sum_{\vec{G}} B^{c\vec{k}}_{c'\vec{k}}(\vec{G})\frac{\epsilon^{-1}(\vec{k}+\vec{G})}{|\vec{k}+\vec{G}|^2}B^{v\vec{k}}_{v'\vec{k}}(\vec{G}) \tag{6.2}$$

Where $B^{n\vec{k}}_{n'\vec{k}}(\vec{G}) = \frac{1}{\Omega}\int_\Omega d\vec{r}u_{n\vec{k}}(\vec{r})u^*_{n'\vec{k}}(\vec{r})e^{i(\vec{k}+\vec{G})\cdot\vec{r}}$, ϵ_∞ is the static ion-clamped dielectric function in the long-wave limit, and λ is a screening length parameter to be determined by fitting ϵ^{-1} to the screened Coulomb kernel diagonal values obtained through a previous $G0W0@PBE$ run (for the 4 cubic perovskites we fitted λ on a $G0W0$ run performed on a $8\times8\times8$ mesh).
To approximate the $G0W0$ correction to the bandstructure we *rigidly shift* the DFT (PBE) conduction bands: the value of this shift, sometimes called in literature *Scissor operator*[127, 128], is again determined by fitting the bandgap to a previous $G0W0$ run. The values of the fitted quantities are collected in table 6.1, while the graphs of the fitted curve are displayed in figure 6.3.

	$SrZrO_3$	$SrTiO_3$	$SrHfO_3$	$KTaO_3$
Scissor Op.(eV)	0.944	1.645	1.913	1.395
λ	1.356	1.463	1.448	1.432
ϵ^{-1}_∞	0.105	0.165	0.242	0.194

Table 6.1: value of the fitted parameter required for the $mBSE$ runs. The fit was performed on a $G0W0@PBE$ using a $8\times8\times8$ mesh and the cut-off energies and numbers of bands listed in table 5.1.

---

[1] as detailed in the online manual `https://cms.mpi.univie.ac.at/wiki/index.php/NBANDSV` (url checked on October 3, 2019). The requirements are: time $\sim (NBANDSO * NBANDSV * N_{kpoints})^3$, while memory $\sim (NBANDSO * NBANDSV * N_{kpoints})^2$. Furthermore we note that the BSE implementation in $VASP$ 5.4 does not exploit symmetry, while the $G0W0$ one does.

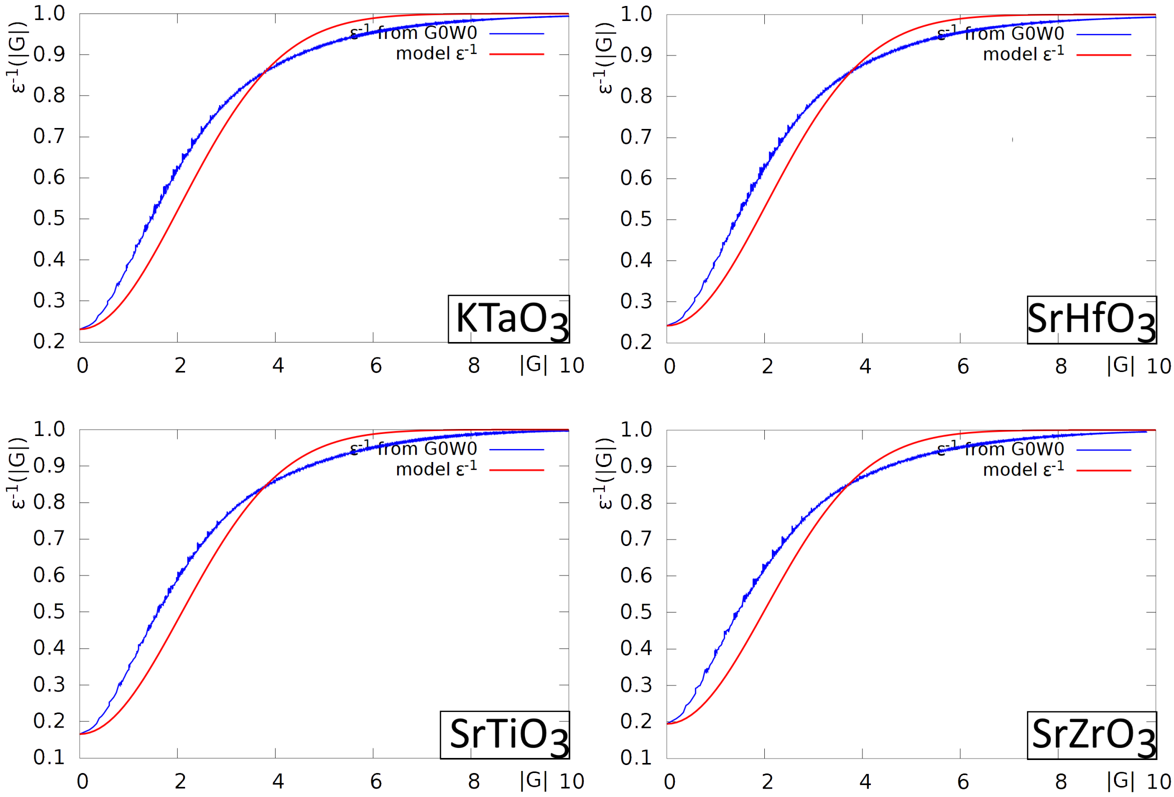

Figure 6.3: fitted model dielectric function and screened Coulomb kernel diagonal values obtained through a $G0W0@PBE$ run. The $G0W0@PBE$ runs were performed with a $8 \times 8 \times 8$ mesh and the cut-off energies and numbers of bands listed in table 5.1.

For the convergence study with the $mBSE$ method we included only four conduction and valence bands, with the purpose of reducing the computational cost. Even so the calculations with the $18 \times 18 \times 18$ mesh required between $8.6 GByte/core$ ($KTaO_3$) and $12.8 GByte/core$ ($SrZrO_3$) using 256 total cores[2].
Two general trends are recognizable in figure 6.4:

1. The kpoint density increase is associated to a strong reduction of the height (intensities) differences between the peaks and the adjacent valleys' minimums: spectral weight is shifted away from the peaks and make the overall shape more uniform. This effect is indeed visible in the BSE calculations (see figure 6.5, 6.8, 6.11, 6.14). The fact that a coarse kpoint sampling introduces additional features is well known in literature[77, chapter. 6.2.2]. The reason behind the slower convergence of the dielectric function has been previously discussed; nonetheless, at $18 \times 18 \times 18$ the peaks' intensities are well converged.

2. The peaks transition energies (*i.e. the positions*) are in general not fully converged, even if the outcomes are markedly material-dependent. While $SrHfO_3$ line shape is almost converged, the peaks transition energies of other material (especially $KTaO_3$) have not yet reached such outcome. From a qualitative perspective, each spectra's features remain coherent and similar between the different meshes (at least starting from $12 \times 12 \times 12$) and well discernible. The structure's onset however is very well converged for all materials.

---

[2] $VASP$ redistributes the BSE matrix among all cores: thus increasing the total number of cores reduces the memory allocated on a single core.

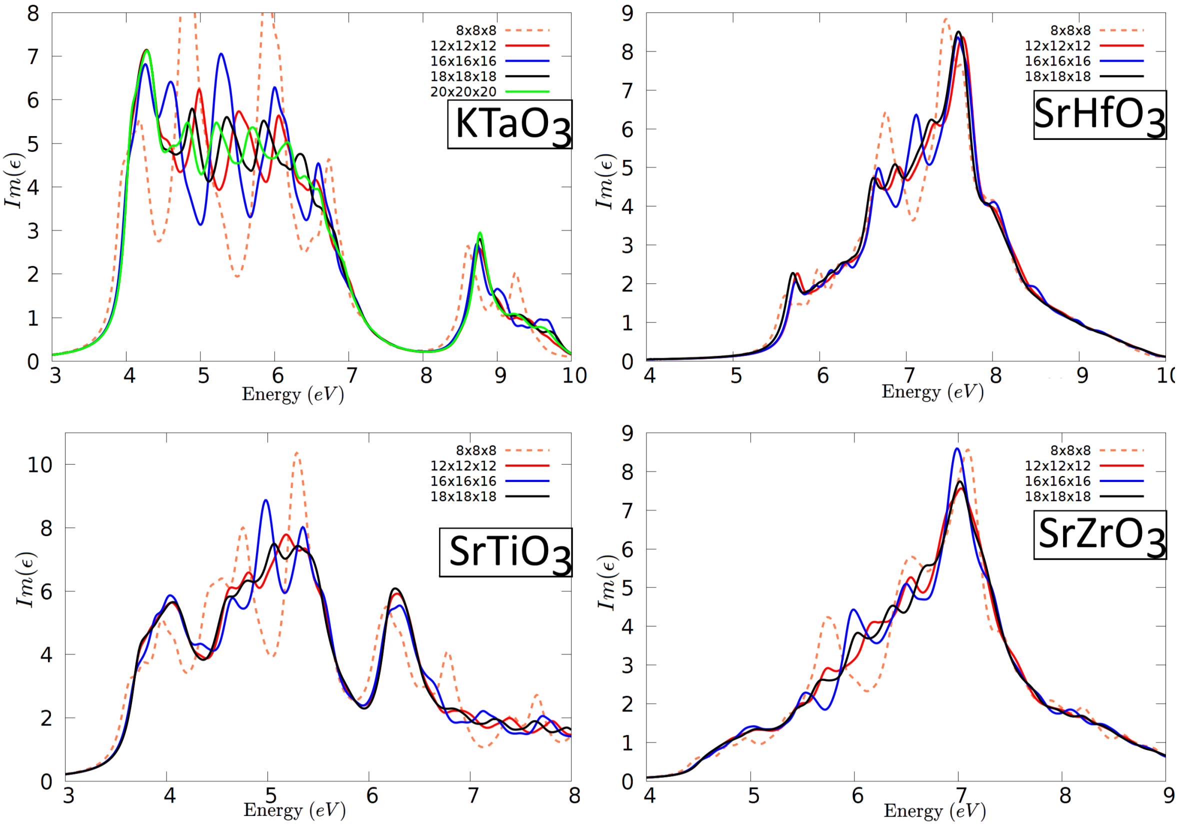

Figure 6.4: dielectric function of the four cubic non magnetic perovskites for different kpoint mesh obtained with the $mBSE$ method with $NBANDSV = NBANDSO = 4$ kept fixed. The cut off energies are listed in table 5.1.

6.2 NBANDSV and NBANDSO convergences

As mentioned in chapter 6.1, a full BSE calculation requires two additional parameters, that is the numbers of conduction and valence bands included in the calculation. The optimal procedure would dictate to run, using the (well enough) converged kpoint mesh, many full BSE or $mBSE$ simulations with varying $NBANDSV$ and $NBANDSO$ until convergence is reached. However, as explained before, the memory requirement of BSE implementation in $VASP$ scales quadratically with respect to the number of kpoints while the time requirement scales with the third power. Because of this, a $NBANDSV/NBANDSO$ convergence study on the denser $(18 \times 18 \times 18)$ kpoint mesh would have been computationally very costly. Therefore we ran the $NBANDSV/NBANDSO$ convergence study on an $8 \times 8 \times 8$ mesh.
Moreover, for this study we opted to discard the $mBSE$ approach (adopted in the kpoints convergence) and employ the full BSE approach. The reason behind this choice is that, short of being a purely technical step, this convergence study can also give information about the origin of the peaks and structures in the full spectra[128]. The converged values are shown in table 6.2.

	$SrTiO_3$	$KTaO_3$	$SrHfO_3$	$SrZrO_3$
NBANDSO	12	12	12	12
NBANDSV	10	12	13	12

Table 6.2: Converged value for $NBANDSV$ and $NBANDSO$ for the cubic non magnetic perovskites considered, determined on a $8 \times 8 \times 8$ mesh.

6.3 Methods adopted

As outlined above, the considerable computational cost could make running BSE calculations for large system a daunting task. Different paths were adopted to face this challenge.

A way to reduce the computational cost is to avoid the direct diagonalization of the effective eigenvalue equation and rely on iterative solvers[129, 130]. These methods can achieve time requirements scaling as $\mathcal{O}(N^2)$ (instead of $\mathcal{O}(N^3)$) and reduced memory occupation. However they don't yield excitons eigenvalues and eigenfunctions, which are usually very helpful to interpret the results.

Another possibility is to adopt a "*hybrid*" kpoints mesh[124, 131], that is a grid that is denser in the region of the Brillouin Zone that is most relevant for the exciton and coarser in the other regions. This technique however can be applied only with *Wannier-Mott*-like exciton; moreover, due to technical reasons related to the kpoints sampling in the VASP implementation of the *GW* method, it is presently not possible to calculate the QP energies for non-uniform k-point meshes.

We employ a different approach, based on the averaging of shifted-grid independent calculations[76, 132]:

1. Generate all irreducible kpoints $\vec{k}^n_{p=1,..,\mathcal{L}}$ with weights $w_{p=1,..,L}$ from a Γ-centered $n \times n \times n$ mesh.
2. Generate $\mathcal{L}$ $m \times m \times m$ kpoints meshes shifted off Γ by the previously calculated shifts $\vec{k}^n_{p=1,..,\mathcal{L}}$: we denote as $\mathcal{M}_p$ the mesh with shift $\vec{k}^n_p$.
   The set formed by the union of all shifted meshes $\bigcup \mathcal{M}_p$ includes all kpoints of a regular (Γ centered) $(m \cdot n) \times (m \cdot n) \times (m \cdot n)$ mesh, with the proper weights.
3. Perform an independent calculation for each mesh $\mathcal{M}_p$, and average the dielectric functions over the $\mathcal{L}$ calculations: $\epsilon = \frac{1}{W} \sum_{p=1}^{\mathcal{L}} w_p \epsilon_p$ where $W = \sum_{p=1}^{\mathcal{L}} w_p$ and ϵ_p denotes the dielectric function calculated on the mesh $\mathcal{M}_p$.

Using this scheme, the computational time required reduces roughly by a factor $(n^3)^2$ in the GW calculations and $(n^3)^3$ in the Bethe-Salpeter ones[76].

The trade-off is that the interaction range of the exciton is limited by the $m \times m \times m$ mesh used in each GW and BSE calculation; in other words, we truncate the long-range part of the Coulomb kernel at roughly m times the unit cell size. This means that this approximation is viable only if the compound exhibits localized (in real space) excitons, and must be applied with care in presence of *Wannier-Mott*-like excitons (due to their large real-space radius).

In the next paragraphs we'll compare the spectra obtained with this methods the ones obtained with the standard method, and analyze the results.

6.4 Optical Properties

KTaO$_3$

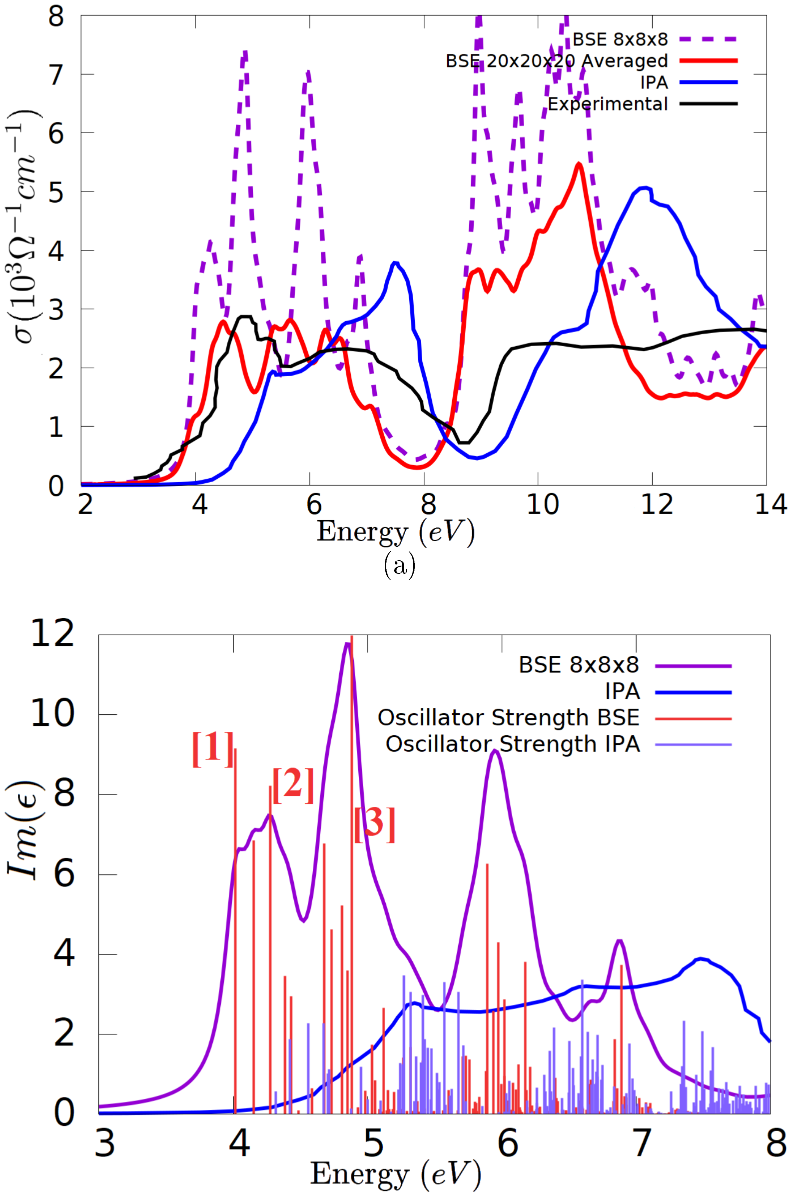

(a)

(b)

Figure 6.5: (a): Spatially averaged optical conductivity of $KTaO_3$, obtained with different approaches: in red through an averaged BSE on a $20 \times 20 \times 20$ mesh ($n \times n \times n = 4 \times 4 \times 4, m \times m \times m = 5 \times 5 \times 5$), in violet through an BSE on a $8 \times 8 \times 8$ mesh, in blue through a IPA on $G0W0$ QP-energies and $8 \times 8 \times 8$ mesh, while the black one is the experimental curve. (b): Zoom of the first structure of $\Im[\epsilon]$ with the associated oscillator strength.

We can identify two structures inside the spectra showed in figure 6.5: a series of peaks plus a shoulder in the range $\sim [3, 8]$ eV and a less prominent structure for energies above 9 eV.
The two BSE curves exhibit a overall good agreement with the experimental data for what concerns the transition energies of the first structure: The onset's transition energies (at 4 eV) are only slightly underestimated (by about $0.3 - 0.4$ eV), while the shoulder at 7 eV exhibits a more severe underestimation.

We recall from figure 6.4 that denser meshes, while resulting in a shift of the peaks, don't modify the onset position (which only requires a $12 \times 12 \times 12$ mesh to be well converged). Thus, the onset position error cannot be traced back to the not fully attained kpoint convergence. Furthermore, the curve associated with the $20 \times 20 \times 20$ mesh offers satisfying peak intensities for what concerns the first structure , as opposed to the $8 \times 8 \times 8$ mesh.
The second structure is instead underestimated by almost 1 eV by the BSE curves, and this effect cannot again be traced back to the kpoints convergence (the transition energies between the two BSE curves are similar despite the different meshes adopted). We will show in section 6.5 that this issue is related to the choice of the DFT starting point.
The IPA picture severely overestimates the first structure' position, while the second structure's onset results less overestimated.
The excitonic effects are prominent, as we can see from the marked redshift in the oscillator strength in figure 6.5.
To understand the origin of the peak structures we followed the method employed by $Sponza.et.Al$[128], based on the convergence of the spectra with respect to the number of conduction bands while keeping fixed the number of valence bands (at 12).

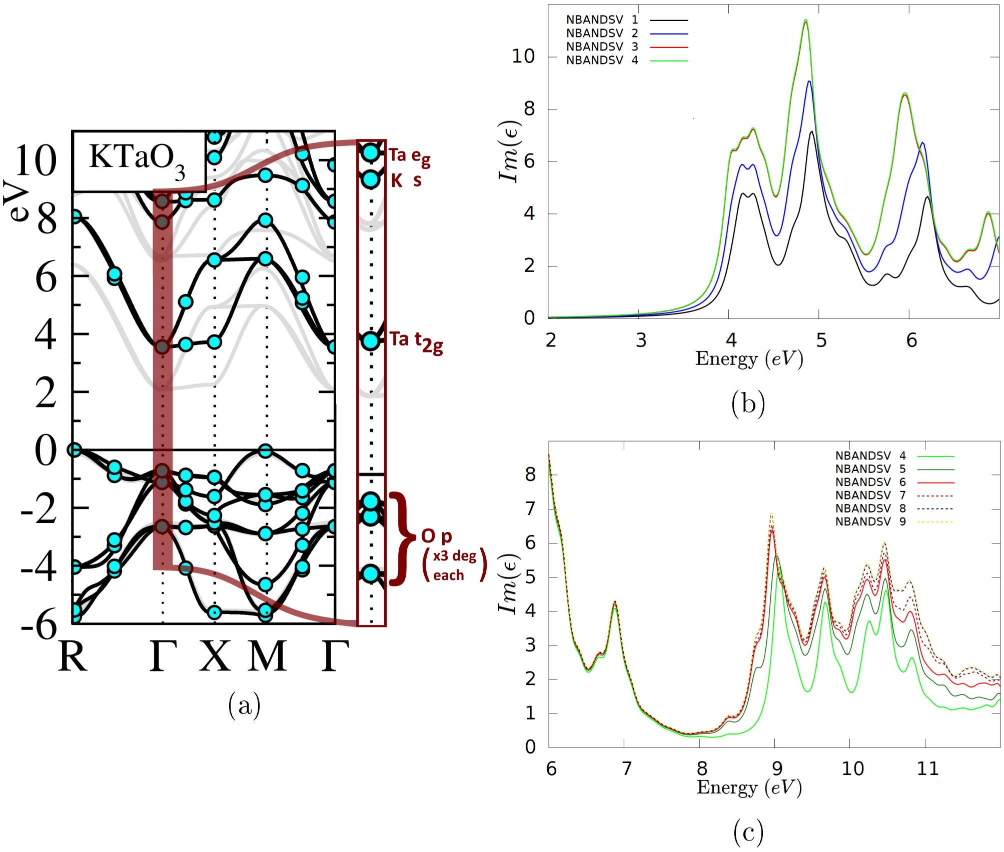

(a)
(b)
(c)

Figure 6.6: (a): bandstructure (taken from [99]), with a focus on the QP-energies at the Γ point and the projected wavefunction character of each band.
(b),(c): Convergence with respect of the number of conduction band (with $NBANDSO$, number of valence bands fixed). The spectra were obtained through a full BSE calculations on a $8 \times 8 \times 8$ mesh.

The first structure (range [3, 7] eV) is completely converged by including the first three conductions bands ($NBANDSV = 3$), and is completely determined by the $O\ p \rightarrow Ta\ t_{2g}$ transitions.
These $O\ p \rightarrow Ta\ t_{2g}$ transitions give also a substantial contribution to the second structure (range [8, 11] eV); the description of the second feature's onset (range [8, 10] eV) is attained with $NBANDSV = 6$, which encompasses the $O\ p \rightarrow Ta\ e_g$, $O\ p \rightarrow K\ s$ transitions. Finally, the shoulder's description requires $NBANDSV = 8$, which involves the transitions between the $O\ p$ near the Fermi level and the $Sr\ 3e_g$ states (which lie at 9.9 eV at Γ).

We can validate the peaks attribution and further elaborate it by looking at the plot of $|A^{\lambda}_{c,v,\vec{k}}|$ along given high symmetry directions in reciprocal space (figure 6.7). This allow us to point out the kpoints mixed for a given transition and to study the valence bands involved in each transition.
The first transition is strongly localized at Γ (with a minor contribution along the $\Gamma - X$ direction) and involves only the highest occupied and lowest unoccupied levels. This transition is associated to the first eigenvalue with non-zero oscillator strength: hence it is related to the optical gap.
The exciton wavefunctions of the second and third transition described in figure 6.7 are less localized on Γ and more distributed along the $\Gamma - X$ direction. The major contributions from the valence bands came not from the three highest occupied but from valence bands $4 - 6$; conversely, the only conduction bands with relevant contributions are the lowest (triply degenerate) ones, in agreement with the description in figure 6.6b.

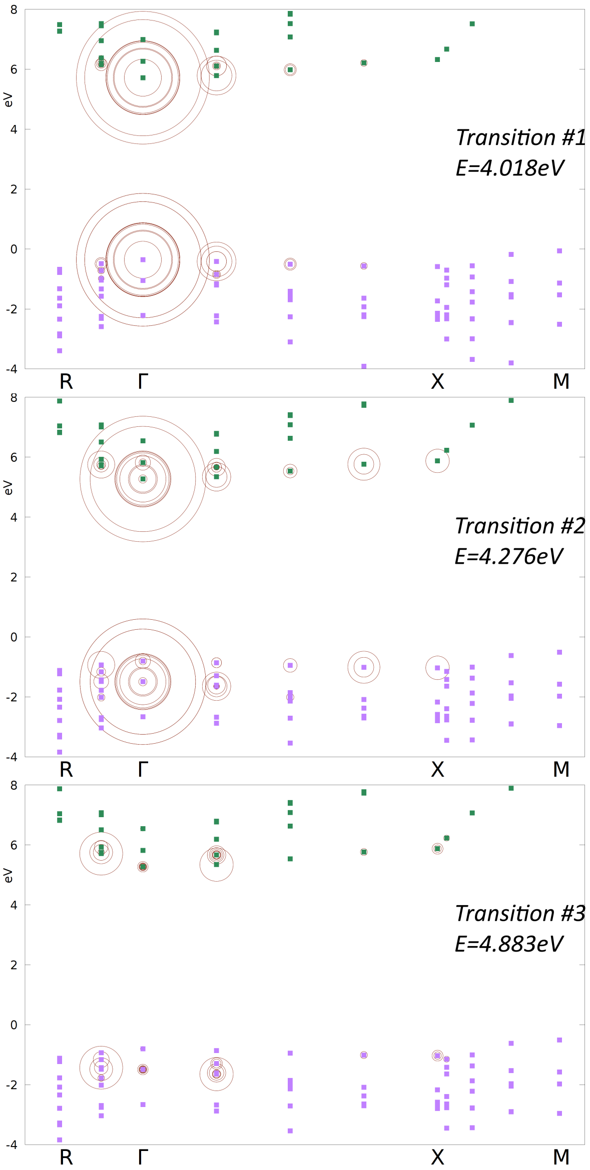

Figure 6.7: Plot of absolute value of the exciton wave function along high symmetry lines in reciprocal space. The circle radius is proportional to $|A^{\lambda}_{c,v,\vec{k}}|$. The transition's numbers refers to the label in figure 6.5b.

$SrTiO_3$

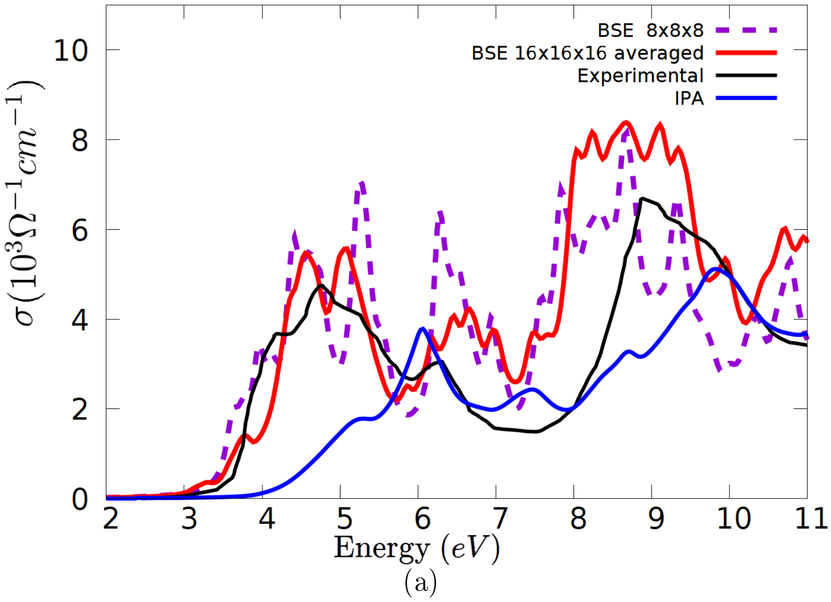

(a)

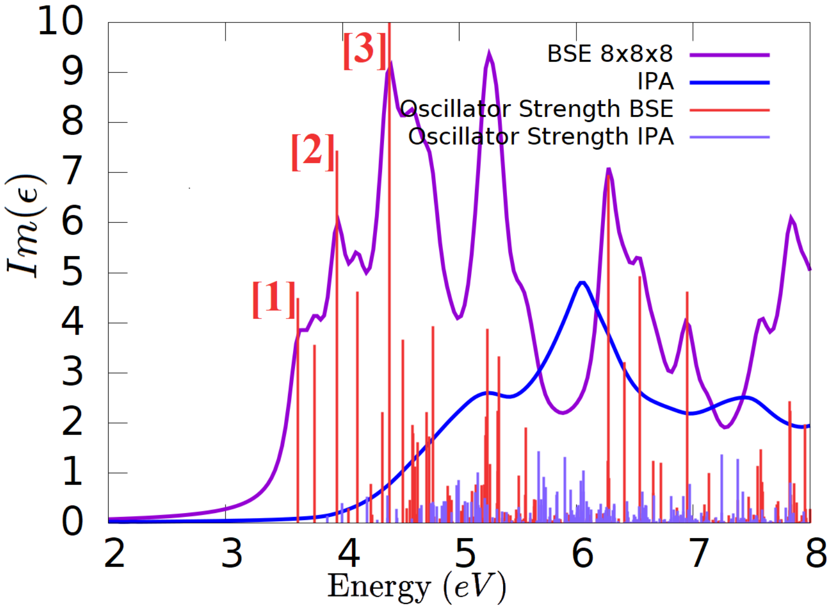

(b)

Figure 6.8: (a): Spatially averaged optical conductivity $(10^3\Omega^{-1}cm^{-1})$ of $SrTiO_3$, obtained with different approaces: in red through an averaged BSE on a $16 \times 16 \times 16$ mesh $(n \times n \times n = 4 \times 4 \times 4, m \times m \times m = 4 \times 4 \times 4)$, in violet through an BSE on a $8 \times 8 \times 8$ mesh, in blue through a IPA on $G0W0$ QP-energies and $8 \times 8 \times 8$ mesh, while the black one is the experimental curve. (b): Zoom of the first structure (range $[2, 8]$ eV) of $\Im[\epsilon]$, with the associated oscillator strength.

The experimental spectra of $SrTiO_3$ stands out from the other cubic perovskites' spectra because, while exhibiting the usual double peaked structure, the first peak is the brightest (highest) between the four. The BSE curves reproduce correctly the features of the first peak (including the onset), and in particular the averaged BSE curve estimates accurately the peak intensities. The second structure is, as usual for the cubic perovskites, severely underestimated in the transition energies and simultaneously overestimated in the intensities by the $8 \times 8 \times 8$ BSE curve. The averaged curve

corrects the intensities overestimation but does not shift at all the transition energies, sign that this error is not related to the kpoint convergence.
As usual the IPA curve severely overestimates the two structures' transition energies. We now move to study the $NBANDSV$ convergence, showed in figure 6.9.

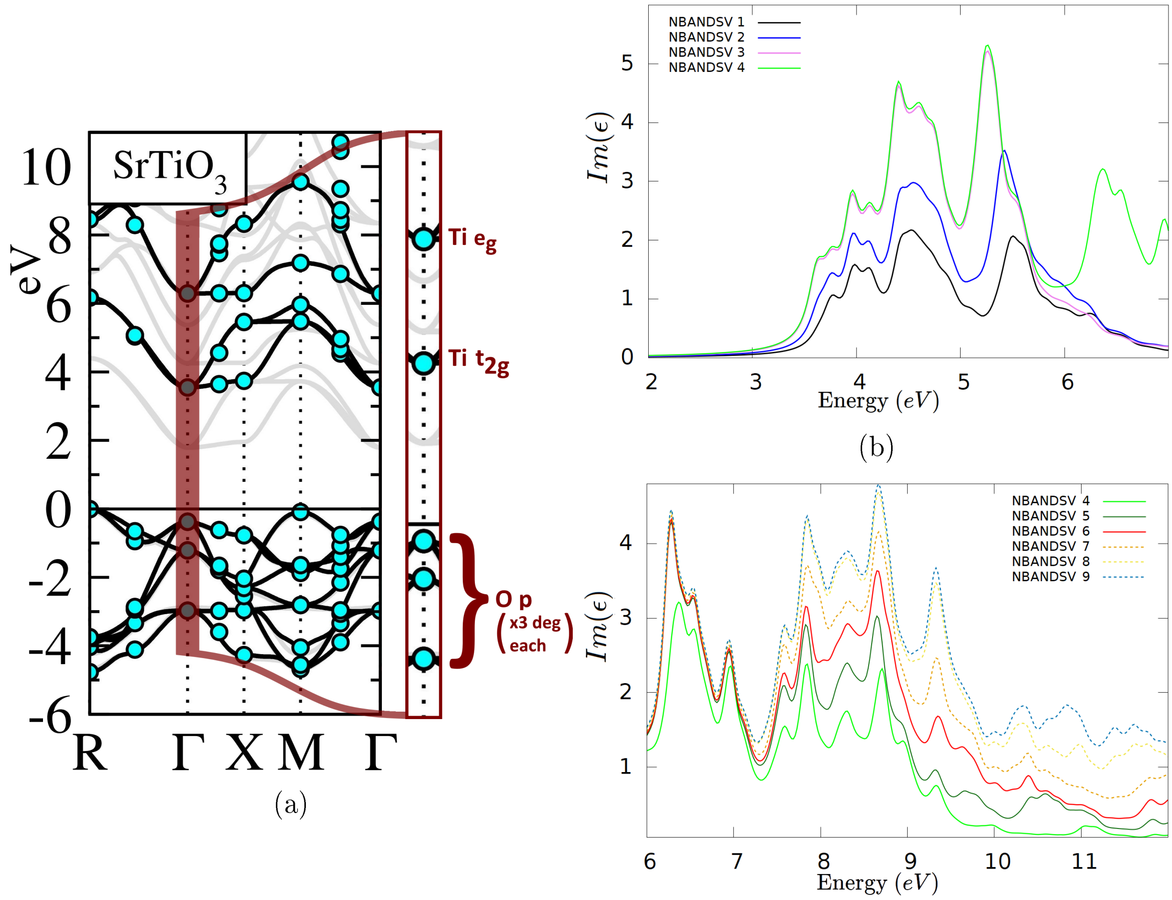

(a)

(b)

(c)

Figure 6.9: (a): bandstructure (taken from [99]), with a focus on the QP-energies at the Γ point and the projected wavefunction character of each band.
(b),(c): Convergence with respect of the number of conduction band (with $NBANDSO$, number of valence bands, fixed) of the (a)first structure, (b)second structure inside $SrTiO_3$'s spectra. The spectra themselves were obtained through a full BSE calculations on a $8 \times 8 \times 8$ mesh.

$SrTiO3$ convergence shows a similar trend as $KTaO_3$, that is the first peak involves only the first three conduction bands and is completely establish by the $O\ p \rightarrow Ti\ t_{2g}$ transitions. However, the first structure's shoulder (range $[6, 7]$ eV) requires also the transition to $Ti\ e_g$ states (corresponding to the $NBANDSV = 5$ curve) to be accounted for.
Conversely the second structure can be described only by including transitions to conduction bands $6, 7, 8$ (not showed in figure 6.15a), where the first two are $Sr\ e_g$ states lying at 11.8 eV (at Γ) and the last one is the $Sr\ s$ state at 12.4 eV at Γ.

We further elaborate on the peaks attribution by studying the excitonic wavefunctions (see figure 6.10). Similarly to $KTaO_3$, the first transition (with corresponds to the first excitonic eigenvalue with non-zero oscillator strength) involves only the triple degenerate highest occupied valence band and lowest unoccupied bands at Γ, with negligible contribution at other kpoints.

The second transition, interestingly, is not localized at Γ and receives the major contribution from the kpoints situated along the $\Gamma - X$ direction. It still involves almost exclusively the highest valence band and the lowest conduction band.

The third transition showed in figure 6.10 is instead almost completely localized at Γ; compared to the first transition, however, the dominating contributions originate no longer from the highest valence bands, but from the bands below (these band have the same character, dominated by $O\ p$).

These results are in full agreement with a recent work by $Begum.et.al$[133].

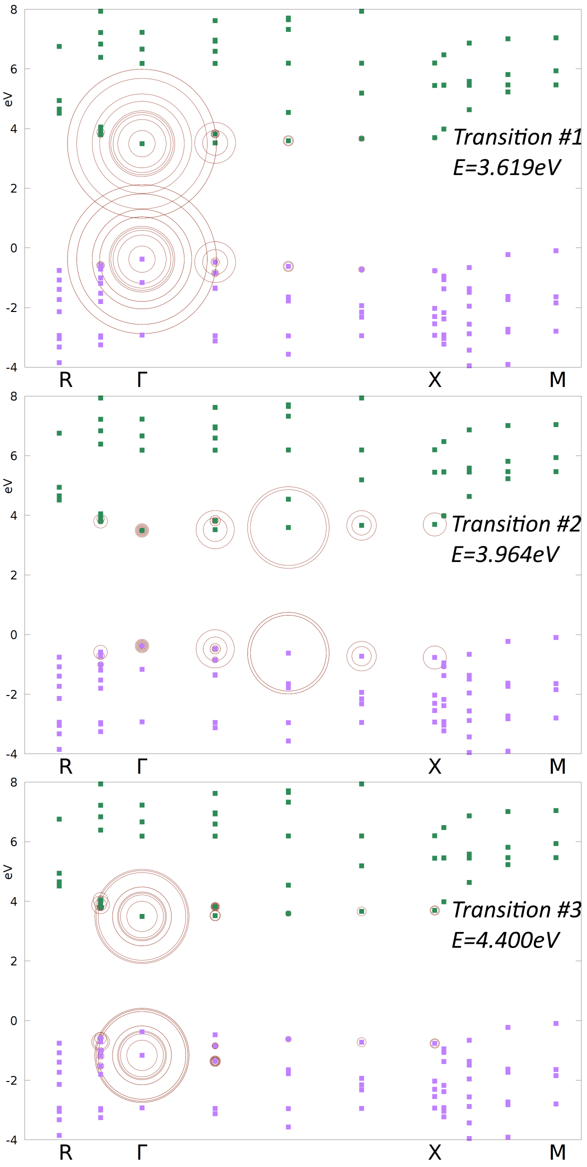

Figure 6.10: Plot of absolute value of the exciton wave function along high symmetry lines in reciprocal space. The circle radius is proportional to $|A^{\lambda}_{c,v,\vec{k}}|$. The transition's numbers refers to the label in figure 6.8b.

SrZrO$_3$

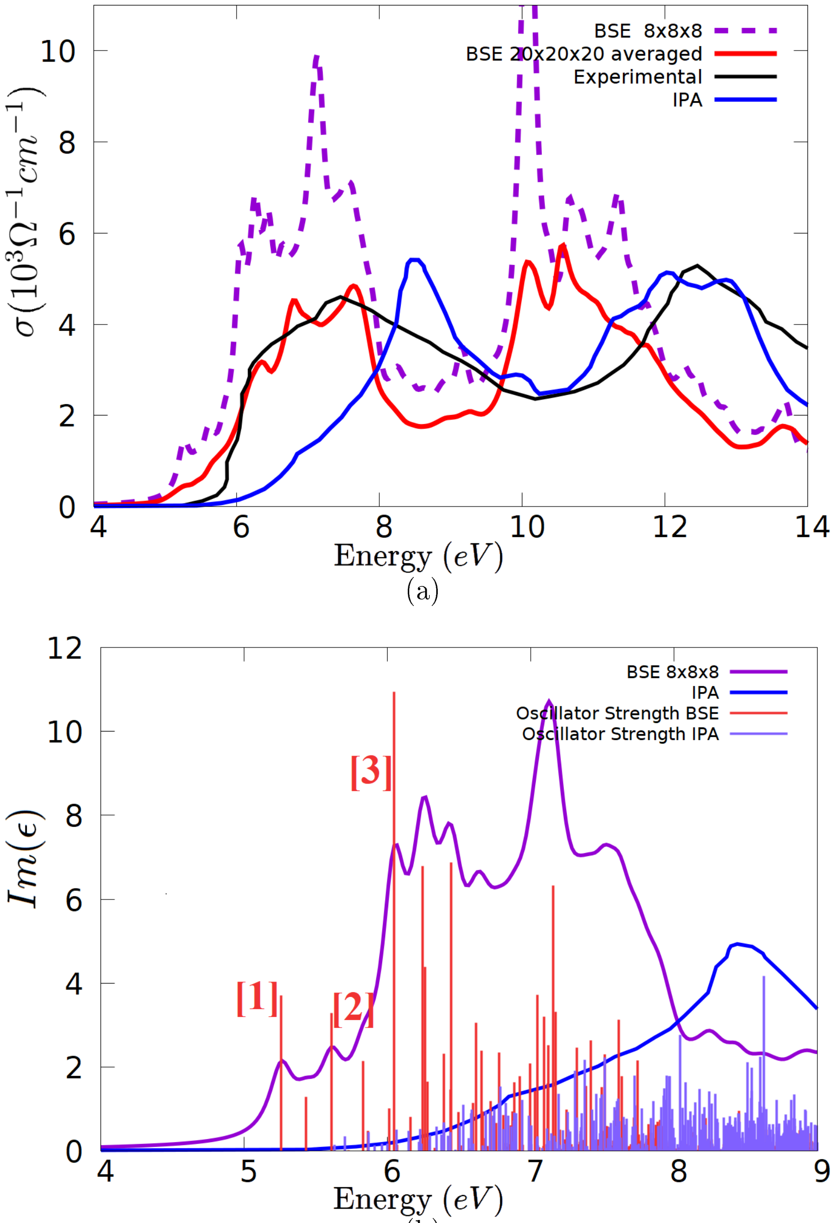

(a)

(b)

Figure 6.11: (a): Spatially averaged optical conductivity ($10^3\Omega^{-1}cm^{-1}$) of $SrZrO_3$, obtained with different approaches: in red through an averaged BSE on a $20 \times 20 \times 20$ mesh ($n \times n \times n = 4 \times 4 \times 4, m \times m \times m = 5 \times 5 \times 5$), in violet through an BSE on a $8 \times 8 \times 8$ mesh, in blue through a IPA on $G0W0$ QP-energies and $8 \times 8 \times 8$ mesh, while the black one is the experimental curve. (b): Zoom of the first structure (range $[4, 9]$ eV) of $\Im[\epsilon]$, with the associated oscillator strength.

In figure 6.11, in a similar way to $KTaO_3$ and $SrTiO_3$, we can identify two structures, a peak plus shoulder between $\sim [6, 9]$ eV and a less pronounced crest between $\sim [11, 14]$ eV. The higher transition energies associated to the first peak with respect to the analogous one of $KTaO_3$ are due to the higher bandgap[99].
The BSE calculation based on an $8 \times 8 \times 8$ mesh underestimates the onset of the experimental first peak by almost 1 eV and almost doubles the experimental peak height; the calculation based on the averaging technique reduces the discrepancy on the onset (but it does not completely erase it). This technique succeeds in reproducing with

excellent agreement the first peak's height, but does underestimate its shoulder.
As in $KTaO_3$, the transition energies of the second structure are underestimated by both BSE calculations; The averaged BSE calculation describes correctly its intensities, while the $8 \times 8 \times 8$ exhibits a very bright peak, which is an artefact due to the coarse kpoint mesh.
The IPA curve severely overestimates the first peak's transition energies, while representing with overall good agreement the second peak.
As we can see from figure 6.11, the compound exhibits strong excitonic effects.

To relate the spectra's feature to the bandstructure we studied (figure 6.12) the convergence with respect to $NBANDSV$:

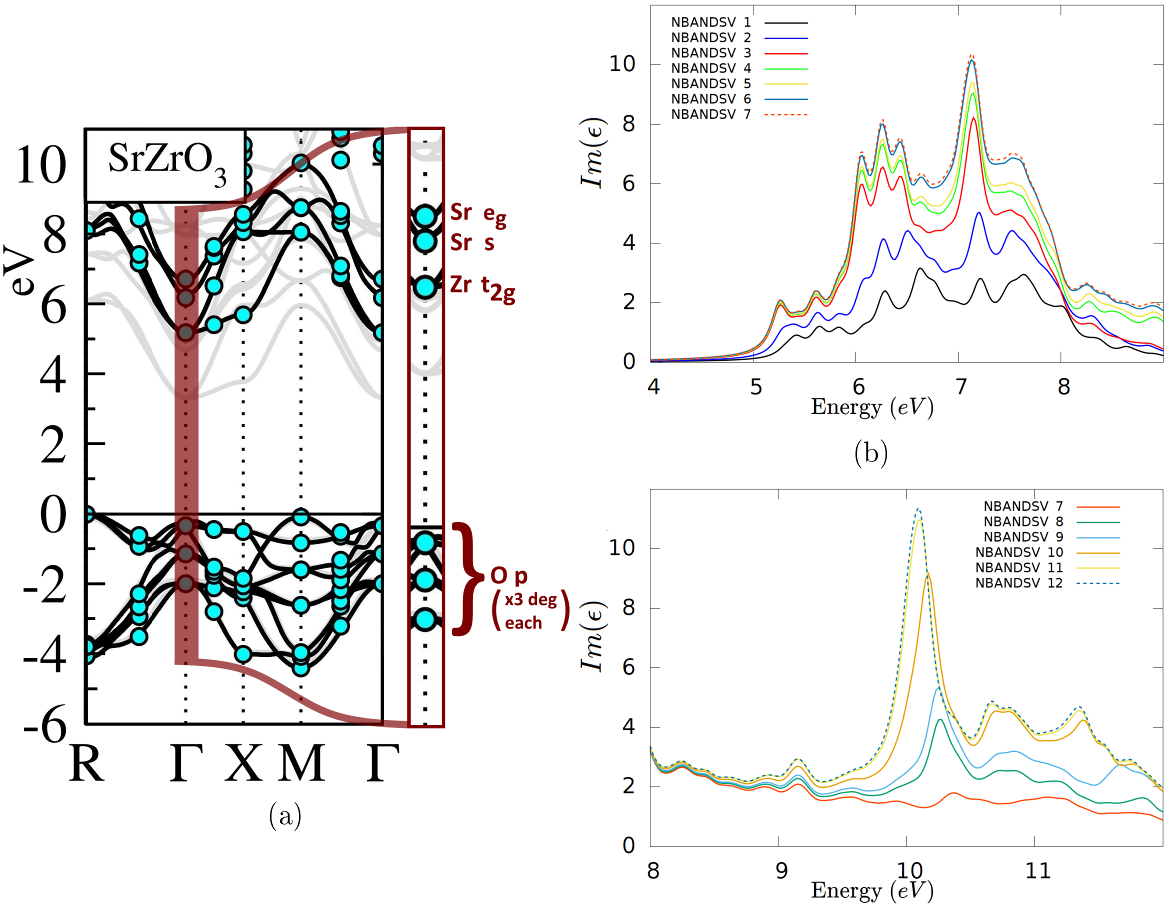

(a)

(b)

(c)

Figure 6.12: (a): bandstructure (taken from [99]), with a focus on the QP-energies at the Γ point and the projected wavefunction character of each band.
(b),(c): Convergence with respect of the number of conduction band (with $NBANDSO$, number of valence bands, fixed) of the (a)first structure, (b)second structure inside $SrZrO_3$'s spectra. The spectra themselves were obtained through a full BSE calculations on a $8 \times 8 \times 8$ mesh.

Figure 6.12 exhibits a marked difference from the previous compounds, that is the first structure requires up to six conduction band ($NBANDSV = 6$ curve) to attain convergence, meaning that transitions from $O\ p$ to $Zr\ t_{2g}$ (*1st, 2nd* and *3rd* conduction bands), $Sr\ s$(*4-th* conduction band) and $Sr\ e_g$(*5, 6-th* conduction bands) are involved.

Although, the structure's onset at 5 eV is described completely by the first three bands. This behaviour can be explained by differences in the bandstructure: for $SrHfO_3$ t_{2g} and e_g bands overlap inside the $\sim [6,8]$ eV range, while for $SrTiO_3$ and $KTaO_3$ (figures 6.6a, 6.9a) these bands have a distinct energy separation.
The second structure is not fully converged until $NBANDSV = 11$: this curve contains contribution from transitions to Zr s states (conduction bands 7, 8 ; degenerate at Γ at 10.3 eV) and to Sr t_2g states(band from 9 to 11, lying at Γ at 10.6 eV).

The first two transitions described in figure 6.13 are associated to the onset of the first structure, as we recall from figure 6.12b (Transition #1 is the first transition with non-zero oscillator strength). The dominant contributions to the excitonic wavefunctions came from the lowest (triply degenerate at Γ) unoccupied bands and highest occupied bands, in agreement with the previous result (with the usual exception of transition #3, where the lower valence bands are involved). Interestingly, the wavefunctions possess a significant magnitude along the $\Gamma - R$ and $\Gamma - X$ directions.

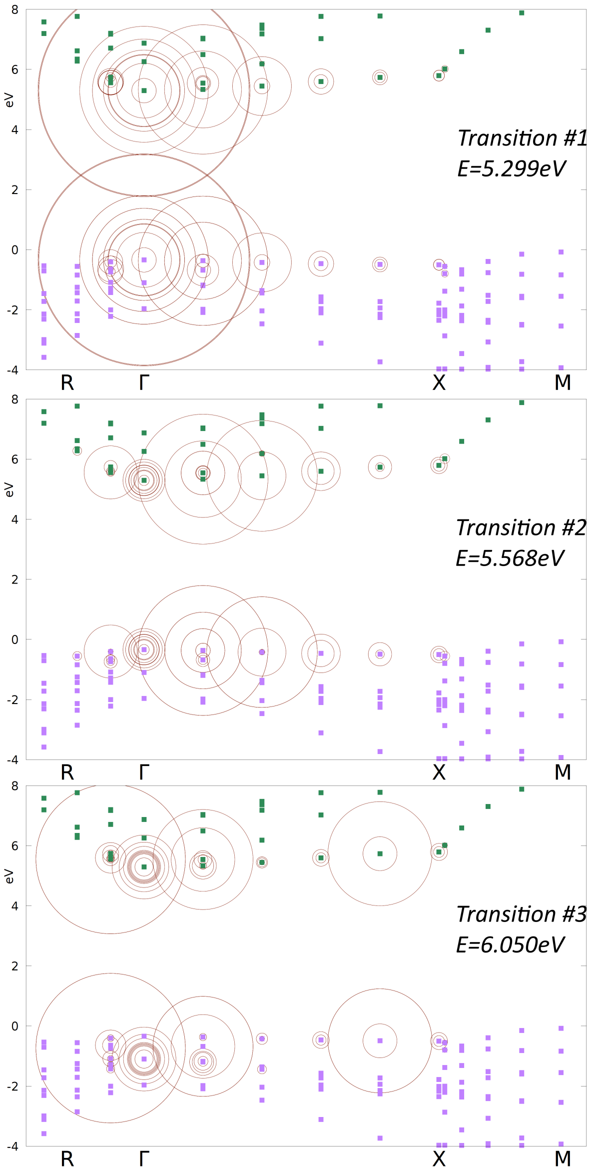

Figure 6.13: Plot of absolute value of the exciton wave function along high symmetry lines in reciprocal space. The circle radius is proportional to $|A^{\lambda}_{c,v,\vec{k}}|$. The transition's numbers refers to the label in figure 6.11b.

SrHfO$_3$

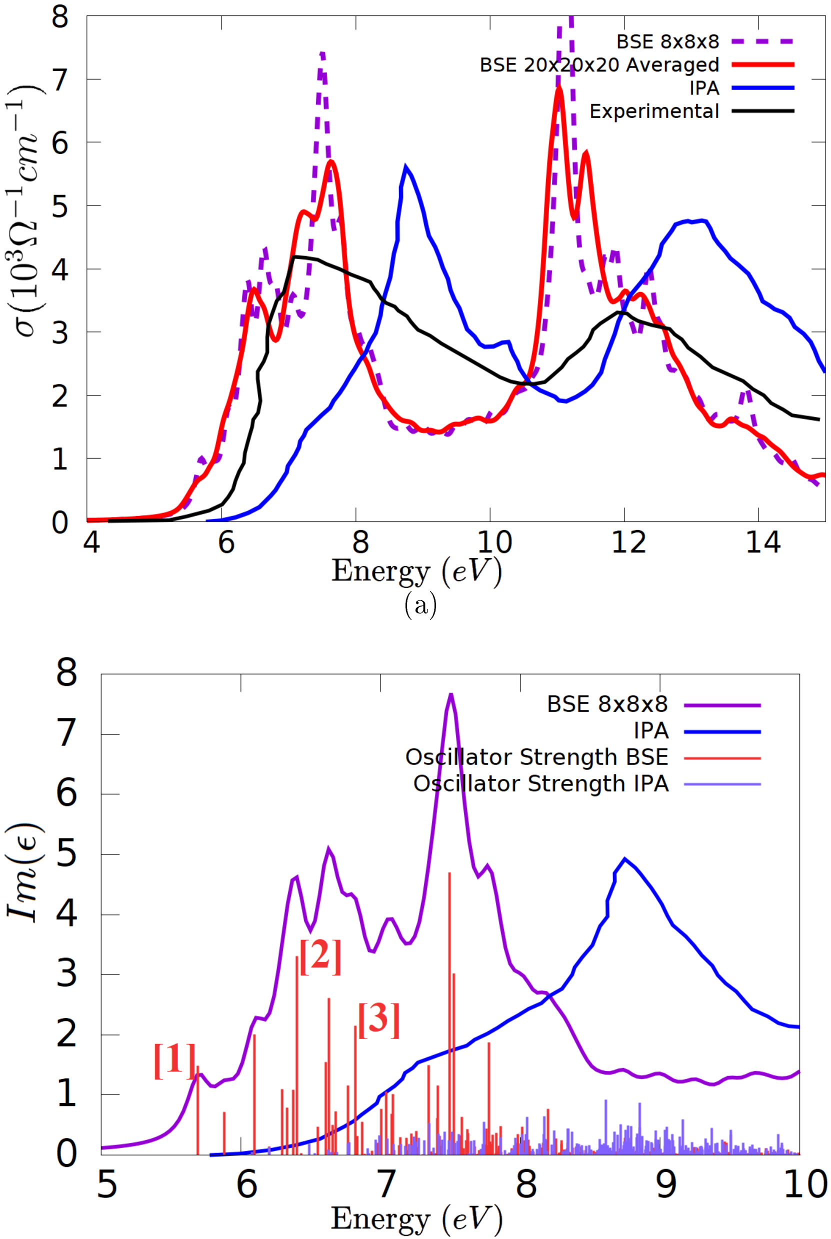

(a)

(b)

Figure 6.14: (a): Spatially averaged optical conductivity $(10^3\Omega^{-1}cm^{-1})$ of $SrHfO_3$, obtained with different approaches: in red through an averaged BSE on a $20\times20\times20$ mesh $(n\times n\times n = 4\times4\times4, m\times m\times m = 5\times5\times5)$, in violet through an BSE on a $8\times8\times8$ mesh, in blue through a IPA on $G0W0$ QP-energies and $8\times8\times8$ mesh, while the black one is the experimental curve. (b): Zoom of the first structure (range $[5, 10]$ eV) of $\Im[\epsilon]$, with the associated oscillator strength.

As usual in the cubic perovskites, $SrHfO_3$'s spectra exhibits two prominent structures. While the first peak is correctly reproduced by both BSE curves, its onset's transition energies are consistently underestimated by $\sim 0.5 - 0.6$ eV. Because the two curves follow the same trend and are almost superimposed in the range $\sim[4, 7]eV$, this is probably unrelated to the kpoints convergence. As in the two previous compounds, the $8\times8\times8$ mesh BSE calculation overshoots severely the first peaks' height, while the averaged BSE curve reaches a much better agreement.

However, as in $SrZrO_3$, the first peak shoulder height is underestimated and the second peak's transition energies are too low.
The IPA picture severely overshoots the first structure's energy transitions while describing more accurately the second structure's onset.
As we can see from figure 6.14, the redshift due to the excitons contribution is considerable.

The $NBANDSV$ convergence, which allows to determine the role of single conduction bands to the spectra, is performed below:

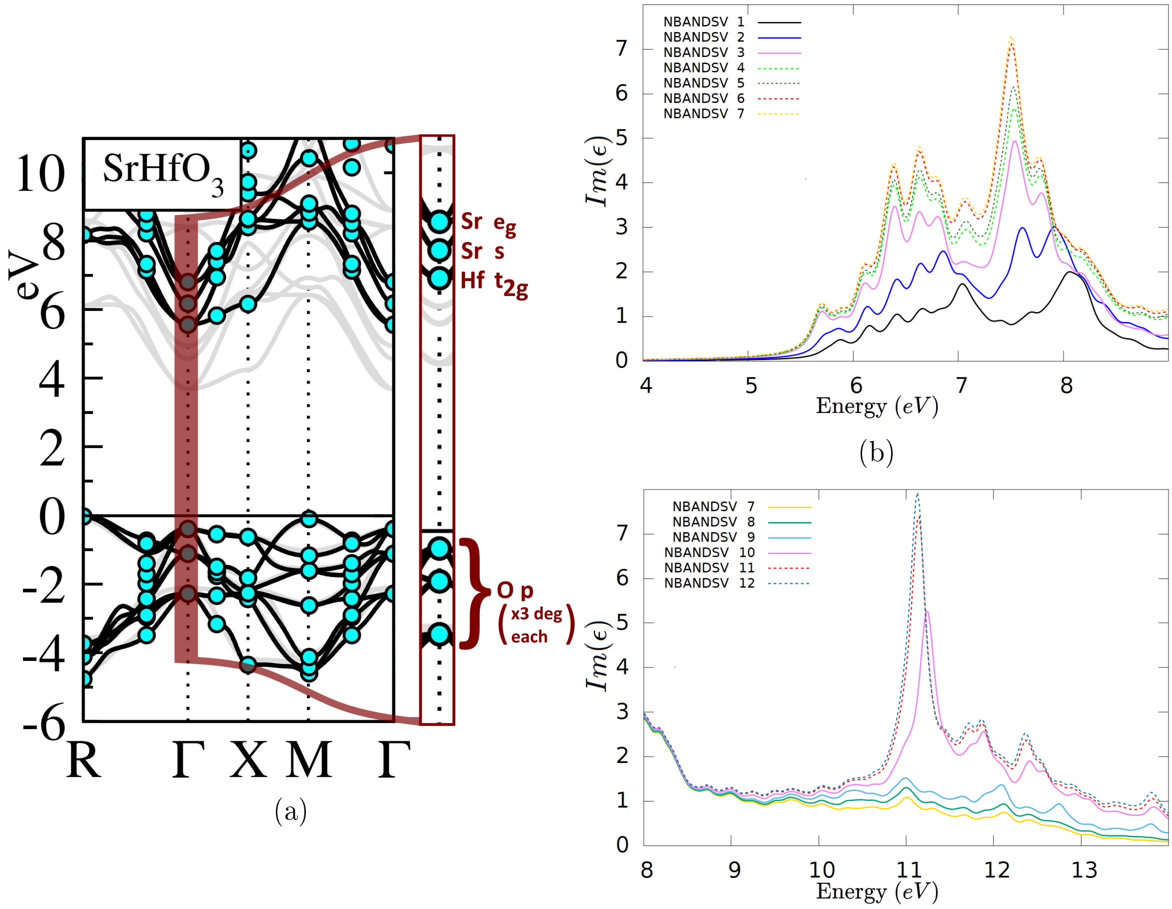

(a)

(b)

(c)

Figure 6.15: (a): bandstructure (taken from [99]), with a focus on the QP-energies at the Γ point and the projected wavefunction character of each band.
(b),(c): Convergence with respect of the number of conduction band (with $NBANDSO$, number of valence bands, fixed) of the (a)first structure, (b)second structure inside $SrHfO_3$'s spectra. The spectra themselves were obtained through a full BSE calculations on a $8 \times 8 \times 8$ mesh.

The interpretation provided by figure 6.15 is quite similar to $SrZrO_3$'s one: To converge the first structure the inclusion of $O\ p \rightarrow Hf\ t_{2g}$ transitions (*1st, 2nd* and *3rd* conduction bands) is not enough and we have to take into account $O\ p \rightarrow Sr\ s$ (*4-th* conduction band) and $O\ p \rightarrow Sr\ e_g$ (*5, 6-th* conduction bands) transitions. The behavior can be explained, as in $SrZrO_3$, by the energy range overlap of $Hf\ t_{2g}$ and $Sr\ s$, $Sr\ e_g$ bands.

The second structure (range $[10, 12]$ eV) require up to conduction bands 11 to be converged: these include $Hf\ e_g$ (*7, 8-th* conduction bands degenerate at Γ at 10.31 eV), $Sr\ t_{2g}$ (*9-11-th* conduction bands at 10.61 eV at Γ).

We now discuss the contributions to the excitonic wavefunctions $|A^{\lambda}_{c,v,\vec{k}}|$ for some selected transitions (figure 6.16).
The first transition (which is the first transition with non-zero oscillator strength) is strongly localized at Γ, with only marginal contribution from the direction $\Gamma - X$, and involves only the highest occupied and lowest unoccupied bands. The second transition (which corresponds to the beginning of the first structure, see figure 6.14) follows a very similar behaviour: the only difference is the dominating valence band, which is the second-highest one (instead of the highest one).

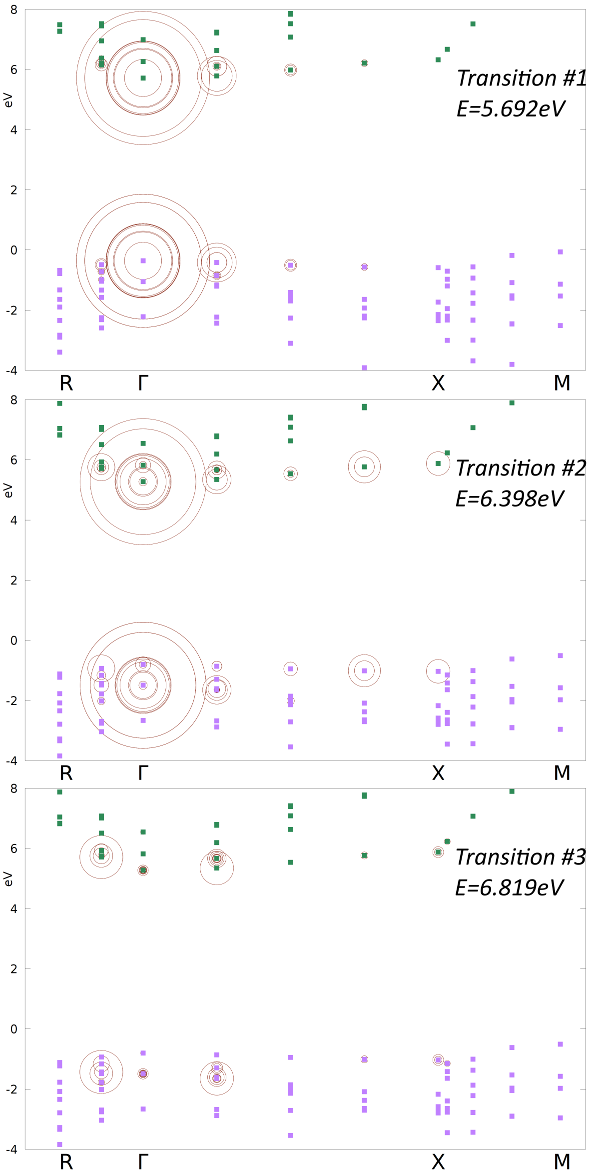

Figure 6.16: Plot of absolute value of the exciton wave function along high symmetry lines in reciprocal space. The circle radius is proportional to $|A^{\lambda}_{c,v,\vec{k}}|$. The transition's numbers refers to the label in figure 6.14b.

6.5 Addendum: Suggestions from Hybrid calculations

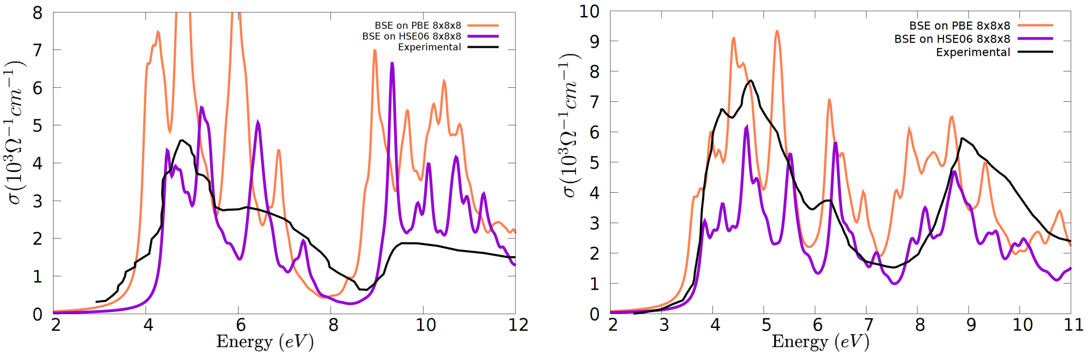

Figure 6.17: Comparison between the experimental data and the optical conductivity of $SrTiO_3$ and $KTaO_3$. The BSE curves were obtained using different starting points: a standard $DFT(PBSE)$ calculation and a hybrid$(HSE06)$ one. all methods employed a $8 \times 8 \times 8$ mesh.

Recently *Begum et.al*[133] have discussed how replacing the starting point for the $G0W0$ method from a PBE to a *hybrid* calculation could improve the description of $SrTiO_3$'s dielectric function. We replicated their result and employed the same approach for $KTaO_3$.
The two spectra show very intense peaks which, as discussed in the previous sections, are artifacts of the coarse mesh employed ($8 \times 8 \times 8$ for both calculations) and must not be attributed to the starting hybrid calculations.
as we can see in figure 6.17, the agreement regarding the peaks transition energies between the experimental data and the BSE curves is greatly improved. The positions of the peaks in the first structure are very well reproduced, and, above all, the error of the second structure's position is significantly reduced.

In fact, in the previous four calculations we found that the BSE methods consistently underestimated the second structure, while the IPA could reach a somewhat more accurate reproduction of its onset. We postulate that the initial partial success of the IPA spectra (based on a $G0W0@PBE$) in reproducing the second structure's onset can be explained as a error cancellation:

1. The first error was due to the absence of excitonic effects; these effects, as we have already discussed, produce a redshift of the features in the spectra.

2. the second error si due to an inaccurate description of localized d states made by the starting $DFT(PBE)$ calculation. A better account of these states produces a blueshift (with respect to the calculations based on PBE).

The IPA spectra lack both corrections: the errors thus partially compensate themselves. The BSE calculations based on PBE include instead only one of the two corrections: this is the reason of the error in the original BSE calculations. Finally, the inclusion of the hybrid starting point improves the description of the localized d states. Moreover the necessity to choose accurately the starting point for the $G0W0$ methods when dealing with compounds with d orbitals is already well-known in literature [134, 135, 136, 137].

Chapter 7

Large perovskites: Lanthanide series, $SrMnO_3$, $4d$ and $5d$ TMO perovskites

7.1 Convergences

As outlined in section 6.1, the first steps to perform a BSE run are the two convergence studies. Let's recall the two aspects (expressed in section 6.1) that make these studies difficult to perform - *are they demanding also for the large perovskites subset?*

1. The first point (the scaling of the $G0W0$ with respect to the number of kpoints) is somewhat aggravated by the fact that the majority of the large perovskites exhibit distorted structures and different types of antiferromagnetism ordering (see tables 4.1 and 4.2). Because of that their cells possess lower symmetry than the cubic ones, making calculations with the same kpoint number more costly (with respect, again, to the cubic ones)[1].

2. However, to describe the magnetic orderings and the distortions we must use a *large* supercell containing up to 28 atoms (instead of 5): a larger supercell corresponds to a smaller Brillouin Zone, thus strongly reducing the demand of dense kpoint meshes. In fact, as we well see, this aspect is less crucial for the large perovskites.

3. The memory requirement of the BSE approach becomes instead critical for this set. This is caused by the high number of atoms inside the supercell (up to 28 atoms for Ca_2RuO_4), which imposes a very high number of bands needed to converge the spectra.
   For example, the supercell of the perovskites in the La series contains 12 O atoms, each one contributing with 6 p orbitals; thus a total of 48 bands must be included only to describe the $O-p$ levels. While the number is material-dependent (and in particular depend on the bandstructure of the considered compounds), some perovskites require values of $NBANDSO$ or $NBANDSV$ over 60 to describe the spectra in the range $[0, 10]$ eV.
   This, in turn, make the requirement on the memory side formidable: for example, in the BSE run for $LaCrO_3$ (with mesh $5 \times 4 \times 5$ and $NBANDSV = NBANDSO = 32$) the BSE matrix alone occupied $\sim 5.8GB$ *per core* ($\sim 380GB$ total).

---

[1] we recall that the $G0W0$ implementation exploits the cell symmetry.

Compound	kpoint mesh	*NBANDSV* / *NBANDSO*	Total memory required
$LaScO_3$	$5 \times 5 \times 3$	$32\,/\,32$	$\sim 207\,GBytes$
$LaTiO_3$	$5 \times 3 \times 5$	$34\,/\,34$	$\sim 824\,GBytes$
$LaVO_3$	$5 \times 3 \times 5$	$30\,/\,30$	$\sim 387\,GBytes$
$LaCrO_3$	$5 \times 3 \times 5$	$32\,/\,32$	$\sim 380\,GBytes$
$LaMnO_3$	$6 \times 6 \times 4$	$26\,/\,26$	$\sim 963\,GBytes$
$LaFeO_3$	$5 \times 3 \times 5$	$34\,/\,34$	$\sim 762\,GBytes$

Table 7.1: Memory requirement for the standard *BSE* calculations for the *La* series. The *total memory* is calculated multiplying the total memory per core (flag *total amount of memory used by VASP on root node*) times the core number employed.

We face thus an almost opposite situation with respect to the cubic perovskites: the kpoint convergence is less problematic (due to the smaller Brillouin Zones associated to the larger supercells) and the *NBANDSV/O* one proves complex, and becomes especially critical for the *La* series, as we can see from table 7.1:

As we will see in section 7.2, most of the *La* compounds require the inclusion of far more bands (often more than double) than the ones showed in table 7.1 to reach a meaningful convergence inside the range $[0, 10]$ eV. Recalling that *BSE* memory requirements scales as $\sim (NBANDSO * NBANDSV * N_{kpoints})^2$, a converged calculation becomes quickly too demanding for a standard calculation due to memory constraints.
To address this matter we discarded the *mBSE* approach (the *mBSE* and *BSE* methods have similar memory requirement[2]), and fully employed the *averaging* technique (as described in section 6.3). In this way each single calculation in this technique uses a much coarser mesh, which reduces the memory demand to acceptable values.

---

[2] As detailed in the online manual `https://cms.mpi.univie.ac.at/wiki/index.php/BSE_calculations` (url checked on October 3, 2019).

7.2 *La* series

LaScO$_3$

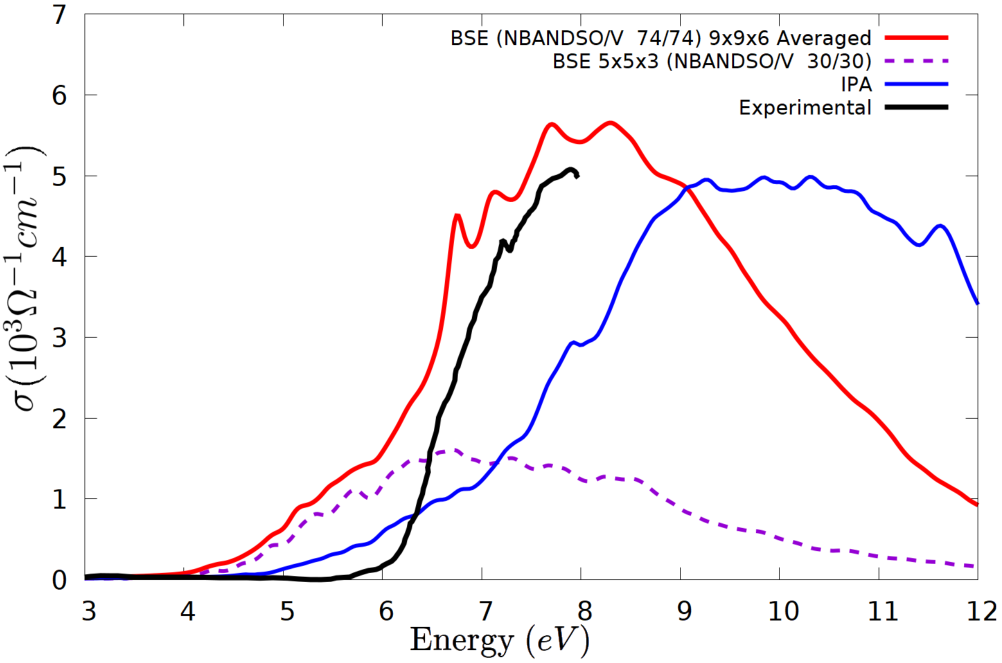

Figure 7.1: (Spatially averaged optical conductivity $(10^5\Omega^{-1}cm^{-1})$ of $LaScO_3$, obtained with different approaches: in red through an averaged BSE on a $9 \times 6 \times 9$ mesh $(n \times n \times n = 3 \times 3 \times 2, m \times m \times m = 3 \times 3 \times 3)$, in violet through an BSE on a $5 \times 3 \times 5$ mesh, in blue through a IPA on $G0W0$ QP-energies and $5 \times 5 \times 3$ mesh, while the black one is the experimental curve.

Before discussing the comparison with the experimental data, we point out the very high number of bands (equal to $NBANDSV = NBANDSO = 74$) required to converge the optical conductivity up to 9 eV. A standard BSE calculation with these parameters would be computationally infeasible due to memory requirements[3], as we discussed in section 7.1. Moreover, the standard BSE calculation on the $5 \times 5 \times 3$ mesh does not reach convergence even in the lower part of the spectra (i.e. < 6eV). We will explain the reason of this behaviour in the next section.
Both the IPA and the BSE describe correctly the spectra from a qualitative point of view, with its wide single structure: however, from a quantitative point of view both approaches strongly underestimate its onset (the IPA one by $1.0 - 1.1$ eV and the averaged BSE by $1.8 - 1.7$ eV on the onset). This error can be partially related to the underestimation of experimental band gap (equal to 6.0 eV) performed by the $G0W0$ approach, which predicts a value of 4.56 eV (see table 4.2).

If the IPA achieves a better account of the onset, this result is no longer valid for the main peak: the IPA severely overestimate it (by about $1.2 - 1.3$ eV), and the introduction of the excitonic effects reduce the error to ~ 0.4 eV.

---

[3] The oscillator strengths for the IPA and BSE curves are extracted from the non averaged calculation. However, for $LaScO_3$ this approach results inadequate and insufficient to reproduce the spectra even at the onset, and thus we omit them.

We conclude this paragraph by observing that the excitonic redshift is prominent in $LaScO_3$: the shift at the onset is equal to ~ 0.9 eV, but it reaches ~ 1.9 eV between the peaks' centers of mass.

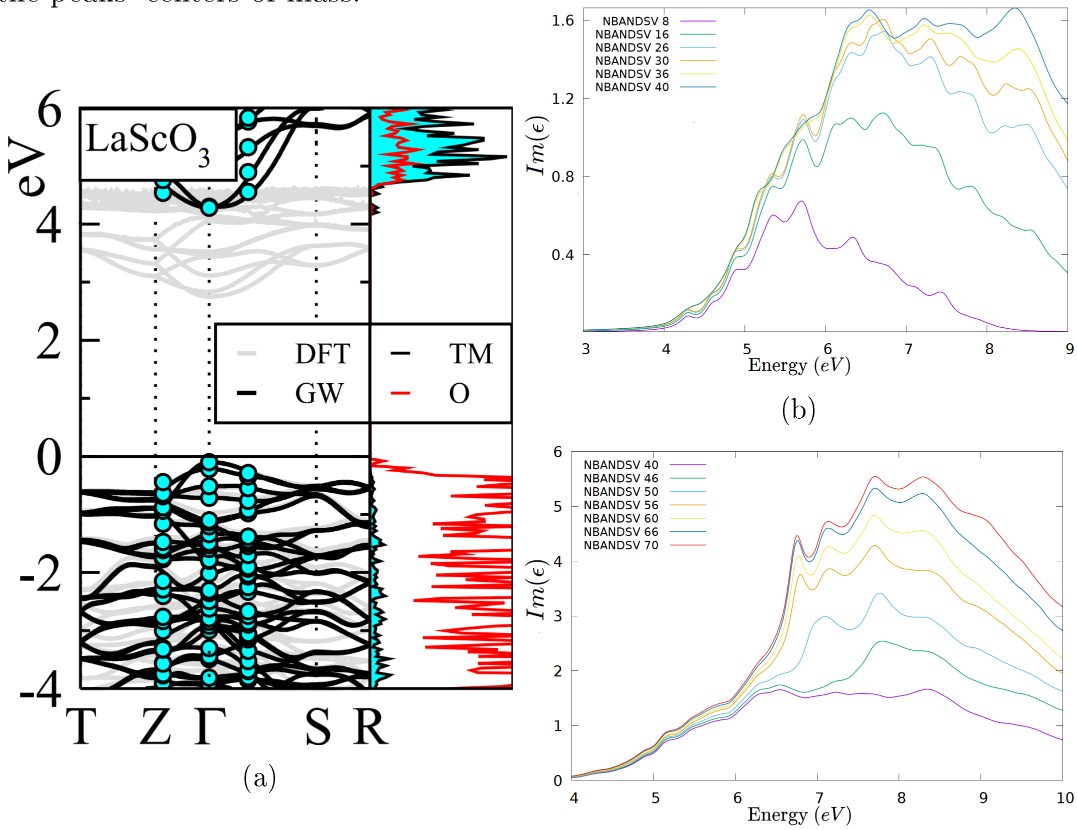

(a)

(b)

(c)

Figure 7.2: (a): bandstructure (taken from [99]), with the Density of States of $TM-d$(shadow, cyan line) and $O-p$ (full line, red).
(b),(c): Convergence with respect of the number of conduction band (with $NBANDSO =$ number of valence bands fixed).

$LaScO_3$ is a band insulator with a $3d^0$ configuration, and this implies that its spectra lacks the Mott peak visible in the other compound of this series, which can be observed only when the $3d$ orbitals start to be filled. The structure visible in the spectra is thus identifiable as a peak formed by transitions between the $O\ p$ valence bands and the d conduction bands. The first 8 conduction bands have a $Sc\ d$ character and reside up to 7.2 eV over the Fermi energy (at Γ); however, their contribution to the peak is fairly limited.

We can observe (figure 7.2c) that transitions involving bands between the *40-th* and the *70-th* are needed to converge the peak and provide the major part of the structure. Bands from *37-th* to the *46-th* (range $[8.4, 8.8]$ eV at Γ) have a mixed $La\ d/Sc\ d$ character; inside the range $[47, 57]$ ($\sim [7.1, 8.4]$ eV at Γ) $Sc\ d$ forms the main constituent, and for bands from *58-th* on (> 8.4 eV at Γ) it becomes mixed with $La\ d$.

Besides, the bands between the *26-th* and the *40-th*, with a predominant $La\ d$ character, reside at very high energy ($\sim [9.3, 9.7] eV$ at Γ) and thus give only a minor contribution (see figure 7.2b). This also explains why the standard calculation with $NBANDSV/O = 30/30$ fails to reproduce the peak.

$LaTiO_3$

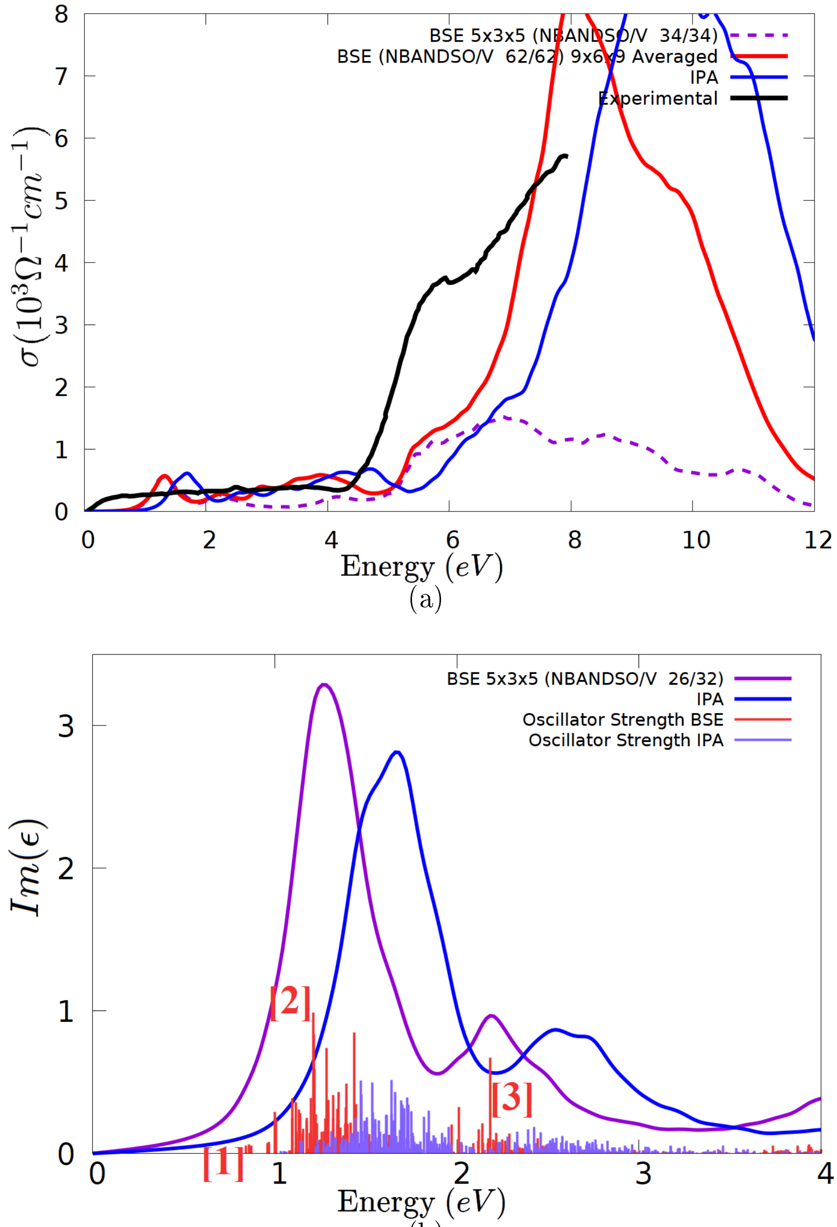

(a)

(b)

Figure 7.3: (a): Spatially averaged optical conductivity $(10^5\Omega^{-1}cm^{-1})$ of $LaTiO_3$, obtained with different approaches: in red through an averaged BSE on a $9 \times 6 \times 9$ mesh $(n \times n \times n = 3 \times 2 \times 3, m \times m \times m = 3 \times 3 \times 3)$, in violet through an BSE on a $5 \times 3 \times 5$ mesh, in blue through a IPA on $G0W0$ QP-energies and $5 \times 3 \times 5$ mesh, while the black one is the experimental curve. (b): Zoom of the first structure (range $[0, 4]$ eV) of $\Im[\epsilon]$, with the associated oscillator strength.

Before discussing the comparison with the experimental data and the spectra's details, we briefly consider the kpoint and conduction bands convergences. First, we can see that within the range $[0, 6]$ eV the averaged BSE calculation and the standard one superimpose consistently, sign that the kpoint convergence is achieved. Secondly, the standard BSE calculation with $NBANDSV/O = 34/34$ fails to reach convergence for energies > 5 eV, making it necessary to employ the averaging technique. This behavior *is shared between all studied compounds in the La series*, thus confirming the proposition made in section 7.1 regarding the kpoint convergence.

From a qualitative point of view, the *BSE* and *IPA* calculations reproduce the main feature of the experimental spectra[120]: a first feature in the region < 2 eV and an intense peak starting at 4 eV. *Arima et.al.* assign the former peak to a Mott transition and the latter to a charge transfer transition, and our results validate this attribution, as we will discuss in the next paragraph.
However, from a quantitative point of view significant discrepancies can be observed. The Mott feature at < 2 eV is overestimated by about ~ 0.5 eV in the transition energies by the *BSE* approach; the intense charge transfer peak is severely overestimated by all calculations, even if the *BSE* one partially reduces this error.
The redshift effect due to excitonic interactions is limited in the first peak, about ~ 0.3 eV (figure 7.3b), and much more marked for the charge transfer peak (about $\sim 0.7-1.0$ eV); moreover the *CT* peak lineshape is partially altered.

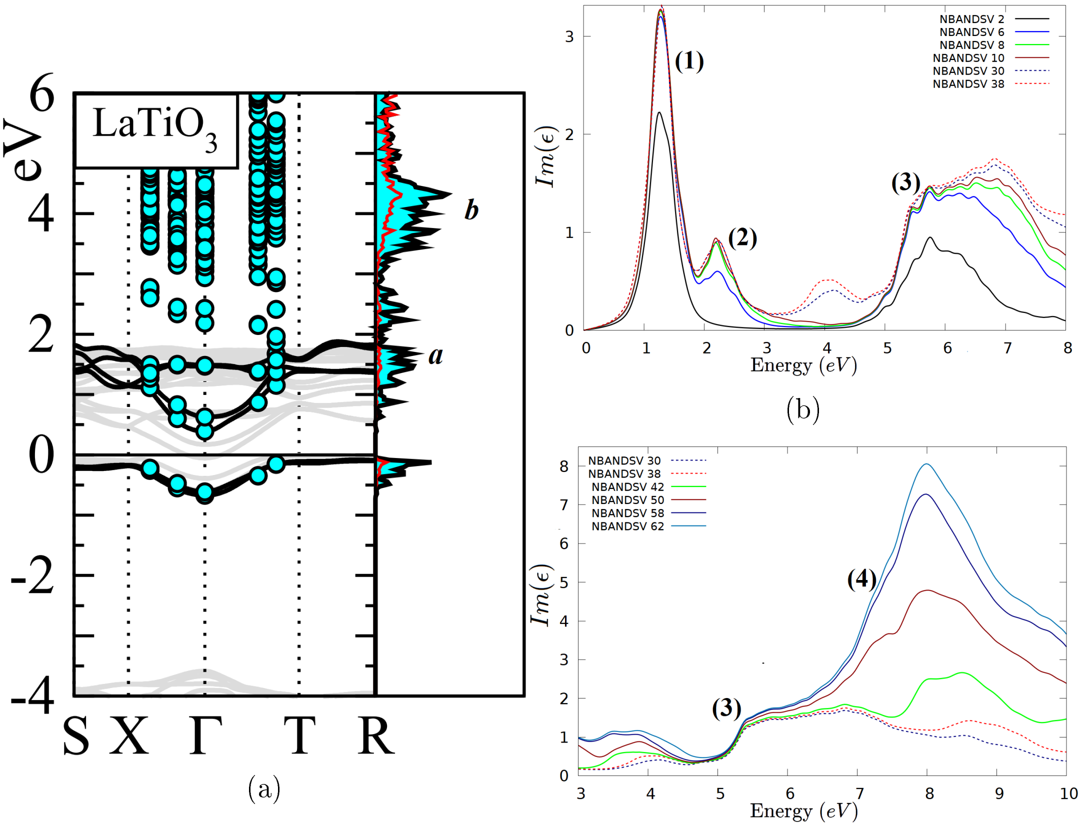

(a)

(b)

(c)

Figure 7.4: (a): bandstructure (taken from [99]), with the Density of States of $TM-d$(shadow, cyan line) and $O-p$ (full line, red).
(b),(c): Convergence with respect of the number of conduction band (with $NBANDSO =$ number of valence bands fixed).

The Mott peak (feature (1)) is completely converged by $NBANDSV = 6$, although the main contribution is given by transitions to the first *two* bands; these first 6 conduction bands lie in the energy range $[0.7, 2.6]$ eV at Γ, have predominant Ti d character (between 40% and 90%), and can be qualitatively assigned to structure a in the density of states.
The shoulder to the Mott peak (feature (2)) is instead determined by the first eight bands, that however belong to the the same structure in the density of states.

Only transitions to two different set of conduction bands are associated to the charge transfer peak. The first 8 conduction bands form a first structure (feature (3)), and taking into account transitions to conduction bands from 10 to 38 ($\sim [3.9, 5.0]$ eV at Γ) doesn't substantially modify this structure. These bands have a main $La\ f$ character, with a total d percentage between 3% and 30%.
The conduction bands from 39 up to 62 give the predominant contribution to the charge transfer structure: these bands lie in the energy range $[3.5, 4.8]$ eV over the Fermi energy at Γ (roughly including structure b in the density of states) and have a mixed character between $La\ d$ and $Ti\ d$.

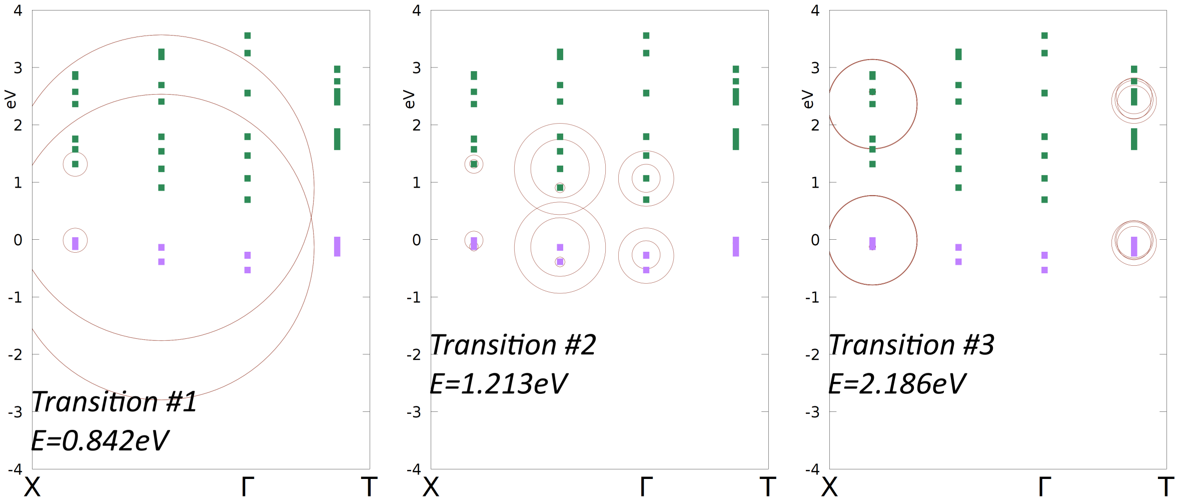

Figure 7.5: Plot of absolute value of the exciton wave function along high symmetry lines in reciprocal space. The circle radius is proportional to $|A^{\lambda}_{c,v,\vec{k}}|$. The transition's numbers refers to the label in figure 7.3b.

We now analyze the wavefunctions associated to three transitions belonging to the first structure (transition #1 is related to the first eigenvalue with non-zero oscillator strength).
The first two transitions show a similar behavior: a wavefunction localized on the $\Gamma - X$ direction which involves the first and second conduction bands, thus confirming the attribution of this structure to a Mott-type peak.
The third transition displayed (which is associated to the shoulder of the Mott peak) exhibits a slightly different behavior, picking up minor contributions from the $\Gamma - T$ direction.

LaVO$_3$

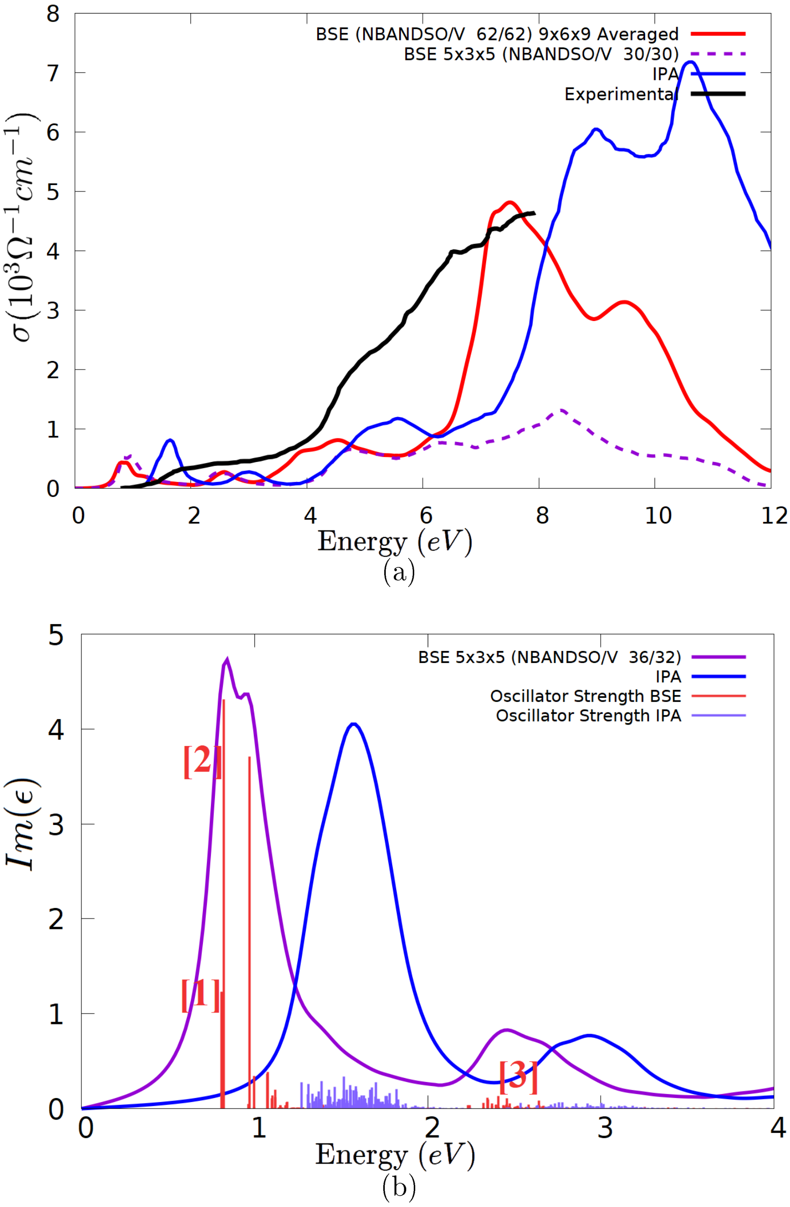

Figure 7.6: (a): Spatially averaged optical conductivity $(10^5\Omega^{-1}cm^{-1})$ of $LaVO_3$, obtained with different approaches: in red through an averaged BSE on a $9\times6\times9$ mesh ($n\times n\times n = 3\times2\times3, m\times m\times m = 3\times3\times3$), in violet through an BSE on a $5\times3\times5$ mesh, in blue through a IPA on $G0W0$ QP-energies and $5\times3\times5$ mesh, while the black one is the experimental curve. (b): Zoom of the first structure (range $[0,4]$ eV) of $\Im[\epsilon]$, with the associated oscillator strength.

$LaVO_3$ spectra shows very similar characteristics to $LaTiO_3$'s one: A Mott peak in the region < 3 eV and a bright charge transfer peak in the region > 4 eV.
The BSE curves underestimate the transition energies of the Mott peak's onset (by about $\sim 0.6-0.8$ eV), while the IPA one describes them more accurately.
As in $LaTiO_3$, the transition energies of the charge transfer structure are overestimated by both types of calculation; however, the redshift due to the excitonic effect partially compensates this error.
The lineshapes obtained by the IPA and BSE simulations are quite similar (almost only shifted) in the region $[0,6]$ eV (the redshift amounts at $\sim 0.6-0.7$ eV on the

onset); the charge transfer structure instead shows a pronounced weight transfer to lower energies and a redshift $\sim 1.0 - 1.2$ eV.

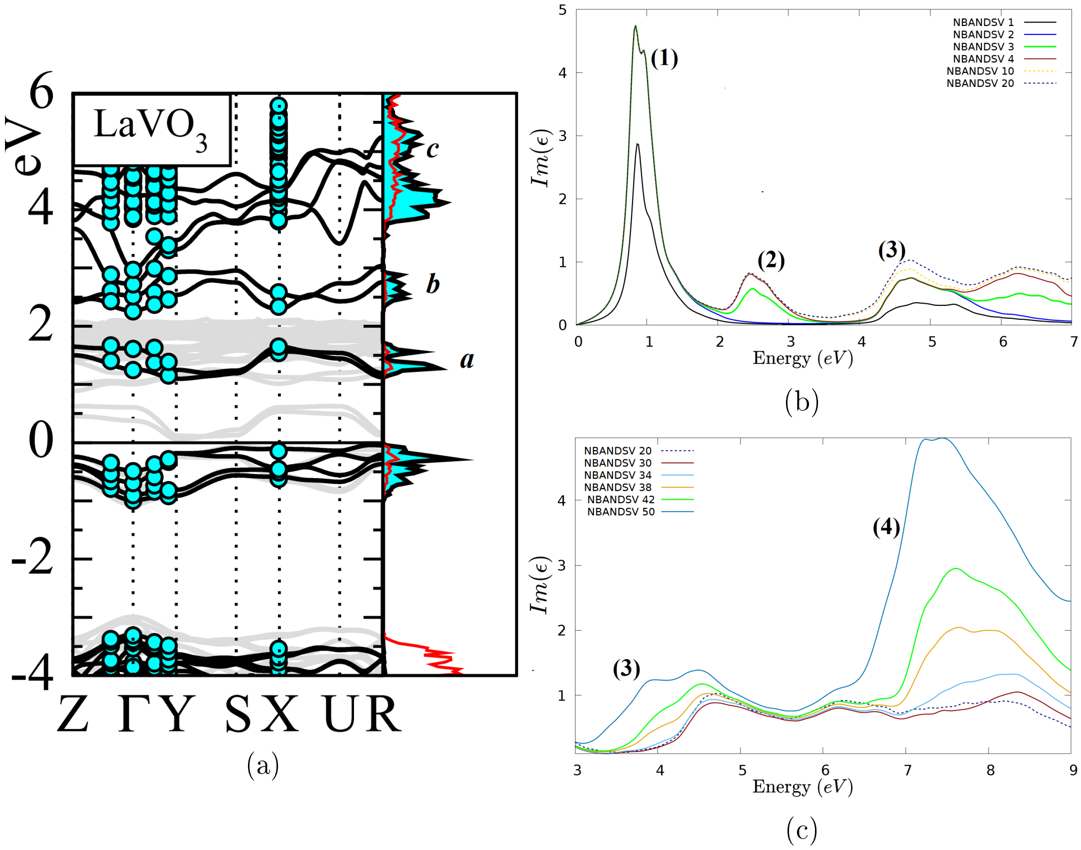

(a)

(b)

(c)

Figure 7.7: (a): bandstructure (taken from [99]), with the Density of States of $TM - d$(shadow, cyan line) and $O - p$ (full line, red).
(b),(c): Convergence with respect of the number of conduction band (with $NBANDSO =$ number of valence bands fixed).

The spectra shows very similar features to the ones exhibited by $LaTiO_3$, and thus we adopt the same numbering. The peak in the Mott structure (inside the energy range $[1, 2]$ eV, feature (1)) is completely converged by considering the first two conduction bands, which correspond to the structure a in the density of states and have a predominant d character ($\sim 70\%$ at Γ). Therefore the attribution of the first structure to a Mott-type transition is supported.
Both in $LaTiO_3$ and $LaVO_3$ the first peak's shoulder (energy $[2, 3]$ eV, feature (2) in figure 7.7b) doesn't receive any contributions from the first two bands. However, while in $LaTiO_3$ transitions to bands from the *3-th* to the *8-th* participate, here this feature is completely determined by including only band 3 and 4 (these two bands generate the b structure in the DOS and have a d character $\sim 80\%$ at Γ). This different behavior can be explained by a difference in the conduction part of the two bandstructures:

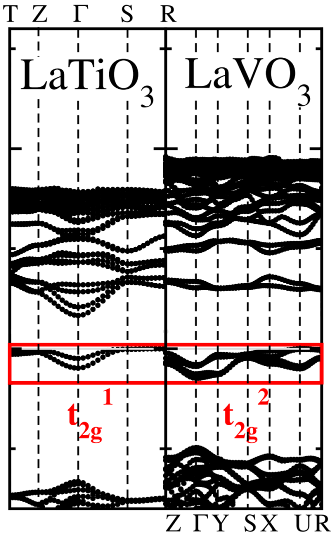

Figure 7.8: $HSE06$ bandstructures of $LaTiO_3$ and $LaVO_3$. From [138].

in $LaVO_3$ the bands starting from the *3-rd* on are shifted to higher energies with respect to $LaTiO_3$ ones, as we can see from figure 7.8 or by comparing the two density of states (for example, in $LaTiO_3$ the *3-rd* and *4-th* bands still contribute to the feature a in the density of states, while in $LaVO_3$ they are associated to feature b).

In a similar manner to $LaTiO_3$, both features (3) and (4) (belonging to the charge transfer structure) receive only minor contributions from the first ten conduction bands (feature (a) and (b) in the density of states). The inclusion of bands between the *10-th* and *30-th* (which have La f character and lies at $[4.7, 5.6]$ eV at Γ, forming the upper part of feature (c) in the density of states) does not provide significant contributions. In fact, the CT structure is mainly determined by bands between *30-th* and *50-th* (lying in the energy range between 3.6 eV and 5.6 eV over the Fermi level and corresponding to the lower part of feature c in the density of states). The La f character is still predominant between the *30-th* and *37-th* bands, while for the last thirteen (from 38 to 50) La d is prevailing (with an average of about $\sim 35\%$ of V d at Γ).

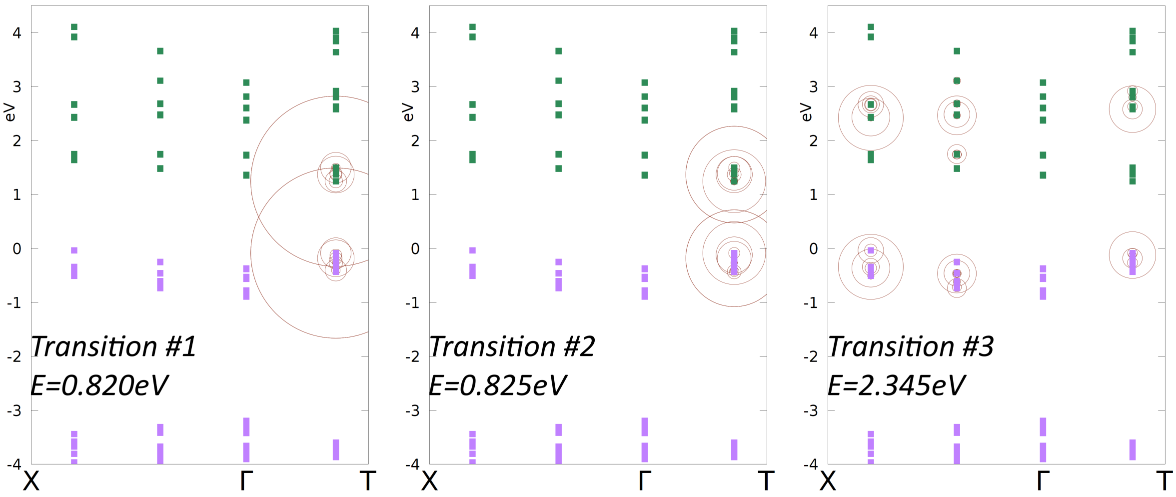

Figure 7.9: Plot of absolute value of the exciton wave function along high symmetry lines in reciprocal space. The circle radius is proportional to $|A^{\lambda}_{c,v,\vec{k}}|$. The transition's numbers refers to the label in figure 7.6b.

We now study the excitonic wavefunctions related to different transitions (as usual transition #1 in figure 7.9 is associated to the first eigenvalue with non-zero oscillator strength). Both the first and the second transitions are related to Mott peak: both involve the lowest conduction bands (in agreement with the previous paragraph), and receive contributions from transitions along the $\Gamma - T$ direction. Conversely, the third eigenvector (which is associated to the shoulder of the Mott peak) is strongly delocalized around $\Gamma - X$, with also notable magnitude along $\Gamma - T$.

$LaCrO_3$

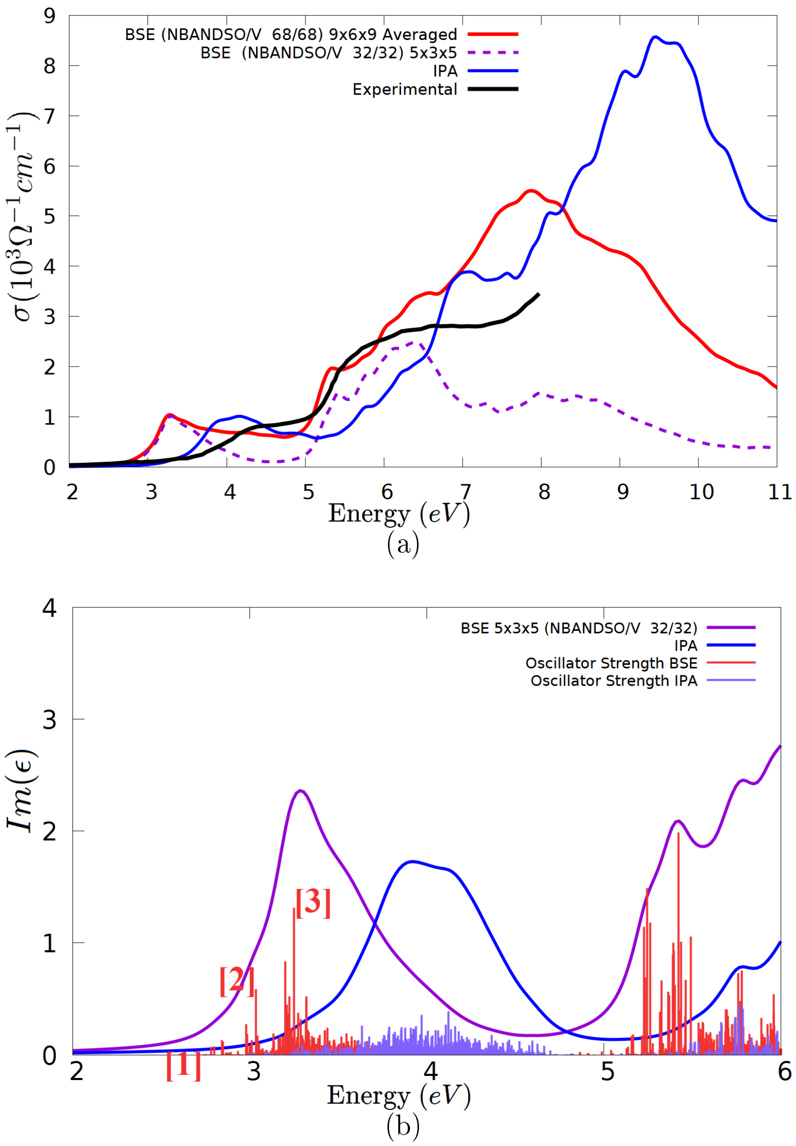

Figure 7.10: (a): Spatially averaged optical conductivity $(10^5\Omega^{-1}cm^{-1})$ of $LaCrO_3$, obtained with different approaches: in red through an averaged BSE on a $9 \times 6 \times 9$ mesh $(n \times n \times n = 3 \times 2 \times 3, m \times m \times m = 3 \times 3 \times 3)$, in violet through an BSE on a $5 \times 3 \times 5$ mesh, in blue through a IPA on $G0W0$ QP-energies and $5 \times 3 \times 5$ mesh, while the black one is the experimental curve. (b): Zoom of the first structure (range $[2, 6]$ eV) of $\Im[\epsilon]$, with the associated oscillator strength.

We can observe inside $LaCrO_3$ spectra the two structures shared by all perovskites belonging to the La series with partially filled $3d$ bands. Moreover, the experimental Mott peak position in $LaCrO_3$ is situated at greater energies than in $LaTiO_3$ and $LaVO_3$, in agreement with the general tendency that electron correlation becomes stronger as the atomic number increases[120].

In a similar fashion to $LaVO_3$, the BSE calculations underestimate this Mott peak's transition energies by $0.8 - 1.0$ eV, while the IPA calculation somewhat reduces the error to $0.3 - 0.5$ eV. Conversely, the averaged BSE curve reproduces correctly the charge transfer peak onset (while overestimating its intensity), while the IPA as usually overestimates both its transition energies and its intensity. Finally, the redshift between BSE and IPA amounts at $\sim 0.7 - 0.8$ eV on the onset.

Regarding the convergence, we note that a very high number of conduction and valence bands is required to obtain a converged spectra, which is hardly achievable in a standard BSE calculation and requires the averaging method.

We now move to the tentative attribution of the peaks through the study of the $NBANDSV$ convergence:

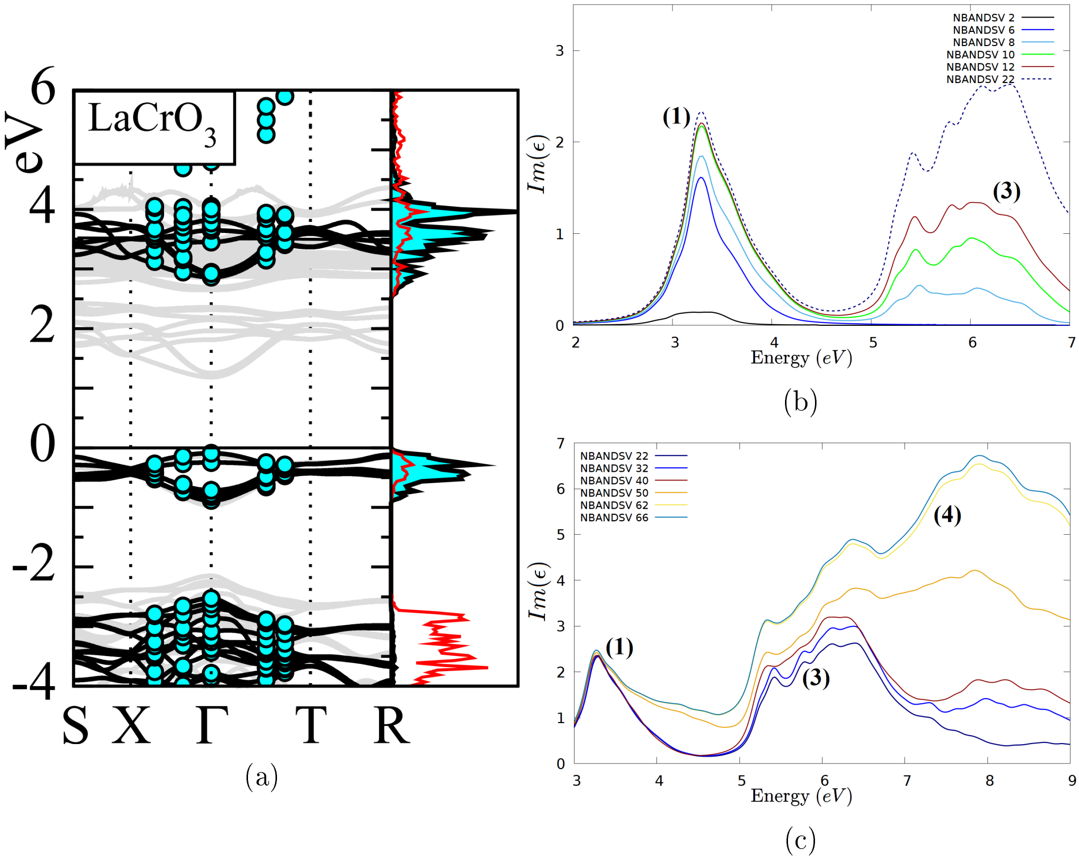

Figure 7.11: (a): bandstructure (taken from [99]), with the Density of States of $TM - d$(shadow, cyan line) and $O - p$ (full line, red).
(b),(c): Convergence with respect of the number of conduction band (with $NBANDSO$ = number of valence bands fixed).

The first peak (range $[3, 4]$ eV, feature (1) in figure 7.11b) is converged by $NBANDSV = 10$ and is mainly formed by transitions extending to the conduction bands between the *3-th* and *8-th*, which reside between 3.5 eV and 4.1 eV over the Fermi energy (at Γ). This structure is thus formed by transitions from the valence Mott subband near the Fermi energy (the levels at −3 eV are too low in energy to contribute) to these conduction bands.
Let's now draw a comparison between this Mott structure and the analogue ones in $LaTiO_3$ (figure 7.4b) and $LaVO_3$ (figure 7.7b). The peak is not split in two different features as in $LaVO_3$ and $LaTiO_3$ (the second feature is missing here). However, $LaCrO_3$'s single peak exhibits a characteristic typical of the second features of all other Mott insulators' spectra, namely the fact that the first two conduction bands give only a very limited contribution.

The second structure (which includes features (3) and (4)) is, as usual, determined by transitions involving two different groups of conduction bands. The first group includes transitions to bands from 7 to 22, and provides the main contribution to feature (3) of the charge transfer peak (see figure 7.11c). Bands from 7 to 10 have a main *Cr d* character and energy in the range $[3.7, 4.1]$ eV at Γ, while between the *11-th* and the *22-th* (lying in the energy window $[6.0, 6.7]$ eV) the *La f* character is dominant.
To complete the charge transfer structure (features (3) and (4)) and converge the spectra up to 9 eV we need however to include the bands between the *42-th* and the *62-th*. These bands have very strong *La d* character (with an average *Cr d* character of 17% at Γ) and reside in the energy range $[4.5, 6.9]$ eV at Γ[4].

The first 6 bands do not participate at all to these two features, as we can see from figure 7.11b; likewise transitions involving bands between the *22-th* and the *40-th* (with *La f* character and energy > 6.5 eV) contribute to this structure to a very limited extent (figure 7.11c).

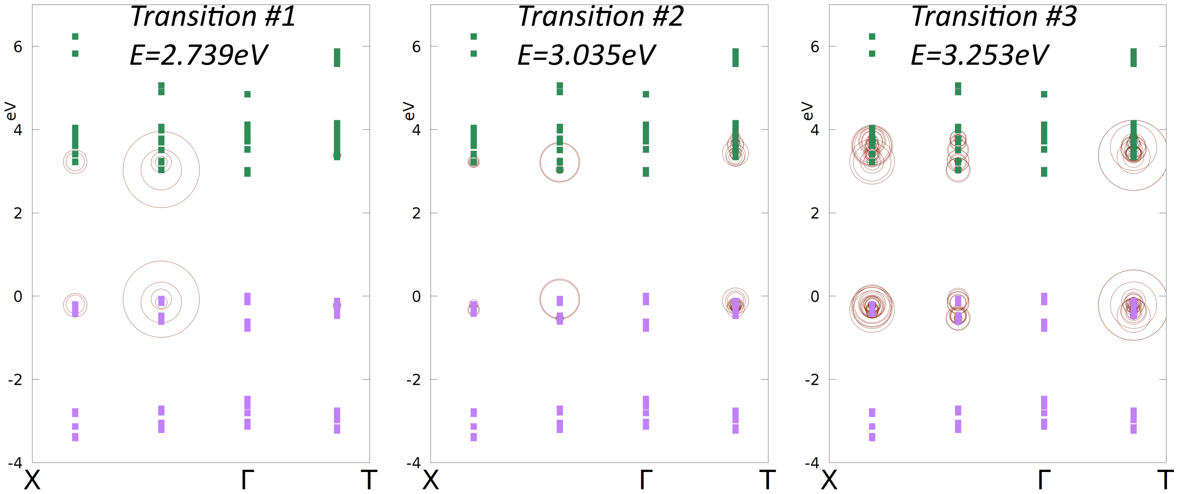

Figure 7.12: Plot of absolute value of the exciton wave function along high symmetry lines in reciprocal space. The circle radius is proportional to $|A^{\lambda}_{c,v,\vec{k}}|$. The transition's numbers refers to the label in figure 7.10b.

The excitonic wavefunctions (which are respectively the first transition with non-zero oscillator strength and two transitions related to the Mott peak) display a similar behavior to $LaTiO_3$'s ones. The first wavefunction is localized on the $\Gamma - X$ direction and, conversely, the second and third ones are strongly delocalized. As expected they are dominated by transitions between the two Mott subbands, without involving the valence bands formed by $O\ p$ states, thus validating the attribution of the first structure (feature (1) of figure 7.11b) to a Mott-type peak.

---

[4] With the exception of bands 43, 44, 45 which have energy in the range $[3.8, 4.2]$ eV.

$LaMnO_3$

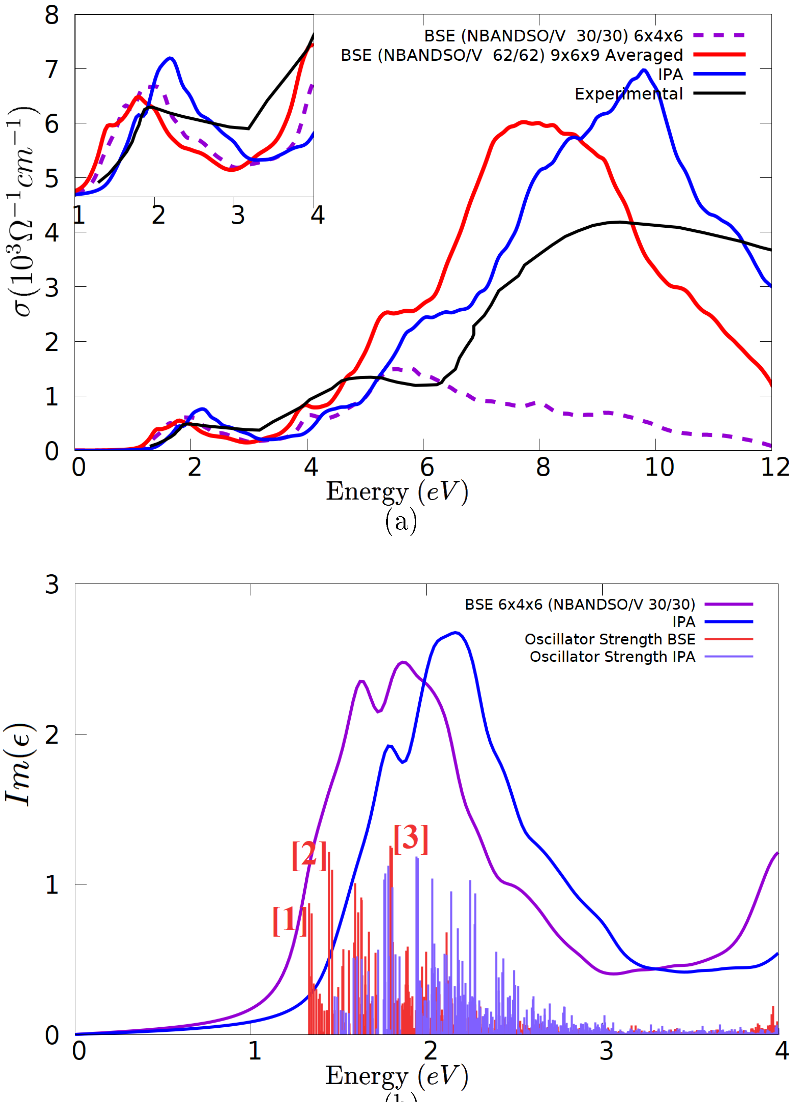

(a)

(b)

Figure 7.13: (a): Spatially averaged optical conductivity ($10^5\Omega^{-1}cm^{-1}$) of $LaMnO_3$, obtained with different approaches: in red through an averaged BSE on a $9 \times 6 \times 9$ mesh ($n \times n \times n = 3 \times 2 \times 3, m \times m \times m = 3 \times 3 \times 3$), in violet through an BSE on a $6 \times 6 \times 6$ mesh, in blue through a IPA on $G0W0$ QP-energies and $6 \times 4 \times 6$ mesh, while the black one is the experimental curve. (b): Zoom of the first structure (range $[0, 4]$ eV) of $\Im[\epsilon]$, with the associated oscillator strength.

$LaMnO_3$ spectra shows a quite different behavior with respect to the previous compounds: the IPA curve reproduces exactly the onset's position and slightly overestimates its intensity, while both BSE curves underestimate the experimental peak onset by ~ 0.4 eV, but reproduce correctly its height.
Conversely, the IPA calculation underestimates the second structure and the inclusion of the excitonic effects worsens its description.
Overall the lineshapes with and without excitonic effects exhibit a strong similarity, and the redshift amounts to ~ 0.3 eV on the onset and to $\sim 0.6 - 1.0$ eV for the second structure.

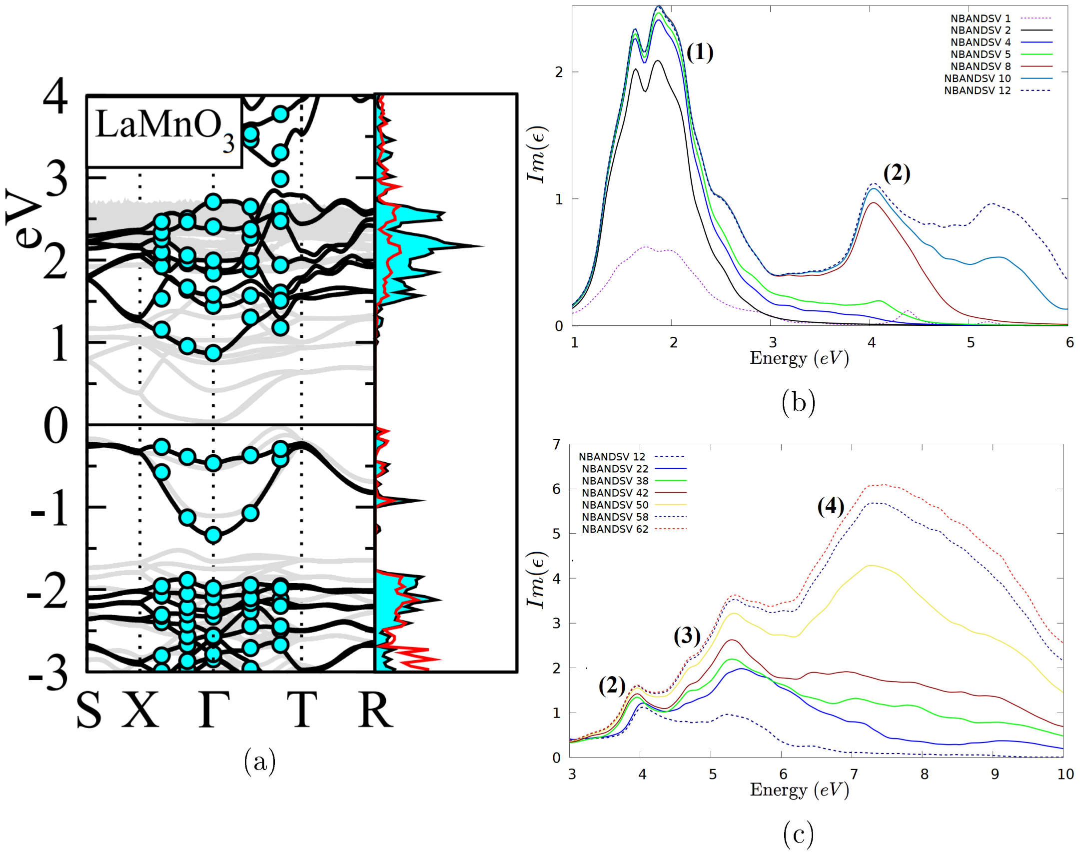

(a)

(b)

(c)

Figure 7.14: (a): bandstructure (taken from [99]), with the Density of States of $TM - d$(shadow, cyan line) and $O - p$ (full line, red).
(b),(c): Convergence with respect of the number of conduction band (with $NBANDSO$ = number of valence bands fixed).

The Mott peak (feature (1) in 7.14b) is completely determined by $NBANDSV = 4$: these bands have an $Mn\ d$ character and lie between 0.9 eV and 2.0 eV at Γ.
The onset of the second structure (feature 2) is mainly determined by the first 8 conduction bands, which have prevalent $Mn\ d$ character (over 75% at Γ) and complete the Mott subband visible in the density of states. The first two bands do not provide any contribution, a behaviour shared with $LaTiO_3$'s and $LaVO_3$'s similar features. However, unlike $LaTiO_3$'s and $LaVO_3$'s ones, this feature is not completely converged until the *50-th* band, as we can see from figure 7.14c.

The shoulder of the charge transfer peak (feature (3), range $[4.5, 6.0]$ eV) is established only by two different sets of bands. A first contribution is provided by transitions involving bands between the *8-th* and the *22-th*, dominated by $La\ f$ (and almost without any trace of $Mn\ d$ character) and lying between $[4.4, 6.4]$ eV over the Fermi energy (at Γ).
A second set of bands, from 38 to 62, is required to converge feature (3) and (4), i.e. the main charge transfer peak and its shoulder. These bands have a main $La\ d$ character (with a $Mn\ d$ percentage $< 10\%$) and energy between 3.1 eV and 6.3 eV (at Γ).

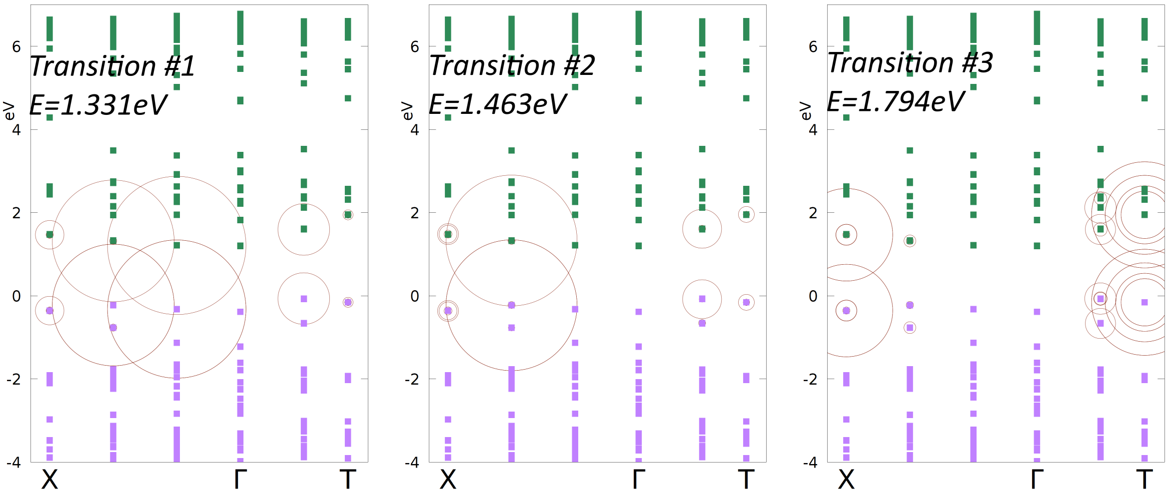

Figure 7.15: Plot of absolute value of the exciton wave function along high symmetry lines in reciprocal space. The circle radius is proportional to $|A^{\lambda}_{c,v,\vec{k}}|$. The transition's numbers refers to the label in figure 7.13b.

We now move to the analysis of the excitonic wavefunction. The one relative to the first eigenvalue with non zero oscillator strength (Transition #1 in figure 7.15) shows a very delocalized wavefunction, mainly along the $\Gamma - X$ direction but with significant magnitude also along the $\Gamma - T$ direction (and, interestingly, almost zero on Γ).
The second and third eigenvectors of figure 7.15 are associated to the Mott structure (feature (1) in 7.14b). This structure exhibits a double-peaked lineshape, and this peculiar lineshape cannot found explanation in the previous analysis (both the $NBANDSV = 1$ and $NBANDSV = 2$ curves in figure 7.14b exhibit this characteristic). To understand this structure we examine the wavefunctions associated to transitions belonging to each peak. The difference between the two wavefunctions is the direction of higher magnitude: the *2-nd* peaks along the $\Gamma - X$ direction, while the third one along $\Gamma - T$.

LaFeO$_3$

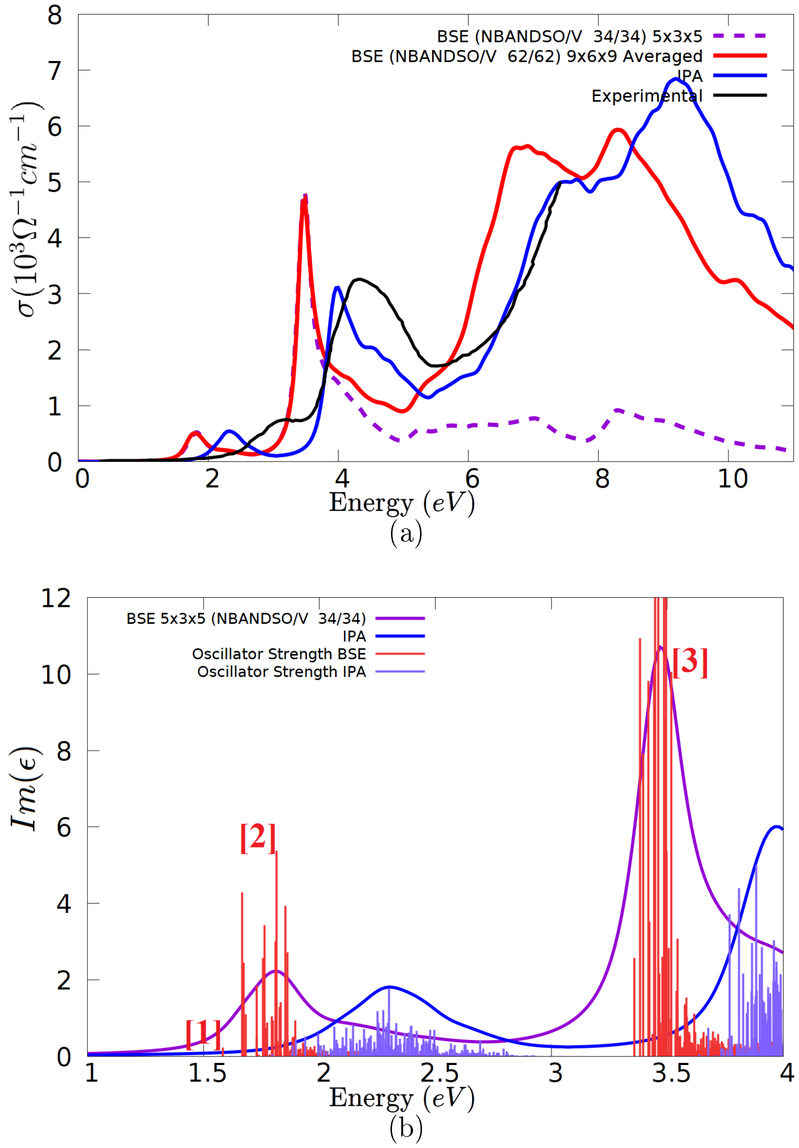

Figure 7.16: (a): Spatially averaged optical conductivity ($10^5\Omega^{-1}cm^{-1}$) of $LaFeO_3$, obtained with different approaches: in red through an averaged BSE on a $9 \times 6 \times 9$ mesh ($n \times n \times n = 3 \times 2 \times 3, m \times m \times m = 3 \times 3 \times 3$), in violet through an BSE on a $5 \times 3 \times 5$ mesh, in blue through a IPA on $G0W0$ QP-energies and $5 \times 3 \times 5$ mesh, while the black one is the experimental curve. (b): Zoom of the first structure (range $[1, 4]$ eV) of $\Im[\epsilon]$, with the associated oscillator strength.

$LaFeO_3$ spectra shows some similarity to $LaCrO_3$ one: both the BSE and IPA calculations underestimate the experimental onset (between $[2, 3]$ eV), and the introduction of excitonic effects worsens its description (the underestimation amounts at $0.8 - 1.0$ eV at the onset).
The spectra displays a second peak between the Mott onset and the charge transfer structure which represents a marked difference from the previous perovskites. The BSE calculations underestimate both this peak and the charge transfer structure by $0.6 - 0.8$ eV, while the IPA calculation correctly predicts their position and intensities.

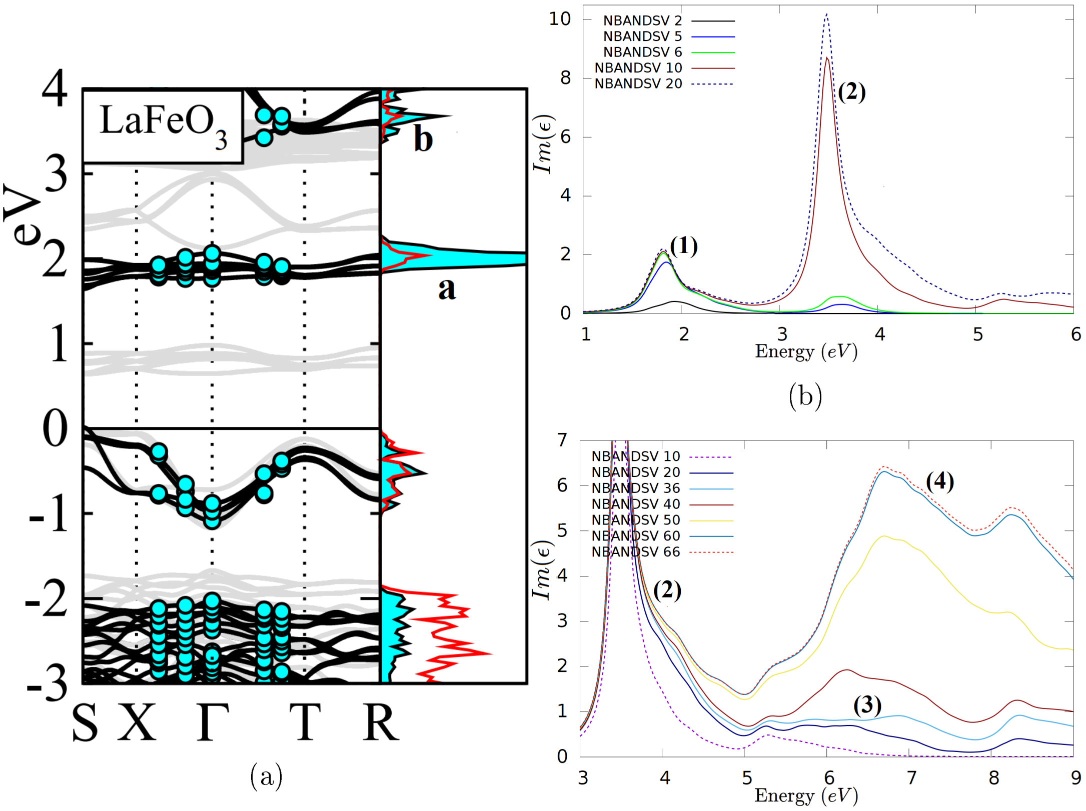

(a)

(b)

(c)

Figure 7.17: (a): bandstructure (taken from [99]), with the Density of States of $TM-d$(shadow, cyan line) and $O-p$ (full line, red).
(b),(c): Convergence with respect of the number of conduction band (with $NBANDSO =$ number of valence bands fixed).

We recognize in figure 7.17b the typical first feature which characterizes the lower part of the spectra of the other perovskite in the *La* series. The spectra onset (range [1.5, 2.0] eV, feature (1)) is determined completely by transitions to the first 6 conduction bands , which have dominant *Fe d* character and energy in the $[1.90, 2.25]$ eV range at Γ (feature *a* in the density of states). Given the energy position (transition energies) of the peak, and considering that the fundamental gap between the two Mott subbands is equal to 1.91 eV (see table 4.2), we validate its attribution as a Mott peak.
Transitions to these six conduction bands do not participate in shaping feature (2). This peaks is almost completely formed by transitions to conduction bands between the *8-th* and *10-th*: these bands have an average mixed character, $\sim 60\%$ *Fe d* and $\sim 25\%$ *La f* and energy in the $[3.5, 4.7]$ eV range. The peak's energy position, around 3.5 eV, allows us to conclude that this peak is formed by transitions between the valence Mott subband and the band group corresponding to the feature *b* in the density of states.
A marked difference between the other perovskites studied in this section is the very high intensity of the second peak (feature (2)).

While the first ten conduction bands do not contribute to the charge transfer structure (features (3) and (4)), the bands between the *11-th* and the *20-th* give a very limited contribution with respect to the previous materials; the main contribution is given by bands between the *36-th* and the *60-th*. The bands between the 11 and 39 have a dominating $La\ f$ character and reside in the region $[2.9, 7.5]$ eV at Γ(from the *11-th* and the *20-th* are located in the energy window $[2.9, 3.1]$ eV), while the orbitals from the *40-th* to the *60-th* lie in the range $[4.0, 7.3]$ eV and have $La\ d$ as main character.

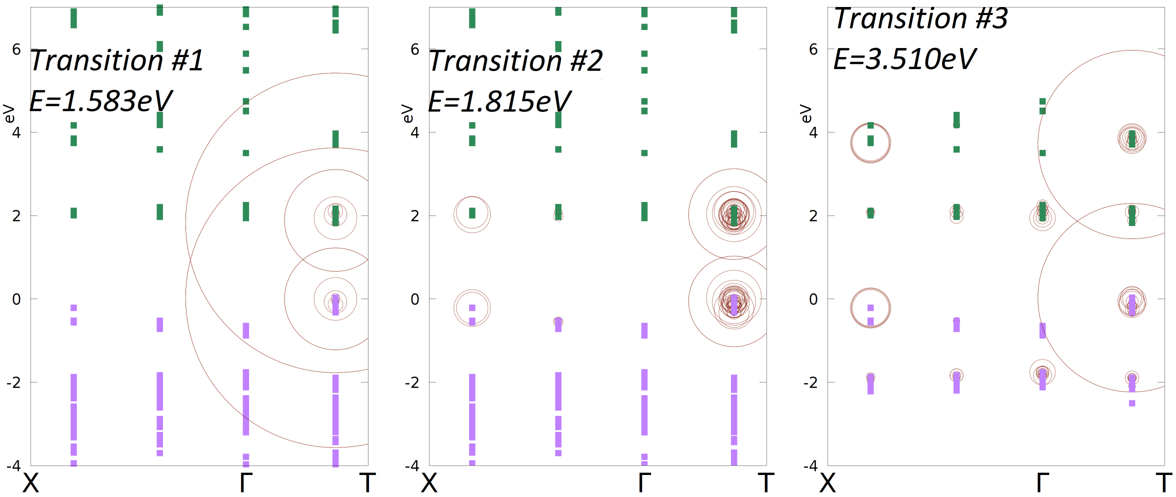

Figure 7.18: Plot of absolute value of the exciton wave function along high symmetry lines in reciprocal space. The circle radius is proportional to $|A^{\lambda}_{c,v,\vec{k}}|$. The transition's numbers refers to the label in figure 7.13b. The first two graph employed $NBANDSV/O = 34/34$, while the third used $NBANDSV/ == 10/10$.

Lastly, we study three excitonic wavefunctions associated to different transitions: the first wavefunction, as usual, is related to the first bright eigenvalue, the second to feature (1) and the third one to feature (2). The first two wavefunctions show a very coherent behavior: they involve only the Mott subbands closer to the Fermi energy. The third one, however, comprise transitions from the uppermost valence subband to conduction bands near 4 eV, confirming the previous exposition.
All three plots are strongly localized along the $\Gamma - T$ direction. All Mott insulators in this series exhibit a significant magnitude in this direction for the first Mott peak; however $LaTiO_3$, $LaCrO_3$ and $LaMnO_3$ share a strong contribution along the $\Gamma - X$ direction which is absent for $LaFeO_3$ and $LaVO_3$.

7.3 $SrMnO_3$, $4d$ and $5d$ TM perovskites

SrMnO$_3$

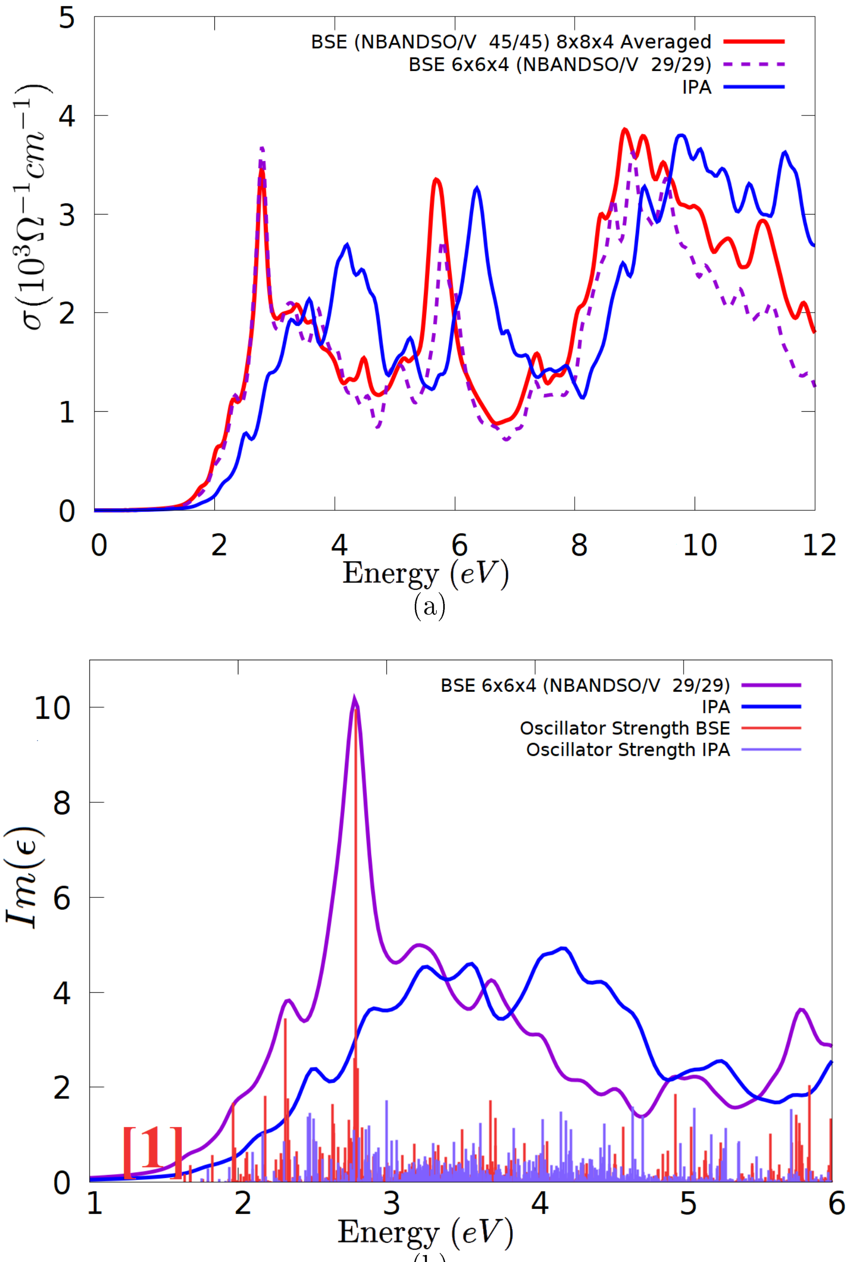

(a)

(b)

Figure 7.19: (a): Spatially averaged optical conductivity $(10^3\Omega^{-1}cm^{-1})$ of $SrMnO_3$, obtained with different approaches: in red through an averaged BSE on a $8 \times 8 \times 4$ mesh $(n \times n \times n = 4 \times 4 \times 2, m \times m \times m = 2 \times 2 \times 2)$, in violet through an BSE on a $6 \times 6 \times 4$ mesh, in blue through a IPA on $G0W0$ QP-energies and $6 \times 6 \times 4$ mesh. We could not find any experimental reports in literature. (b): Zoom on the range $[1, 6]$ eV of $\Im[\epsilon]$, with the associated oscillator strength.

Before starting to analyze the spectra, we briefly discuss the kpoint convergence: the two BSE curves in figure 7.19a superpose almost completely on first part of the graph (range $[0, 5]$ eV) and possess overall very similar features. Thus, an $8 \times 8 \times 4$ mesh was deemed adequate.

$SrMnO_3$'s BSE spectra exhibits a first structure at $[2, 4]$ eV, a second smaller peak at 6 eV and a larger structure at $[8, 11]$ eV. The BSE curve shows a marked redshift with respect to the IPA curve.

The excitonic effects on the first structure are quite relevant: the first peak is more intense (almost double height), the peak's shape is modified (a spectral weight transfer is present) and a noticeable redshift is visible in the transition energies (equal to $0.5 - 0.6$ eV).

The features at higher energies however maintain similar shapes and intensities, and are only redshifted. Similarly, the oscillator strengths are redshifted from the IPA one and display few very bright transitions in correspondence of the peaks.

We now discuss the $NBANDSV$ convergence, displayed in figure 7.20:

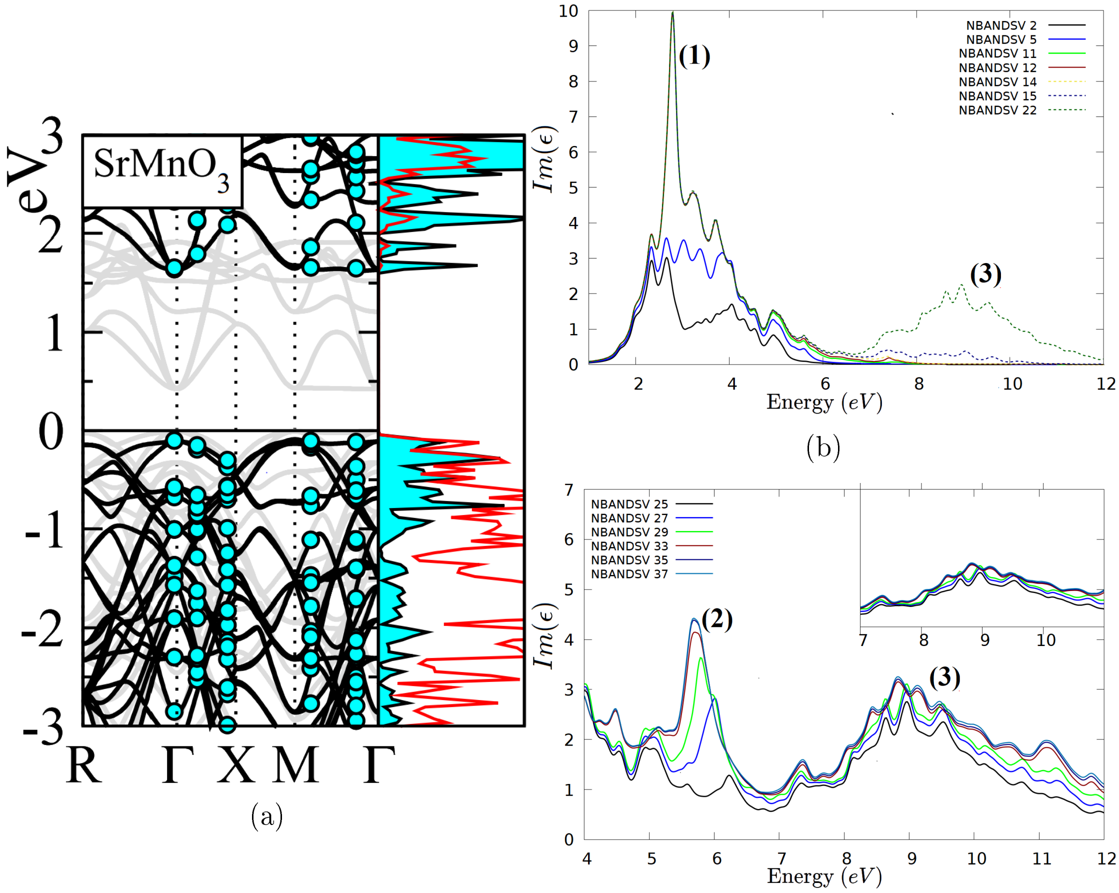

(a)

(b)

(c)

Figure 7.20: (a): bandstructure (taken from [99]), with the Density of States of $TM - d$(shadow, cyan line) and $O - p$ (full line, red).
(b),(c): Convergence with respect of the number of conduction band (with $NBANDSO$, number of valence bands, fixed).

The first peak (feature (1)) is completely described by $NBANDSV = 11$, which includes the transitions to conduction $Mn - 3d$ states between 1.6 eV and 3.0 eV over the Fermi energy (at Γ).

The second structure (range $[7, 12]$ eV, feature (3)) is completely missed until $NBANDSV = 14$ and starts to be described only by $NBANDSV = 15$ (see figure 7.20b); it's completely converged only by $NBANDSV = 33$ (see figure 7.20c). Hence this second

structure is defined by transitions between the *15-th* and the *33-th* conduction bands, corresponding to the *Sr 4d* and *6s* states lying between 6.2 eV and 11.1 eV over the Fermi energy at Γ (states not shown in figure 7.20a).
The peak between $[5, 7]$ eV (feature (2)) is the last to be described, involving transitions up to conduction bands 35 (thus including both $Mn - 3d$ states between 1.6 eV and 3.0 eV and *Sr 4d* and *6s* states lying between 6.2 eV and 11.1 eV).

From figure 7.19b we can see that a single very bright transition gives the dominant contribution to the first peak; it would interesting to understand which valence bands are involved. While the preferential method would be the direct investigation of the BSE eigenvector, in this particular case it's not possible due to computational limitation[5]. To gain a qualitative understanding we executed a series of calculations with a limited number of valence bands, see figure 7.21. The first 8 valence bands include states with energies (at Γ) from the Fermi energy down to 0.8 eV under the Fermi level: states that are strongly hybridized between $O - p$ and $Mn - d$ (see figure 7.20a and [99, p. 91]).

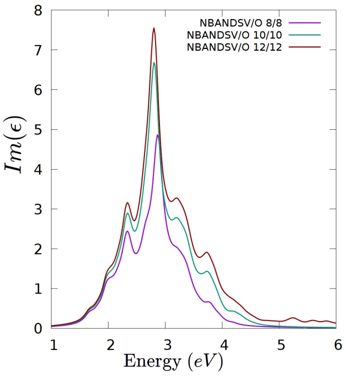

Figure 7.21: Convergence of the first structure with respect of the number of valence band.

Lastly we inspect (in figure 7.22) the excitonic eigenvector associated to the first eigenvalue with non-zero oscillator strength. All the relevant electron-hole pairs in the eigenvector involve the lowest unoccupied band (higher band give almost no contribution); however they comprise not only the highest occupied band but the first 7 valence band, which are strongly hybridized between $O - p$ and $Mn - d$, as said before. Interestingly, the wavefunction is strongly delocalized, with the major contribution coming from the $\Gamma - R$ direction and the strongest one at R.

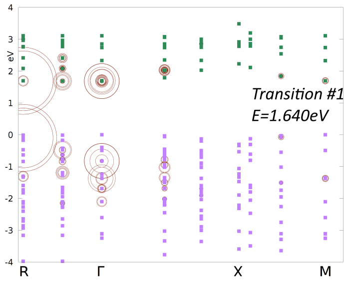

Figure 7.22: Plot of absolute value of the exciton wave function along high symmetry lines in reciprocal space. The circle radius is proportional to $|A^{\lambda}_{c,v,\vec{k}}|$. The transition's numbers refers to the label in figure 7.19b.

---

[5] The current $VASP$ implementation cannot provide in output an arbitrary eigenvector, but only every eigenvector from the first to the desired one; in other words, the output file must start from the first eigenvector and continue in order. The very bright transition corresponds to the *4673*-th and *4674*-th degenerate BSE eigenvalues; but a file with 4674 eigenvectors would require more than 100$GByte$, making its parsing exceedingly cumbersome.

Ca_2RuO_4

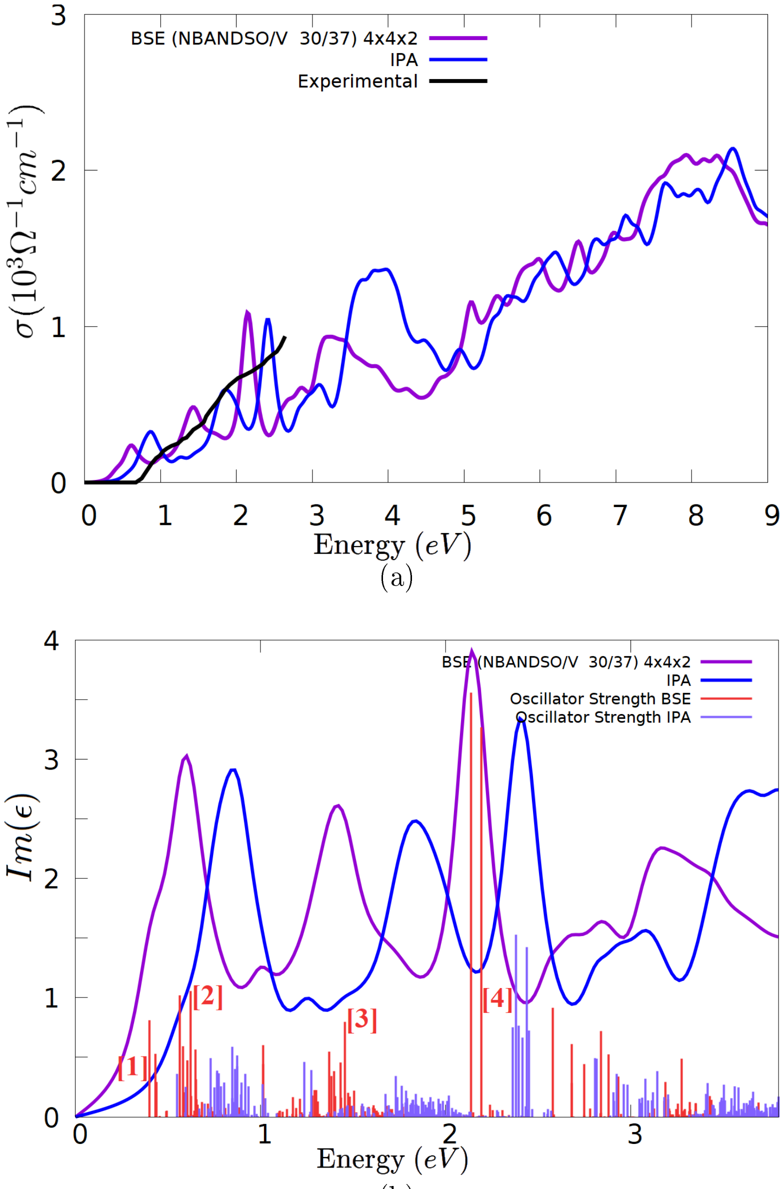

(a)

(b)

Figure 7.23: (a):Spatially averaged optical conductivity $(10^3\Omega^{-1}cm^{-1})$ of Ca_2RuO_4, obtained with different approaches: in violet through an BSE, in blue through a IPA on $G0W0$ QP-energies. Both calculations used a $4 \times 4 \times 2$ mesh (b): Zoom on the range $[0, 3.8]$ eV of $\Im[\epsilon]$, with the associated oscillator strength.

Ca_2RuO_4 is characterized by 4 different peaks inside the range $[0, 5]$ eV, the third one being the most intense; these peaks can be recognized more easily from the dielectric function graph (figure 7.23b). Interestingly, the BSE curve presents only a slight redshift from the IPA one (~ 0.15 eV at the onset) and very similar structures for what regard the lineshapes and the intensities. This result is essentially in line with a previous work from *Jung et.al*[122].

However, both IPA and BSE curves show only a *partial* agreement with the experimental curve: the IPA curve underestimates the onset by ~ 0.2 eV and the BSE curve, being redshifted with respect to the IPA one, accentuates this discrepancy (to ~ 0.4 eV).

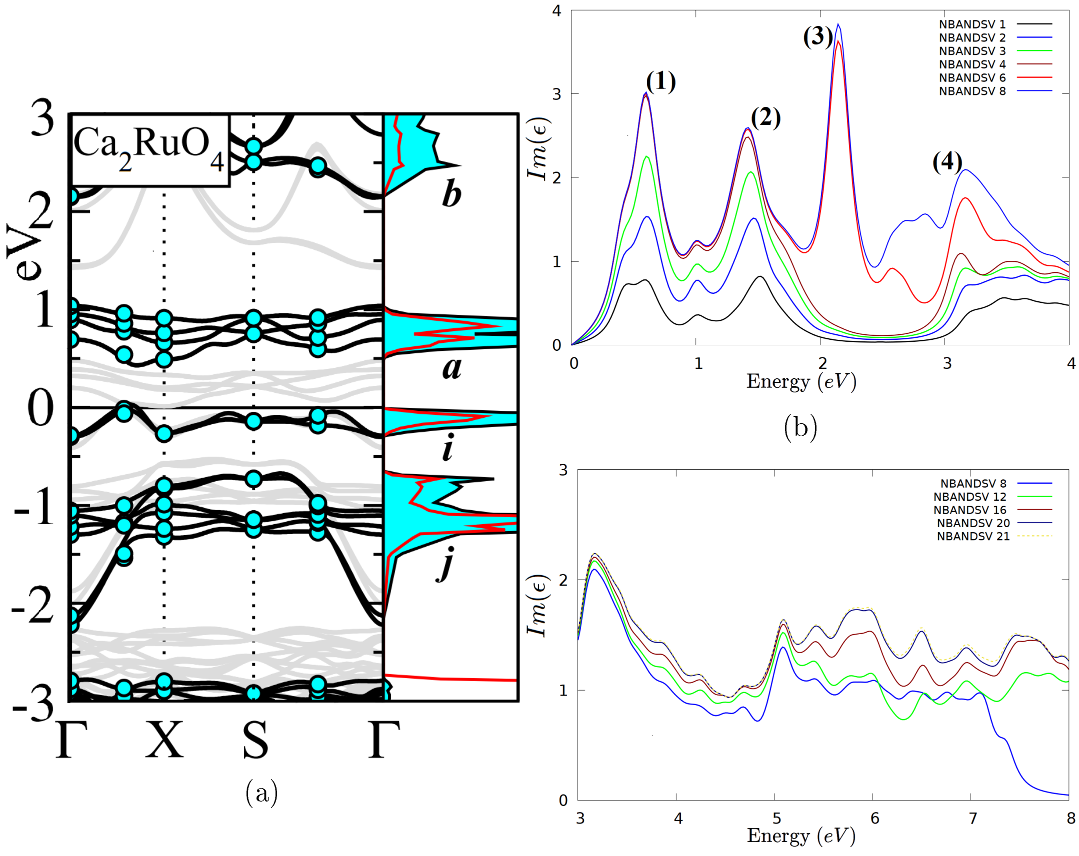

(a)

(b)

(c)

Figure 7.24: (a): bandstructure (taken from [99]), with the Density of States of $TM - d$(shadow, cyan line) and $O - p$ (full line, red).
(b),(c): Convergence with respect of the number of conduction band (with $NBANDSO$ = number of valence bands fixed).

The picture emerging from figure 7.24 essentially confirms the peaks attribution made by *Zeynep et.al*[99] and *Jung et.al*[122]. The first peak (range $[0, 1]$ eV, feature (1)) is determined by transitions to the first 4 conduction bands. These bands are dominated prevalently by $Ru - d$ states (feature a in the density of states), and thus (given the peak's position < 1 eV) can be associated only to $i \rightarrow a$ transitions.
The second peak (range $[1, 2]$ eV, feature (2)) is completely converged by conduction band 6, which gives also the dominant contribution to the third peak (feature (3)); band 5 and 6 are the first two bands associated with the b structure inside the DOS. To converge the third and fourth peak is however necessary to include band 7 and 8, which complete the b structure inside the DOS (the b structure is primarily constituted by $Ru - d$ states too).
The structure in the range $[4, 8]$ eV requires the first 20 conduction bands to be described correctly. The $10 - th$ and $11 - th$ conduction bands are also primarily associated to $Ru - d$ states, while the bands from 12 to 20, lying from 4.2 eV to 5.6 eV at Γ, have $Ca - d$ character.

We now analyze (in figure 7.25) the excitonic eigenvectors relative to the first non-zero oscillator strength (transition #1 in figure 7.25) and to features (1), (2) and (3) of figure 7.24b:

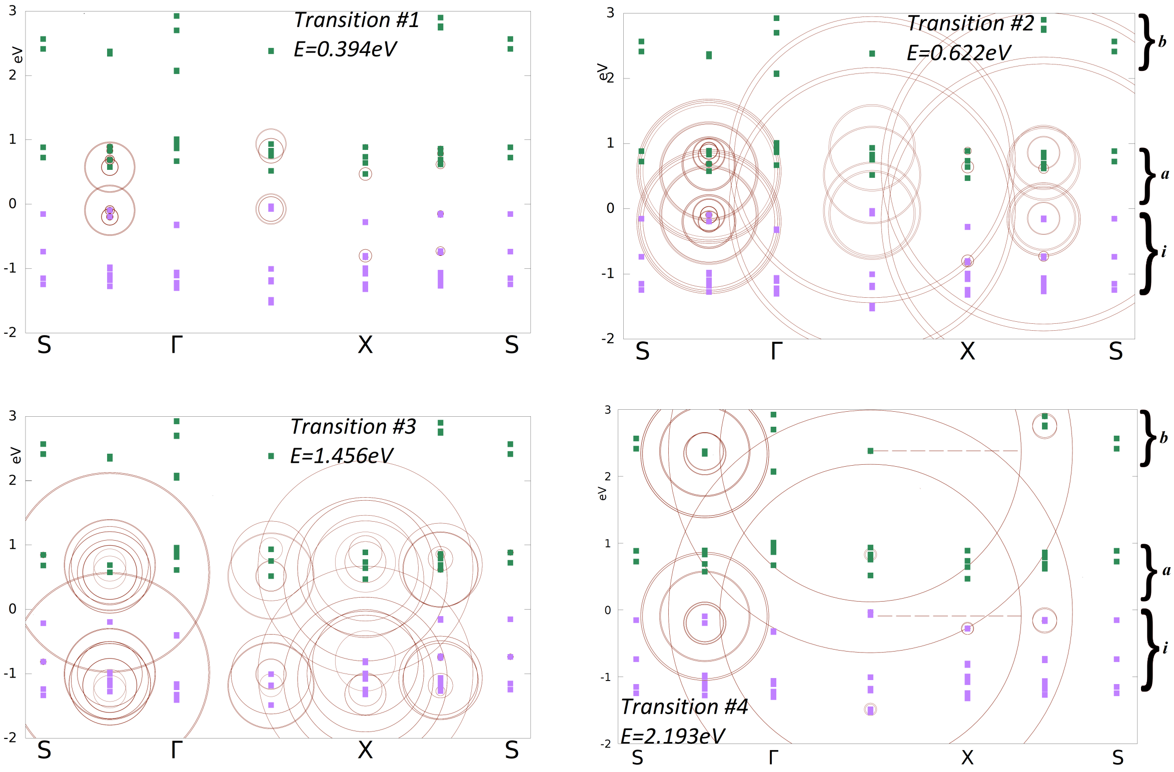

Figure 7.25: Plot of absolute value of the exciton wave function along high symmetry lines in reciprocal space. The circle radius is proportional to $|A^{\lambda}_{c,v,\vec{k}}|$. The transition's numbers refers to the label in figure 7.23.

All eigenvectors are very delocalized and, interestingly, there are no relevant contribution at Γ. The first two wavefunctions, related to the first peak, are associated to transitions $i \rightarrow a$ (where i and a are structures in the density of states, see figure 7.24a). On the contrary the brightest transition belonging to the second peak (#3) involves the j and a structures ($j \rightarrow a$), and the last wavefunction describes a $i \rightarrow b$ transition, in agreement with the previous discussion.

SrTcO$_3$

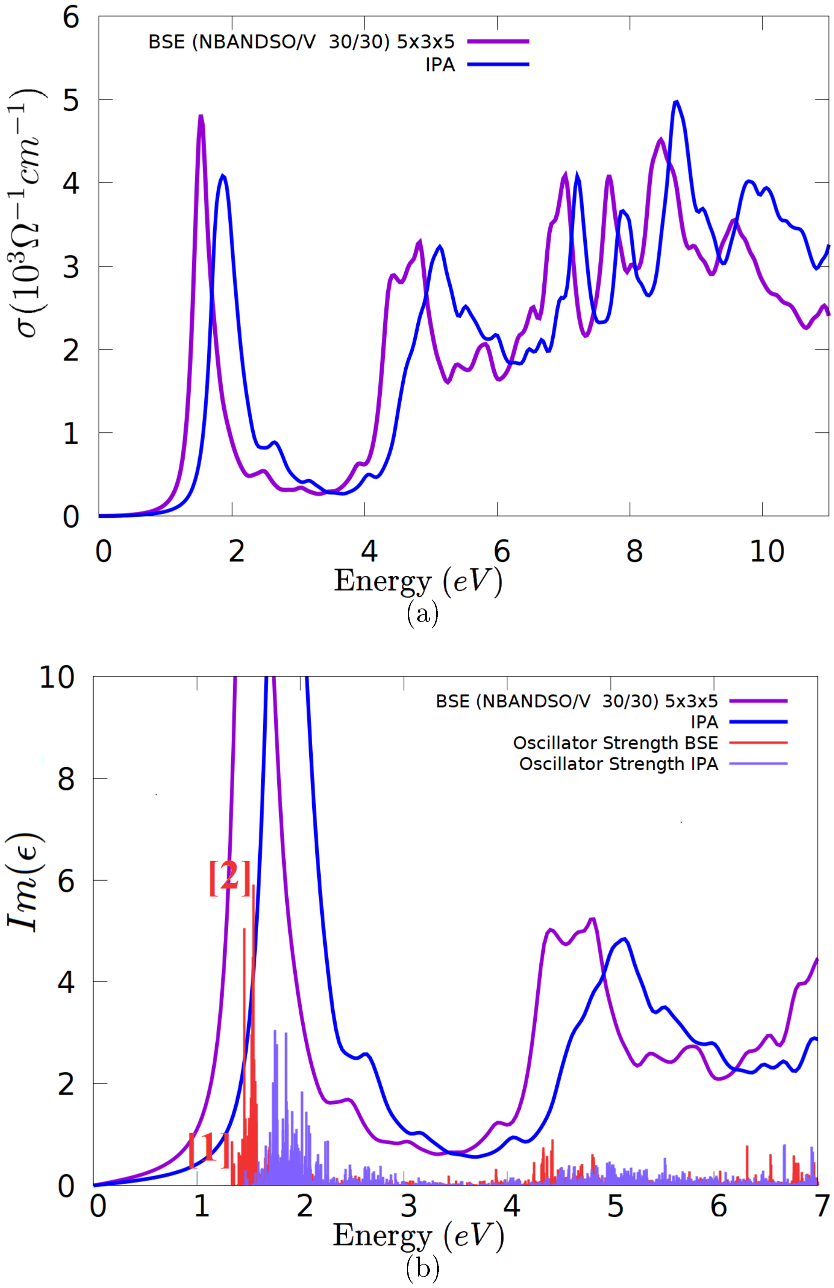

Figure 7.26: (a): Spatially averaged optical conductivity ($10^3\Omega^{-1}cm^{-1}$) of $SrTcO_3$, obtained with different approaches: in violet through an BSE on a $5 \times 3 \times 5$ mesh, in blue through a IPA on $G0W0$ QP-energies and the same mesh. We could not find any experimental reports in literature.(b): Zoom of the first two structures (range $[0, 7]$ eV) of $\Im[\epsilon]$, with the associated oscillator strength.

$SrTcO_3$ spectra shows a very intense peak near 2 eV and a series of less high peaks in the range $[4, 10]$ eV. The BSE and IPA curves display a very similar shape, without marked differences apart from the usual redshift, also visible in the oscillation strengths in figure 7.26. While in $SrMnO_3$ the inclusion of excitonic effects gives rise to a very intense peak (figure 7.19), here the peak between $[1, 2]$ eV is only marginally enhanced and shifted by ~ 0.3 eV.

We now analyze, as usual, the $NBANDSV$ convergence in figure 7.27:

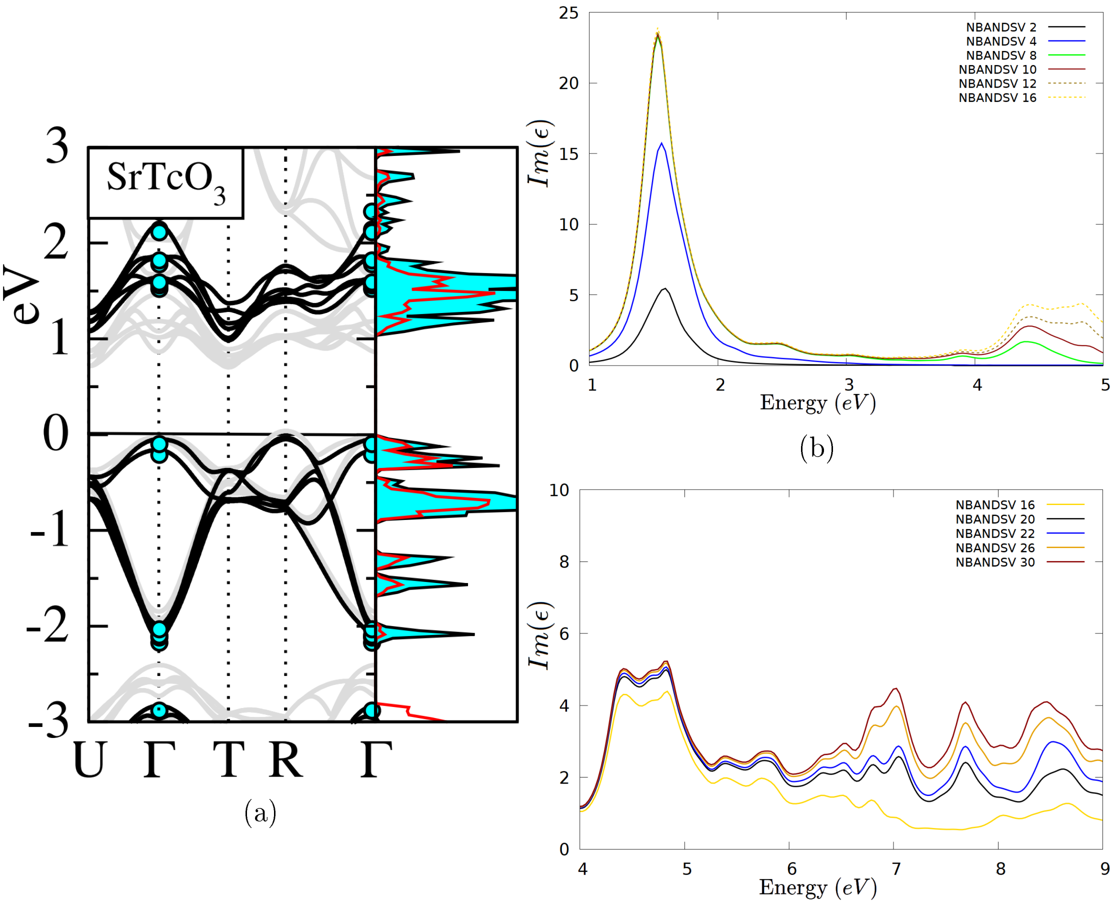

(a)

(b)

(c)

Figure 7.27: (a): bandstructure (taken from [99]), with the Density of States of $TM-d$(shadow, cyan line) and $O-p$ (full line, red).
(b),(c): Convergence with respect of the number of conduction band (with $NBANDSO$, number of valence bands, fixed).

The structure between $[1, 2]$ eV requires the first 8 conduction bands to be completely converged, although a significant contribution originates from transitions involving the first 4 conduction bands. These eight bands, between 1.6 eV and 2.4 eV (at Γ) over the Fermi energy, are dominated by Tc d states.
The second, smaller, peak at $[4, 6]$ eV is not described by the first four bands and receives the major contribution from transitions to conduction bands $8-16$, lying between 2.4 eV and 5.5 eV (at Γ) over the Fermi energy (not showed in figure 7.27a). The *8-th*, *9-th* and *10-th* conduction bands exhibit a predominant Tc d character, while the ones from the *11-th* to the *16-th* display a strong Sr d character (with the exception of the *14-th*, which still retains a strong Tc character and is weakly hybridized with O p states).
Only the spectra segment > 6 eV receives contribution from transitions involving bands over the $22-th$.

We now display (in figure 7.28) the excitonic wavefunctions associated to the first transition with non-zero oscillator strength and to the first peak.

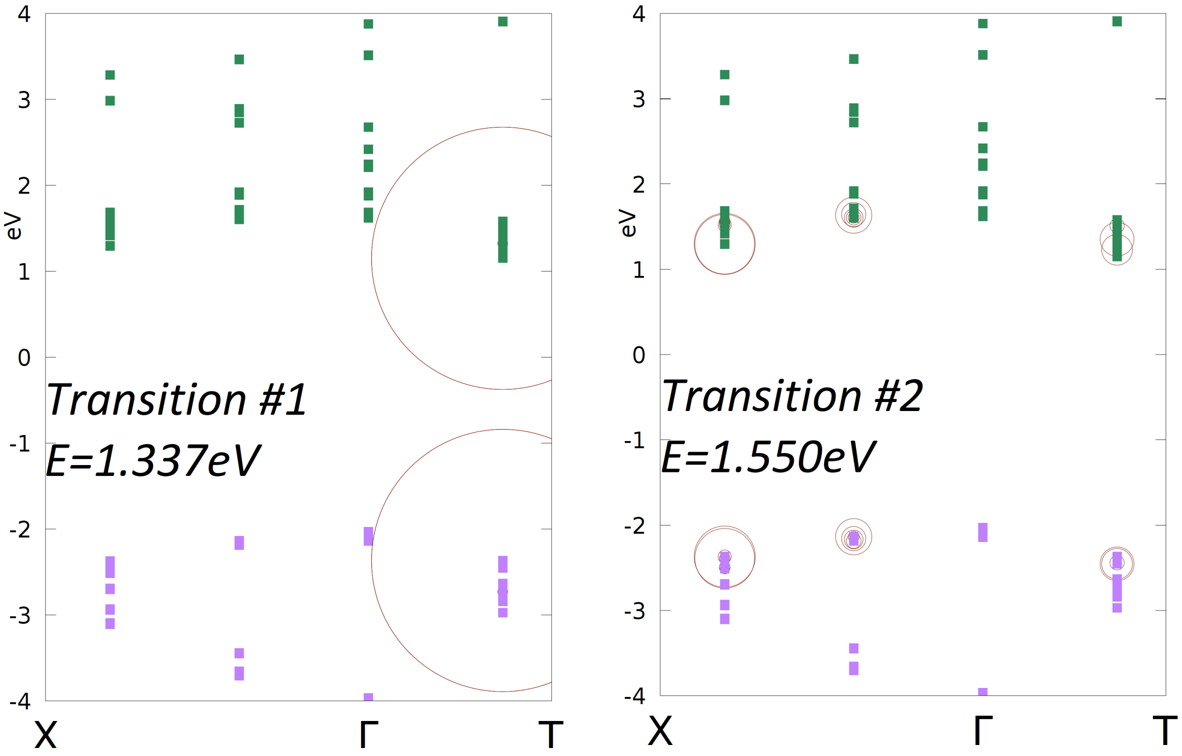

Figure 7.28: Plot of absolute value of the exciton wave function along high symmetry lines in reciprocal space. The circle radius is proportional to $|A^{\lambda}_{c,v,\vec{k}}|$. The transition's numbers refers to the label in figure 7.26b.

In the first figure (transition #1) the only strong contribution came from kpoints near the $\Gamma - T$ direction, and involves bands with predominant $Tc\,d$ character; in the second one the eigenvector is much more delocalized, and exhibits no contribution at Γ.

NaOsO$_3$

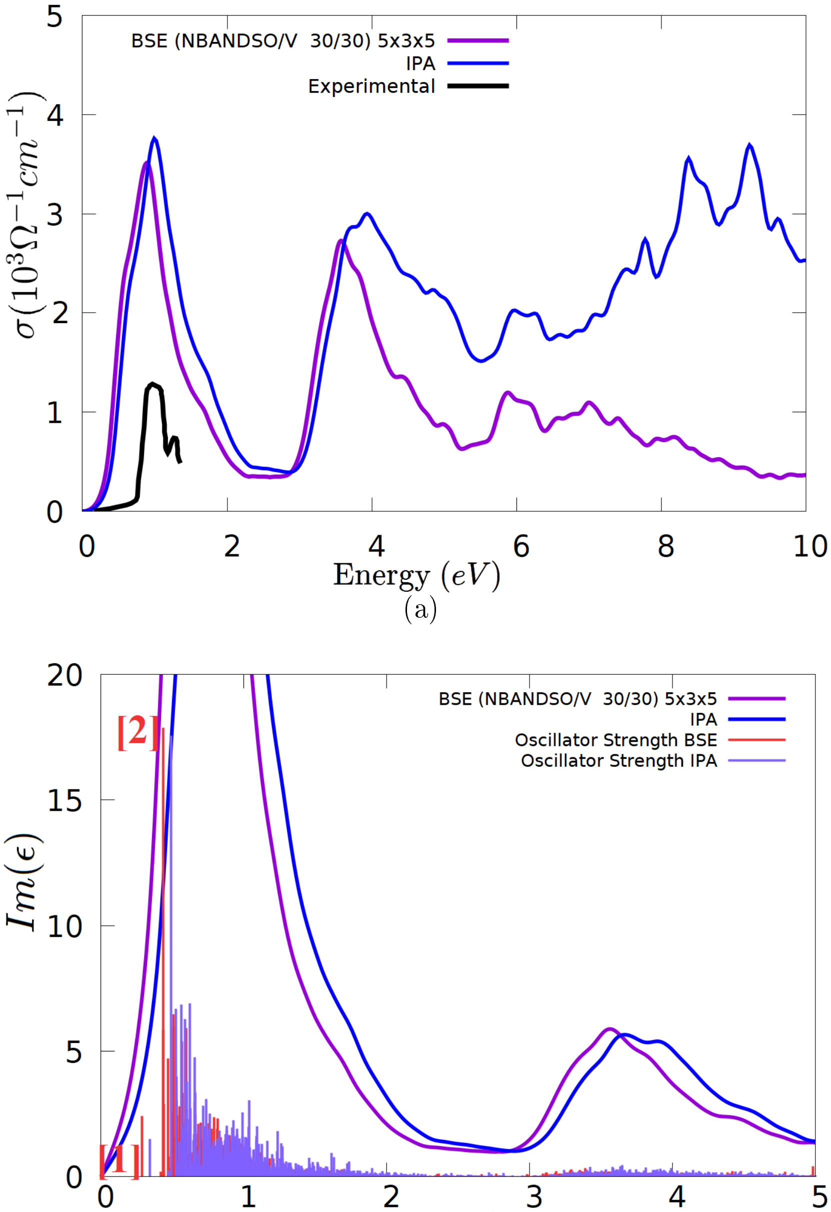

(a)

(b)

Figure 7.29: (a): Spatially averaged optical conductivity $(10^3\Omega^{-1}cm^{-1})$ of $NaOsO_3$, obtained with different approaches: in violet through an BSE, in blue through a IPA on $G0W0$ QP-energies- Both calculations used a $5 \times 3 \times 5$ mesh. (b): Zoom of the first two structures (range $[0, 5]$ eV) of $\Im[\epsilon]$, with the associated oscillator strength.

$NaOsO_3$ spectra is characterized by a very intense and large peak between $[0, 2]$ eV (as we can see from figure 7.29, the oscillator strengths associated to this peak span almost 1 eV for both curves) and a second peak with a large shoulder starting from 3 eV. The excitonic effects modify only in a very weak manner the IPA spectra: the BSE's oscillator strength redshift is much less pronounced than $SrTcO_3$ one ($\sim$ 0.1 eV for the first peak), and the lineshape variation is less conspicuous.

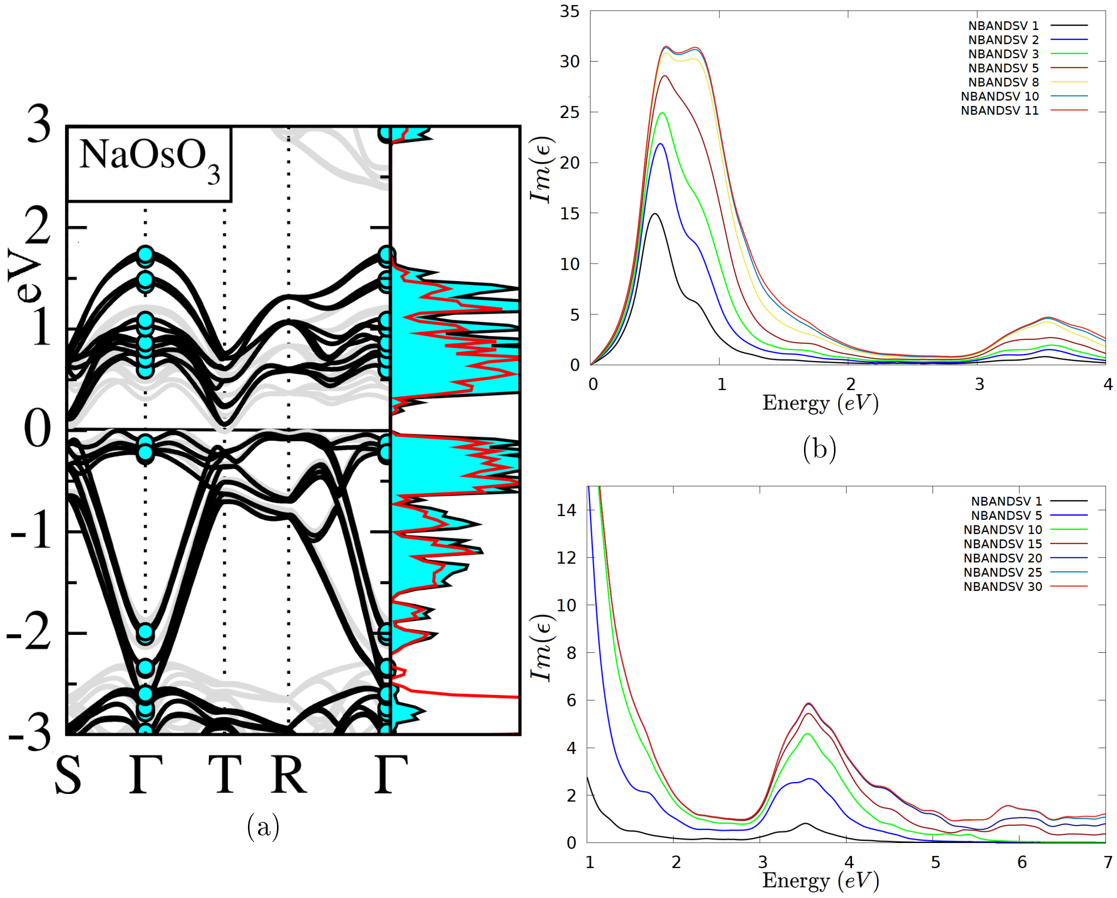

(a)

(b)

(c)

Figure 7.30: (a): bandstructure (taken from [99]), with the Density of States of $TM - d$(shadow, cyan line) and $O - p$ (full line, red).
(b),(c): Convergence with respect of the number of conduction band (with $NBANDSO$, number of valence bands, fixed).

As we can see from figure 7.30b the first peak is mostly determined by transitions involving the first five conductions bands ($NBANDSV = 5$, dark red line), located between 0.5 eV and 0.8 eV over the Fermi energy at Γ. However it's completed only by the $10 - th$ conduction band, which includes bands up to 1.4 eV. These first ten bands are primarily associated to $Os - d$ t_{2g} levels (even though they possess also sizable components of $O - p$ and $Os - d$ d_{z^2} states).
Transitions to the first 10 bands provide also an important contribution to the peak between $[2, 4]$ eV, which requires up to conduction bands 25 (corresponding to 4.9 eV over the Fermi level) to be converged. These bands between the *11-th* and the *25-th* have a prevalent Os d character.

We now study (in figure 7.31)the excitonic wavefunction (or, specifically, its absolute value $|A^{\lambda}_{c,v,\vec{k}}|$) for some specific transitions:

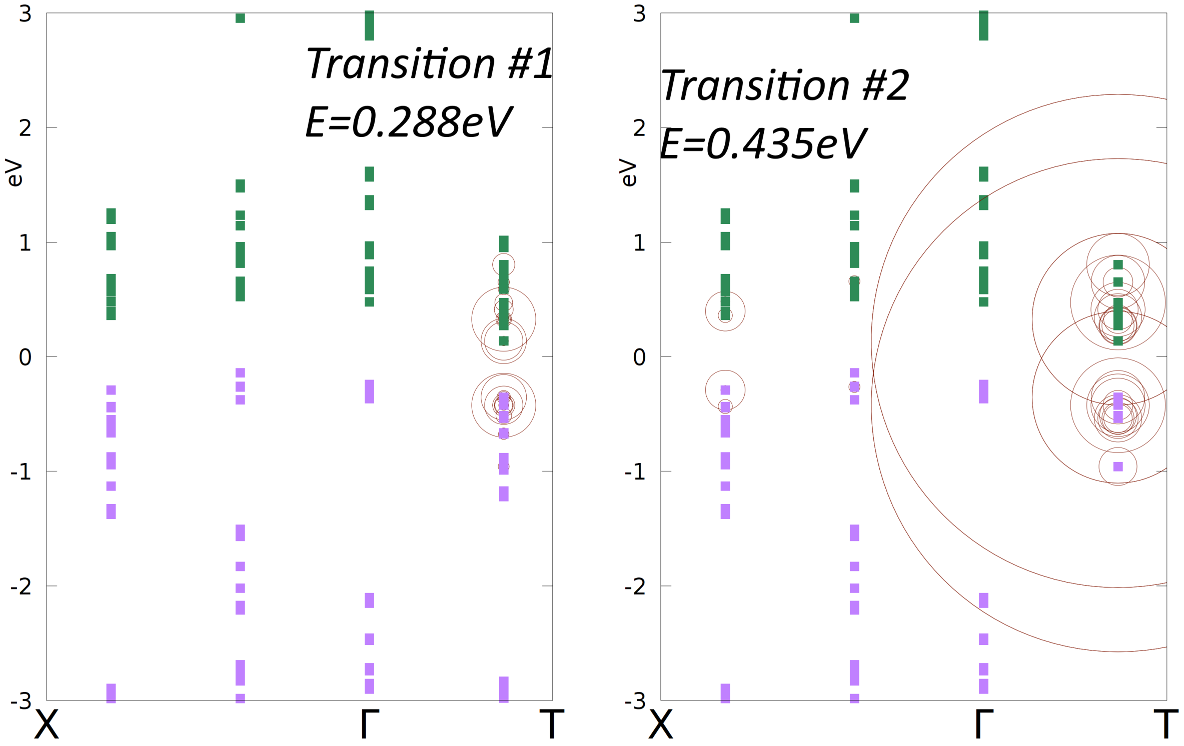

Figure 7.31: Plot of absolute value of the exciton wave function along high symmetry lines in reciprocal space. The circle radius is proportional to $|A^{\lambda}_{c,v,\vec{k}}|$. The transition's numbers refers to the label in figure 7.29.

The first picture displayed in figure 7.31 corresponds to the first transition with non-zero oscillator strength; it exhibits localized contributions in the $\Gamma - T$ direction. The second transition is associated with the very bright peak at 1 eV (see figure 7.29b). This wavefunction attains significant weight not only on the highest valence band and lowest conduction band, but from all bands (in the $\Gamma - T$ direction) inside the energy range $[-1, 1]$ eV.

Chapter 8

Conclusions and Outlooks

The main focus of this thesis was the computational study of the optical spectra of a selected set of Transition metal Oxide perovskites with state-of-art methodologies implemented in the software $VASP$ (*Vienna Ab-Initio Simulation Package*).
The set was chosen in order to constitute a minimal dataset representative of the variety of properties and characteristic of this class of materials: magnetic and non-magnetic systems, with and without structural distortions, with different spatial extensions ($n = 3, 4, 5$ with $n =$ *main quantum number*) and occupancies of the outermost d states ($d^0 \rightarrow d^5$). The bandgaps cover a range from 0.1 eV ($NaOsO_3$) to 6.1 eV ($SrHfO_3$), and the spectra exhibit different types of main optical excitations (Mott-Hubbard, Charge-Transfer and band insulators).
A previous study of the same dataset was performed by *Ergönenc et.al*[99] employing the $G0W0$ method, which allowed the authors to evaluate the bandgaps with good precision; the spectra however have been evaluated only in the Indipendent Particle Approximation using as a starting point a PBE (GGA) calculation. An important question left open by this work is hence the effect of electron-hole interaction on the perovskites' optical conductivity spectra.
The inclusion of the electron-hole interaction beyond the IPA (through the Bethe-Salpeter equation), which is the focus of this thesis, modifies the IPA spectra in two main ways: the first one involves an almost uniform redshift of the entire spectra, while the second one is associated to a lineshape change, in the form of a shift to lower energies of a feature's spectral weight or in the development of very bright peaks at the onset. We can therefore summarize the result inside this framework:

- The first four materials of the dataset (see chapter 6.4), the band insulators $KTaO_3$, $SrTiO_3$, $SrZrO_3$ and $SrHfO_3$, exhibit a pronounced redshift and spectral weight transfer to lower energies, in particular for the first structure inside the spectra. The agreement is overall good on the onset and less satisfactory for the second structures of the spectra.
  We discussed in Chapter 6.5 that the remaining discrepancies can be strongly reduced by employing a different starting point (i.e. a hybrid $HSE06$ calculation instead of a standard DFT one) which guarantees a better description of the localized d states and hence allows to reach a very good agreement with the experimental data.
  Finally we examined the attribution of the spectra's peaks to specific transitions between bands. With a broad generalization, the first structure derives from transition from O p states to the transition metals' t_{2g} ones, while the second

structure involves mainly transitions to the transition metals' or $Sr\ e_g$ states.

- The second subset (see chapter 7.2) comprises the six perovskites in the La Series, which display a spectra redshift between 0.3 eV and 0.8 eV on the onset. However they don't exhibit any relevant changes in the lineshapes and don't display the development of new peaks or features (even at the onset).
  Regarding the comparison with the experimental data, the structures are correctly identified (with overall similar shapes) and the transitions attributions confirm the results of previous experimental works[120, 121]. The Mott peaks' transition energies however are consistently underestimated by $0.4 - 1.0$ eV (with $LaTiO_3$ as only exception). On the contrary, the agreement of the Charge-Transfer peaks does not show a general trend, shared by the compounds of this subset, and appears material dependent.

- The IPA and BSE comparisons in the last subset (comprising $SrMnO_3$, $SrTcO_3$, $NaOsO_3$ and Ca_2RuO_4 ; see chapter 7.3) show a similar behaviour with respect to the La series: The spectral weight transfers are small and the redshifts amount at $\sim 0.1 - 0.5$ eV, sign that the excitonic effects have a smaller impact with respect to the other subsets. For Ca_2RuO_4 and $NaOSO_3$ the agreement with the experimental data is not complete, and for $SrMnO_3$, $SrTcO_3$ no experimental reports in literature have been found.

Another important set of considerations, developed in chapters 6.1, 6.2 and 7.1, concerns the technical but crucial issue of the convergence of the BSE spectra.
In fact, as discussed in chapter 6.1, the assessment of the optical properties requires much denser kpoint meshes inside the Brillouin Zone than the corresponding ground state calculations. In turn (see chapter 7.1), the larger perovskites (comprising all the materials with more than 20 atoms inside the unit cell, i.e. the second and third subsets) require the inclusion of transitions between a large number of valence and conduction bands to appropriately converge the optical conductivity up to 10 eV. These considerations imply that a standard calculation with converged parameters would be infeasible due to time and memory requirements. To address this issue we used a different approach, employing a method based on the averaging of shifted-grid independent BSE calculations (described in chapter 6.3). This approach allowed us to reduce the computational load and divide it into more tractable calculations, while retaining spectra almost identical to the ones obtained with the standard BSE procedure.

Finally, the remaining discrepancies in the La series need to be addressed and investigated further. Moreover the remarkable results obtained in chapter 6.5, employing calculations with hybrid functionals as a starting point, are expected to be extended to all materials in the dataset: this will improve the overall quality of the spectra and may represent a possible way to address these discrepancies.

Bibliography

[1] D. R. Hartree and W. Hartree. Self-consistent field, with exchange, for Beryllium. *Proceedings of the Royal Society of London. Series A - Mathematical and Physical Sciences*, 150(869):9–33, 1935.

[2] D. R. Hartree. The wave mechanics of an atom with a non-coulomb central field. part II. some results and discussion. *Mathematical Proceedings of the Cambridge Philosophical Society*, 24(1):111–132, 1928.

[3] V. Fock. „selfconsistent field“ mit austausch für natrium. *Zeitschrift für Physik*, 62(11):795–805, Nov 1930.

[4] R.M. Martin, R.M. Martin, and Cambridge University Press. *Electronic Structure: Basic Theory and Practical Methods*. Cambridge University Press, 2004.

[5] G. Baym. *Lectures On Quantum Mechanics*. CRC Press, 1969.

[6] P. Hohenberg and W. Kohn. Inhomogeneous Electron Gas. *Phys. Rev.*, 136:B864–B871, Nov 1964.

[7] R.G. Parr and Y. Weitao. *Density-Functional Theory of Atoms and Molecules*. International Series of Monographs on Chemistry. Oxford University Press, 1994.

[8] H. Eschrig. *The fundamentals of density functional theory*. Teubner-Texte zur Physik. Teubner, 1996.

[9] R.M. Dreizler and J. da Providência. *Density Functional Methods In Physics*. Nato ASI Subseries B:. Springer US, 1985.

[10] M. Ferrario, G. Ciccotti, and K. Binder. *Computer Simulations in Condensed Matter: From Materials to Chemical Biology*. Number v. 1 in Lecture Notes in Physics. Springer Berlin Heidelberg, 2007.

[11] W. Kohn. Highlights of condensed-matter theory. proceedings of the international school of physics “Enrico Fermi”, course LXXXIX at Varenna on Lake Como, 28 June-16 July 1983. Hg. von F. Bassani, F. Fumi und M. P. Tosi. *Acta Polymerica*, 38(10):588–588, 1987.

[12] P. Blanchard and E. Bruening. *Mathematical Methods in Physics: Distributions, Hilbert Space Operators, and Variational Methods*. Progress in Mathematical Physics. Birkhäuser Boston, 2002.

[13] F. Bechstedt. *Many-Body Approach to Electronic Excitations: Concepts and Applications*. Springer Series in Solid-State Sciences. Springer Berlin Heidelberg, 2014.

[14] Mel Levy. Electron densities in search of Hamiltonians. *Phys. Rev. A*, 26:1200–1208, Sep 1982.

[15] E. Lieb. in Physics as Natural Philosophy, edited by A.Shymony and H.Feshbach. page 11, 1982.

[16] T. L. Gilbert. Hohenberg-Kohn theorem for nonlocal external potentials. *Phys. Rev. B*, 12:2111–2120, Sep 1975.

[17] U von Barth and L Hedin. A local exchange-correlation potential for the spin polarized case. *Journal of Physics C: Solid State Physics*, 5(13):1629–1642, Jul 1972.

[18] John P. Perdew and Yue Wang. Accurate and simple analytic representation of the electron-gas correlation energy. *Phys. Rev. B*, 45:13244–13249, Jun 1992.

[19] John P. Perdew, Kieron Burke, and Matthias Ernzerhof. Generalized Gradient Approximation Made Simple. *Phys. Rev. Lett.*, 78:1396–1396, Feb 1997.

[20] A. D. Becke. Density-functional exchange-energy approximation with correct asymptotic behavior. *Phys. Rev. A*, 38:3098–3100, Sep 1988.

[21] Chengteh Lee, Weitao Yang, and Robert G. Parr. Development of the Colle-Salvetti correlation-energy formula into a functional of the electron density. *Phys. Rev. B*, 37:785–789, Jan 1988.

[22] Jiangang He and Cesare Franchini. Assessing the performance of self-consistent hybrid functional for band gap calculation in oxide semiconductors. *Journal of Physics: Condensed Matter*, 29(45):454004, oct 2017.

[23] Peitao Liu, Cesare Franchini, Martijn Marsman, and Georg Kresse. Assessing model-dielectric-dependent hybrid functionals on the antiferromagnetic transition-metal monoxides MnO, FeO, CoO, and NiO. *arXiv e-prints*, Feb 2019.

[24] Aliaksandr V. Krukau, Oleg A. Vydrov, Artur F. Izmaylov, and Gustavo E. Scuseria. Influence of the exchange screening parameter on the performance of screened hybrid functionals. *The Journal of Chemical Physics*, 125(22):224106, 2006.

[25] O. Gunnarsson, M. Jonson, and B. I. Lundqvist. Descriptions of exchange and correlation effects in inhomogeneous electron systems. *Phys. Rev. B*, 20:3136–3164, Oct 1979.

[26] B.H. Bransden, C.J. Joachain, and T.J. Plivier. *Physics of Atoms and Molecules*. Pearson Education. Prentice Hall, 2003.

[27] E G Maksimov, I I Maxin, S Yu Savrasov, and Yu A Uspenski. Excitation spectra of semiconductors and insulators: a density-functional approach to many-body theory. *Journal of Physics: Condensed Matter*, 1(14):2493–2504, Apr 1989.

[28] A. Svane. Hartree-fock band-structure calculations with the linear muffin-tin-orbital method: Application to C, Si, Ge, and α-Sn. *Phys. Rev. B*, 35:5496–5502, Apr 1987.

[29] P. Horsch. A simple state-dependent exchange functional for calculating Hartree-Fock bandstructures in semiconductors and insulators. *Solid State Communications*, 54(8):741 – 744, 1985.

[30] S. T. Epstein and C. M. Rosenthal. The Hohenberg–Kohn theorem. *The Journal of Chemical Physics*, 67(247), 1976.

[31] John P. Perdew and Mel Levy. Extrema of the density functional for the energy: Excited states from the ground-state theory. *Phys. Rev. B*, 31:6264–6272, May 1985.

[32] John P. Perdew, Robert G. Parr, Mel Levy, and Jose L. Balduz. Density-Functional Theory for Fractional Particle Number: Derivative Discontinuities of the Energy. *Phys. Rev. Lett.*, 49:1691–1694, Dec 1982.

[33] John P. Perdew and Mel Levy. Physical content of the exact Kohn-Sham orbital energies: Band gaps and derivative discontinuities. *Phys. Rev. Lett.*, 51:1884–1887, Nov 1983.

[34] R. W. Godby, M. Schlüter, and L. J. Sham. Self-energy operators and exchange-correlation potentials in semiconductors. *Phys. Rev. B*, 37:10159–10175, Jun 1988.

[35] Aron J. Cohen, Paula Mori-Sánchez, and Weitao Yang. Fractional charge perspective on the band gap in density-functional theory. *Phys. Rev. B*, 77:115123, Mar 2008.

[36] Lars Hedin. Electron correlation: Keeping close to an orbital description. *International Journal of Quantum Chemistry*, 56(5):445–452, 1995.

[37] E. O. Kane. Need for a Nonlocal Correlation Potential in Silicon. *Phys. Rev. B*, 4:1910–1917, Sep 1971.

[38] R. W. Godby and L. J. Sham. Exchange-correlation potentials at semiconductor interfaces. *Phys. Rev. B*, 49:1849–1857, Jan 1994.

[39] Klaus Capelle. A bird's-eye view of density-functional theory. *Braz. J. Phys.*, 36, 12 2002.

[40] Marcus Lundberg and Per E. M. Siegbahn. Quantifying the effects of the self-interaction error in DFT: When do the delocalized states appear? *The Journal of Chemical Physics*, 122(22):224103, 2005.

[41] P. E. Blöchl. Projector augmented-wave method. *Phys. Rev. B*, 50:17953–17979, Dec 1994.

[42] O. Krogh Andersen. Linear methods in band theory. *Phys. Rev. B*, 12:3060–3083, Oct 1975.

[43] D. R. Hamann, M. Schlüter, and C. Chiang. Norm-Conserving Pseudopotentials. *Phys. Rev. Lett.*, 43:1494–1497, Nov 1979.

[44] G. Kresse and D. Joubert. From ultrasoft pseudopotentials to the projector augmented-wave method. *Phys. Rev. B*, 59:1758–1775, Jan 1999.

[45] G Kresse and J Hafner. Norm-conserving and ultrasoft pseudopotentials for first-row and transition elements. *Journal of Physics: Condensed Matter*, 6(40):8245–8257, Oct 1994.

[46] P. Nozieres. *Theory Of Interacting Fermi Systems.* Advanced Books Classics. Avalon Publishing, 1997.

[47] H. Bruus, K. Flensberg, and Oxford University Press. *Many-Body Quantum Theory in Condensed Matter Physics: An Introduction.* Oxford Graduate Texts. OUP Oxford, 2004.

[48] G. Rickayzen. *Green's functions and condensed matter.* Techniques of physics. Academic Press, 1980.

[49] H. Fuxiang. *A Modern Course In The Quantum Theory Of Solids.* World Scientific Publishing Company, 2012.

[50] Christoph Friedrich and Arno Schindlmayr. Many-Body Perturbation Theory: The GW Approximation. 31:335, 01 2006.

[51] Lars Hedin. New Method for Calculating the One-Particle Green's Function with Application to the Electron-Gas Problem. *Phys. Rev.*, 139:A796–A823, Aug 1965.

[52] Richard M. Martin, Lucia Reining, and David M. Ceperley. *Interacting Electrons: Theory and Computational Approaches.* Cambridge University Press, 2016.

[53] A. Marini, R.D. Sole, and A. Rubio. *Approximate Functionals from Many-Body Perturbation Theory*, pages 161–180. Springer Berlin Heidelberg, Berlin, Heidelberg, 2006.

[54] Giovanni Onida, Lucia Reining, and Angel Rubio. Electronic Excitations: Density-Functional versus Many-body Green's-Function Approaches. *Rev. Mod. Phys.*, 74:601–659, Jun 2002.

[55] Lars Hedin and Stig O. Lundqvist. *Effects of Electron-Electron and Electron-Phonon Interactions on the One-Electron States of Solids*, volume 23, pages 1–181. Academic Press, 1969,.

[56] David Pines and David Bohm. A Collective Description of Electron Interactions: II. Collective vs Individual Particle Aspects of the Interactions. *Phys. Rev.*, 85:338–353, Jan 1952.

[57] J. Hubbard and Rudolf Ernst Peierls. The description of collective motions in terms of Many-Body Perturbation Theory. II. The Correlation Energy of a Free-Electron Gas. *Proceedings of the Royal Society of London. Series A. Mathematical and Physical Sciences*, 243(1234):336–352, 1958.

[58] H. Ehrenreich and M. H. Cohen. Self-Consistent Field Approach to the Many-Electron Problem. *Phys. Rev.*, 115:786–790, Aug 1959.

[59] Stephen L. Adler. Quantum Theory of the Dielectric Constant in Real Solids. *Phys. Rev.*, 126:413–420, Apr 1962.

[60] Nathan Wiser. Dielectric Constant with Local Field Effects Included. *Phys. Rev.*, 129:62–69, Jan 1963.

[61] N H March. *Electron Correlation in the Solid State.* PUBLISHED BY IMPERIAL COLLEGE PRESS AND DISTRIBUTED BY WORLD SCIENTIFIC PUBLISHING CO., 1999.

[62] M. van Schilfgaarde, Takao Kotani, and S. Faleev. Quasiparticle self-consistent GW theory. *Phys. Rev. Lett.*, 96:226402, Jun 2006.

[63] Mark S. Hybertsen and Steven G. Louie. First-Principles Theory of Quasiparticles: Calculation of Band Gaps in Semiconductors and Insulators. *Phys. Rev. Lett.*, 55:1418–1421, Sep 1985.

[64] Mark S. Hybertsen and Steven G. Louie. Electron Correlation in Semiconductors and Insulators: Band Gaps and Quasiparticle Energies. *Phys. Rev. B*, 34:5390–5413, Oct 1986.

[65] M. Gajdoš, K. Hummer, G. Kresse, J. Furthmüller, and F. Bechstedt. Linear optical properties in the projector-augmented wave methodology. *Phys. Rev. B*, 73:045112, Jan 2006.

[66] M. Shishkin and G. Kresse. Implementation and performance of the frequency-dependent GW method within the PAW framework. *Phys. Rev. B*, 74:035101, Jul 2006.

[67] M. Shishkin and G. Kresse. Self-consistent GW calculations for semiconductors and insulators. *Phys. Rev. B*, 75:235102, Jun 2007.

[68] Arno Schindlmayr and R. W. Godby. Systematic vertex corrections through iterative solution of hedin's equations beyond the GW approximation. *Phys. Rev. Lett.*, 80:1702–1705, Feb 1998.

[69] MARK E. CASIDA. *Time-Dependent Density Functional Response Theory for Molecules*, pages 155–192.

[70] D.J. Thouless and J.G. Valatin. Time-dependent hartree-fock equations and rotational states of nuclei. *Nuclear Physics*, 31:211 – 230, 1962.

[71] W. Hanke and L. J. Sham. Many-particle effects in the optical spectrum of a semiconductor. *Phys. Rev. B*, 21:4656–4673, May 1980.

[72] G. Strinati. Effects of dynamical screening on resonances at inner-shell thresholds in semiconductors. *Phys. Rev. B*, 29:5718–5726, May 1984.

[73] R. Zimmermann, K. Kilimann, W. D. Kraeft, D. Kremp, and G. Röpke. Dynamical screening and self-energy of excitons in the electron–hole plasma. *physica status solidi (b)*, 90(1):175–187, 1978.

[74] Francesco Sottile. *Response functions of semiconductors and insulators:from the Bethe-Salpeter equation to time-dependent density functional theory.* PhD thesis, Ecole Polytechnique, Palaiseau, 2003.

[75] Stefan Albrecht, Lucia Reining, Rodolfo Del Sole, and Giovanni Onida. Ab Initio Calculation of Excitonic Effects in the Optical Spectra of Semiconductors. *Phys. Rev. Lett.*, 80:4510–4513, May 1998.

[76] Tobias Sander, Emanuele Maggio, and Georg Kresse. Beyond the Tamm-Dancoff approximation for extended systems using exact diagonalization. *Phys. Rev. B*, 92:045209, Jul 2015.

[77] Judith Harl. *The linear response function in density functional theory.* PhD thesis, University of Vienna. Fakultät für Physik, 2008.

[78] Masatoshi Imada, Atsushi Fujimori, and Yoshinori Tokura. Metal-insulator transitions. *Rev. Mod. Phys.*, 70:1039–1263, Oct 1998.

[79] Yoshinori Tokura. Correlated-electron physics in transition-metal oxides. *Phys.Today*, 56:50–55, 2003.

[80] A. Ohtomo and H. Y. Hwang. A high-mobility electron gas at the $LaAlO_3/SrTiO_3$ heterointerface. *Nature*, 427(6973):423–426, 2004.

[81] R. D. Shannon. Revised effective ionic radii and systematic studies of interatomic distances in halides and chalcogenides. *Acta Crystallographica Section A*, 32(5):751–767, 1976.

[82] Jacqueline B. A. A. Elemans, B. Van Laar, K. R. Van Der Veen, and B. O. Loopstra. The crystallographic and magnetic structures of $La_{1-x}Ba_xMn_{1-x}Me_xO_3$ (Me = Mn orTi). *Journal of Solid State Chemistry*, 3(2):238–242, 1971.

[83] P. Norby, I.G. Krogh Andersen, E. Krogh Andersen, and N.H. Andersen. The crystal structure of lanthanum manganate(iii), $LaMnO_3$, at room temperature and at 1273 K under N_2. *Journal of Solid State Chemistry*, 119:191–196, 1995.

[84] J. Rodríguez-Carvajal, M. Hennion, F. Moussa, A. H. Moudden, L. Pinsard, and A. Revcolevschi. Neutron-diffraction study of the Jahn-Teller transition in stoichiometric $LaMnO_3$. *Phys. Rev. B*, 57:R3189–R3192, Feb 1998.

[85] Tapan Chatterji, Fran çois Fauth, Bachir Ouladdiaf, P. Mandal, and B. Ghosh. Volume collapse in $LaMnO_3$ caused by an orbital order-disorder transition. *Phys. Rev. B*, 68:052406, Aug 2003.

[86] H. E. Swanson G. M. Ugrinic R. K. Fuyat and U. States. Standard X-ray diffraction powder patterns. *National Bureau of Standars circular 539*, 3:73, 1954.

[87] A. J. Smith and A. J. E. Welch. Some mixed metal oxides of perovskite structure. *Acta Crystallographica*, 13(8):653–656, Aug 1960.

[88] Brendan J. Kennedy, Christopher J. Howard, and Bryan C. Chakoumakos. High-temperature phase transitions in $SrHfO_3$. *Phys. Rev. B*, 60:2972–2975, Aug 1999.

[89] J. Sigman, D. P. Norton, H. M. Christen, P. H. Fleming, and L. A. Boatner. Antiferroelectric behavior in symmetric $KNbO_3/KTaO_3$ superlattices. *Phys. Rev. Lett.*, 88:097601, Feb 2002.

[90] S. Geller. Crystallographic studies of perovskite-like compounds. IV. Rare earth scandates, vanadites, galliates, orthochromites. *Acta Crystallographica*, 10(4):243–248, Apr 1957.

[91] C.P. Khattak and D.E. Cox. Structural studies of the (La, Sr) CrO_3 system. *Materials Research Bulletin*, 12(5):463 – 471, 1977.

[92] M. Cwik, T. Lorenz, J. Baier, R. Müller, G. André, F. Bourée, F. Lichtenberg, A. Freimuth, R. Schmitz, E. Müller-Hartmann, and M. Braden. Crystal and magnetic structure of $LaTiO_3$: Evidence for nondegenerate t_{2g} orbitals. *Phys. Rev. B*, 68:060401, Aug 2003.

[93] M. Marezio Q. Huang A. Santoro S.-W.Cheong H. Takagi C. Oglesby P. Bordet, C. Chaillout. Structural aspects of the crystallographic-magnetic transition in $LaVO_3$ around 140 k. *Journal of Solid State Chemistry*, 106(2):253 – 270, 1993.

[94] S.E. Dann, D.B. Currie, M.T. Weller, M.F. Thomas, and A.D. Al-Rawwas. The effect of oxygen stoichiometry on phase relations and structure in the system $La_{1-x}Sr_xFeO_{3-\delta}$ ($0 <= x <= 1$, $0 <= -\delta <= 0.5$). *Journal of Solid State Chemistry*, 109(1):134 – 144, 1994.

[95] Rune Søndenå, P. Ravindran, Svein Stølen, Tor Grande, and Michael Hanfland. Electronic structure and magnetic properties of cubic and hexagonal $SrMnO_3$. *Phys. Rev. B*, 74:144102, Oct 2006.

[96] Efrain E. Rodriguez, Frédéric Poineau, Anna Llobet, Brendan J. Kennedy, Maxim Avdeev, Gordon J. Thorogood, Melody L. Carter, Ram Seshadri, David J. Singh, and Anthony K. Cheetham. High temperature magnetic ordering in the 4*d* perovskite $SrTcO_3$. *Phys. Rev. Lett.*, 106:067201, Feb 2011.

[97] Y. G. Shi, Y. F. Guo, S. Yu, M. Arai, A. A. Belik, A. Sato, K. Yamaura, E. Takayama-Muromachi, H. F. Tian, H. X. Yang, J. Q. Li, T. Varga, J. F. Mitchell, and S. Okamoto. Continuous metal-insulator transition of the antiferromagnetic perovskite $naoso_3$. *Phys. Rev. B*, 80:161104, Oct 2009.

[98] M. Braden, G. André, S. Nakatsuji, and Y. Maeno. Crystal and magnetic structure of Ca_2RuO_4: Magnetoelastic coupling and the metal-insulator transition. *Phys. Rev. B*, 58:847–861, Jul 1998.

[99] Zeynep Ergönenc, Bongjae Kim, Peitao Liu, Georg Kresse, and Cesare Franchini. Converged GW Quasiparticle Energies for Transition Metal Oxide Perovskites. *Phys. Rev. Materials*, 2:024601, Feb 2018.

[100] Zeynep Ergönenc. *Converged GW quasiparticle energies for transition metal oxide perovskites.* PhD thesis, University of Vienna. Fakultät für Physik, 2017.

[101] N F Mott. The basis of the electron theory of metals, with special reference to the transition metals. *Proceedings of the Physical Society. Section A*, 62(7):416–422, Jul 1949.

[102] Igor Solovyev, Noriaki Hamada, and Kiyoyuki Terakura. t_{2g} versus all 3d localization in $LaMO_3$ perovskites (M=Ti–Cu): First-principles study. *Phys. Rev. B*, 53:7158–7170, Mar 1996.

[103] Ersoy Şaşıoğlu, Christoph Friedrich, and Stefan Blügel. Effective coulomb interaction in transition metals from constrained random-phase approximation. *Phys. Rev. B*, 83:121101, Mar 2011.

[104] Loïg Vaugier, Hong Jiang, and Silke Biermann. Hubbard U and hund exchange J in transition metal oxides: Screening versus localization trends from constrained random phase approximation. *Phys. Rev. B*, 86:165105, Oct 2012.

[105] J. Zaanen, G. A. Sawatzky, and J. W. Allen. Band gaps and electronic structure of transition-metal compounds. *Phys. Rev. Lett.*, 55:418–421, Jul 1985.

[106] D. Feng and G. Jin. *Introduction to Condensed Matter Physics*. Number v. 1. World Scientific, 2005.

[107] Jernej Mravlje, Markus Aichhorn, and Antoine Georges. Origin of the high neel temperature in $SrTcO_3$. *Physical Review Letters*, 108:197202–197202, 2012.

[108] C. Franchini, T. Archer, Jiangang He, Xing-Qiu Chen, A. Filippetti, and S. Sanvito. Exceptionally strong magnetism in the 4d perovskites $RTcO_3$ (R=Ca,Sr, Ba). *Phys. Rev. B*, 83:220402, Jun 2011.

[109] I. Lo Vecchio, A. Perucchi, P. Di Pietro, O. Limaj, U. Schade, Y. Sun, M. Arai, K. Yamaura, and S. Lupi. Infrared evidence of a Slater metal-insulator transition in $NaOsO_3$. *Scientific Reports*, 3:2990 EP –, Oct 2013. Article.

[110] Bongjae Kim, Peitao Liu, Zeynep Ergönenc, Alessandro Toschi, Sergii Khmelevskyi, and Cesare Franchini. Lifshitz transition driven by spin fluctuations and spin-orbit renormalization in $NaOsO_3$. *Phys. Rev. B*, 94:241113, Dec 2016.

[111] J. G. Vale, S. Calder, C. Donnerer, D. Pincini, Y. G. Shi, Y. Tsujimoto, K. Yamaura, M. Moretti Sala, J. van den Brink, A. D. Christianson, and D. F. McMorrow. Evolution of the magnetic excitations in $NaOsO_3$ through its metal-insulator transition. *Phys. Rev. Lett.*, 120:227203, May 2018.

[112] Vladislav Borisov, Sergey Ostanin, and Ingrid Mertig. Two-dimensional electron gas and its electric control at the interface between ferroelectric and antiferromagnetic insulator studied from first principles. *Phys. Chem. Chem. Phys.*, 17:12812, Dec 2015.

[113] F. Gebhard. *The Mott Metal-Insulator Transition: Models and Methods*. Springer Tracts in Modern Physics. Springer Berlin Heidelberg, 2003.

[114] Luca de' Medici, Jernej Mravlje, and Antoine Georges. Janus-faced influence of Hund's rule coupling in strongly correlated materials. *Phys. Rev. Lett.*, 107:256401, Dec 2011.

[115] G. Kresse and J. Furthmüller. Efficient iterative schemes for ab initio total-energy calculations using a plane-wave basis set. *Phys. Rev. B*, 54:11169–11186, Oct 1996.

[116] S. L. Dudarev, G. A. Botton, S. Y. Savrasov, C. J. Humphreys, and A. P. Sutton. Electron-Energy-Loss Spectra and the Structural Stability of Nickel Oxide: An LSDA+U study. *Phys. Rev. B*, 57:1505–1509, Jan 1998.

[117] M. Sousa, C. Rossel, C. Marchiori, H. Siegwart, D. Caimi, J.-P. Locquet, D. J. Webb, R. Germann, J. Fompeyrine, K. Babich, J. W. Seo, and Ch. Dieker. Optical properties of epitaxial $SrHfO_3$ thin films grown on Si. *Journal of Applied Physics*, 102(10):104103, 2007.

[118] Y. S. Lee, J. S. Lee, T. W. Noh, Douck Young Byun, Kwang Soo Yoo, K. Yamaura, and E. Takayama-Muromachi. Systematic trends in the electronic structure parameters of the $4d$ transition-metal oxides $\mathrm{Sr}m\mathrm{o}_3(m =$ Zr, mo, ru, and rh). *Phys. Rev. B*, 67:113101, Mar 2003.

[119] Yunsang Lee and Y. K. Seo D. J. Lee. Optical spectroscopic study on the electronic structure of $SrHfO_3$. *J. Korean Phys. Soc.*, 56:366, 2010.

[120] T. Arima, Y. Tokura, and J. B. Torrance. Variation of optical gaps in perovskite-type 3d transition-metal oxides. *Phys. Rev. B*, 48:17006–17009, Dec 1993.

[121] J. H. Jung, K. H. Kim, D. J. Eom, T. W. Noh, E. J. Choi, Jaejun Yu, Y. S. Kwon, and Y. Chung. Determination of electronic band structures of $CaMnO_3$ and $LaMnO_3$ using optical-conductivity analyses. *Phys. Rev. B*, 55:15489–15493, Jun 1997.

[122] J. H. Jung, Z. Fang, J. P. He, Y. Kaneko, Y. Okimoto, and Y. Tokura. Change of electronic structure in $CaRuO_4$ induced by orbital ordering. *Phys. Rev. Lett.*, 91:056403, Jul 2003.

[123] Peitao Liu, Merzuk Kaltak, Ji ří Klimeš, and Georg Kresse. Cubic scaling GW: Towards fast quasiparticle calculations. *Phys. Rev. B*, 94:165109, Oct 2016.

[124] F. Fuchs, C. Rödl, A. Schleife, and F. Bechstedt. Efficient $\mathcal{O}(N^2)$ approach to solve the Bethe-Salpeter equation for excitonic bound states. *Phys. Rev. B*, 78:085103, Aug 2008.

[125] Menno Bokdam, Tobias Sander, Alessandro Stroppa, Silvia Picozzi, D. D. Sarma, Cesare Franchini, and Georg Kresse. Role of Polar Phonons in the Photo Excited State of Metal Halide Perovskites. *Scientific Reports*, 6:28618, Jun 2016.

[126] Peitao Liu, Bongjae Kim, Xing-Qiu Chen, D. D. Sarma, Georg Kresse, and Cesare Franchini. Relativistic GW+BSE study of the optical properties of Ruddlesden-Popper iridates. *Phys. Rev. Materials*, 2:075003, Jul 2018.

[127] Vincenzo Fiorentini and Alfonso Baldereschi. Dielectric scaling of the self-energy scissor operator in semiconductors and insulators. *Phys. Rev. B*, 51:17196–17198, Jun 1995.

[128] Lorenzo Sponza, Valérie Véniard, Francesco Sottile, Christine Giorgetti, and Lucia Reining. Role of localized electrons in electron-hole interaction: The case of $SrTiO_3$. *Phys. Rev. B*, 87:235102, Jun 2013.

[129] W. G. Schmidt, S. Glutsch, P. H. Hahn, and F. Bechstedt. Efficient $\mathcal{O}(N^2)$ method to solve the Bethe-Salpeter equation. *Phys. Rev. B*, 67:085307, Feb 2003.

[130] Dario Rocca, Deyu Lu, and Giulia Galli. Ab initio calculations of optical absorption spectra: Solution of the bethe–salpeter equation within density matrix perturbation theory. *The Journal of Chemical Physics*, 133(16):164109, 2010.

[131] Michael Rohlfing and Steven G. Louie. Electron-Hole Excitations in Semiconductors and Insulators. *Phys. Rev. Lett.*, 81:2312–2315, Sep 1998.

[132] Joachim Paier, Martijn Marsman, and Georg Kresse. Dielectric properties and excitons for extended systems from hybrid functionals. *Phys. Rev. B*, 78:121201, Sep 2008.

[133] Vijaya Begum, Markus Ernst Gruner, and Rossitza Pentcheva. Role of the exchange-correlation functional on the structural, electronic, and optical properties of cubic and tetragonal $\mathrm{SrTiO_3}$ including many-body effects. *Phys. Rev. Materials*, 3:065004, Jun 2019.

[134] F. Aryasetiawan and O. Gunnarsson. Electronic structure of NiO in the GW approximation. *Phys. Rev. Lett.*, 74:3221–3224, Apr 1995.

[135] Hong Jiang, Ricardo I. Gomez-Abal, Patrick Rinke, and Matthias Scheffler. Localized and itinerant states in lanthanide oxides united by GW@LDA+U. *Phys. Rev. Lett.*, 102:126403, Mar 2009.

[136] Jiangang He and Cesare Franchini. Structural determination and electronic properties of the 4d perovskite $\mathrm{SrPdO_3}$. *Phys. Rev. B*, 89:045104, Jan 2014.

[137] Joachim Paier, Martijn Marsman, and Georg Kresse. Dielectric properties and excitons for extended systems from hybrid functionals. *Phys. Rev. B*, 78:121201, Sep 2008.

[138] Cesare Franchini. *Electronic Structure of Perovskites: Lessons from Hybrid Functionals,* in *Many-Body Physics: From Kondo to Hubbard.* Modeling and Simulation. Verlag des Forschungszentrum Jülich, 2015.